

Section 3.2.1 Appendix A: Yukon Field Methods

Fabrice Calmels, Fanny Amyot and Louis-Philippe Roy

January 2022

1. Introduction

Field investigations were focused largely on the acquisition of new geophysical information including electrical resistivity tomography (ERT) surveys and ground penetrating radar (GPR) surveys, and shallow drilling to develop cryostratigraphic logs and to validate interpretations of geophysical information. In addition, unmanned aerial vehicle (UAV) surveys were performed to create high resolution imagery and digital surface models (DSMs).

2. Geophysics

2.1. Electrical Resistivity Tomography

Electrical resistivity tomography (ERT) is a geophysical method that passes electrical current through stainless steel electrodes that are driven into the ground surface. A resistivity meter located at a central “station” measures the resistivity distribution of the subsurface between electrode pairs. Resistivity is the mathematical inverse of conductivity and indicates the ability of an electrical current to pass through a material. Mineral materials (except for specific substances such as metallic ores) are mostly non-conductive. Therefore, variation in the resistivity of a soil or rock profile is governed primarily by the amount and resistivity of pore water present in the profile, and the arrangement of the pores. This makes ERT very well suited to permafrost and hydrology applications. Because most water content in frozen ground is in the solid phase and typically has a higher resistivity than unfrozen water content, permafrost distribution can be inferred based on changes in resistivity between frozen and unfrozen ground.

An ERT system consists of an automated imaging unit and a set of wires connected to an electrode array. The system used for the surveys presented in this report is an ABEM Terrameter LS electrical resistivity and tomography system, consisting of a four-channel imaging unit and four electrode cables, each with 21 take-outs at five-meter intervals. To conduct a survey, 81 electrodes are driven into the ground along a survey line and connected to the electrode cables (Figure 1).

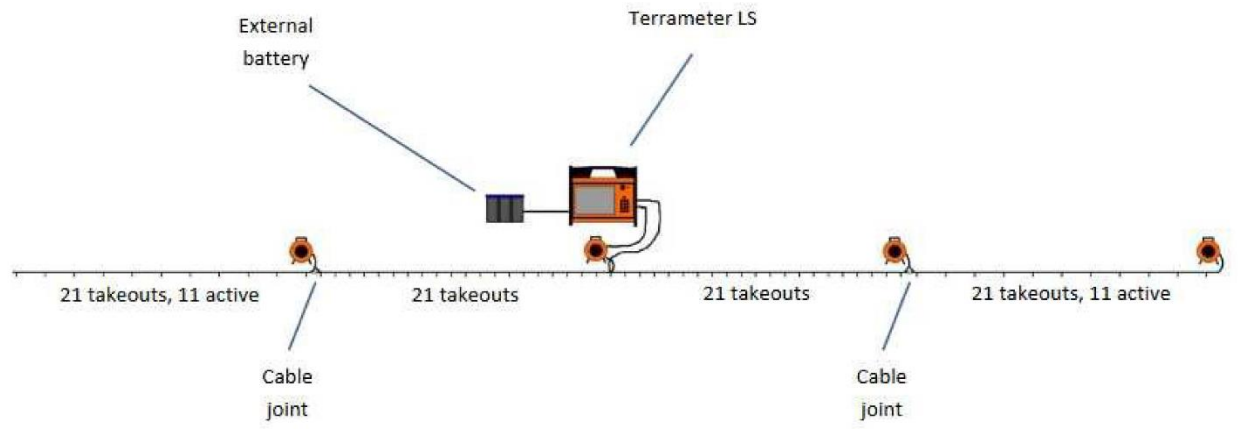


Figure 1 Instrument set-up for ERT surveying

Multiple array types have been used at different sites, including the “Wenner”, “Dipole-dipole”. These arrays differ in how they pair current and potential electrodes (Figure 2). A direct current electrical pulse is sent from the resistivity meter along the survey line in two current electrodes (C1 and C2), and the measurement is performed by two potential electrodes (P1 and P2). The resulting data consists of a cross-sectional (2D) plot of the ground’s resistivity ($\text{ohm}\cdot\text{m}$) versus depth (m) for the length of the survey.

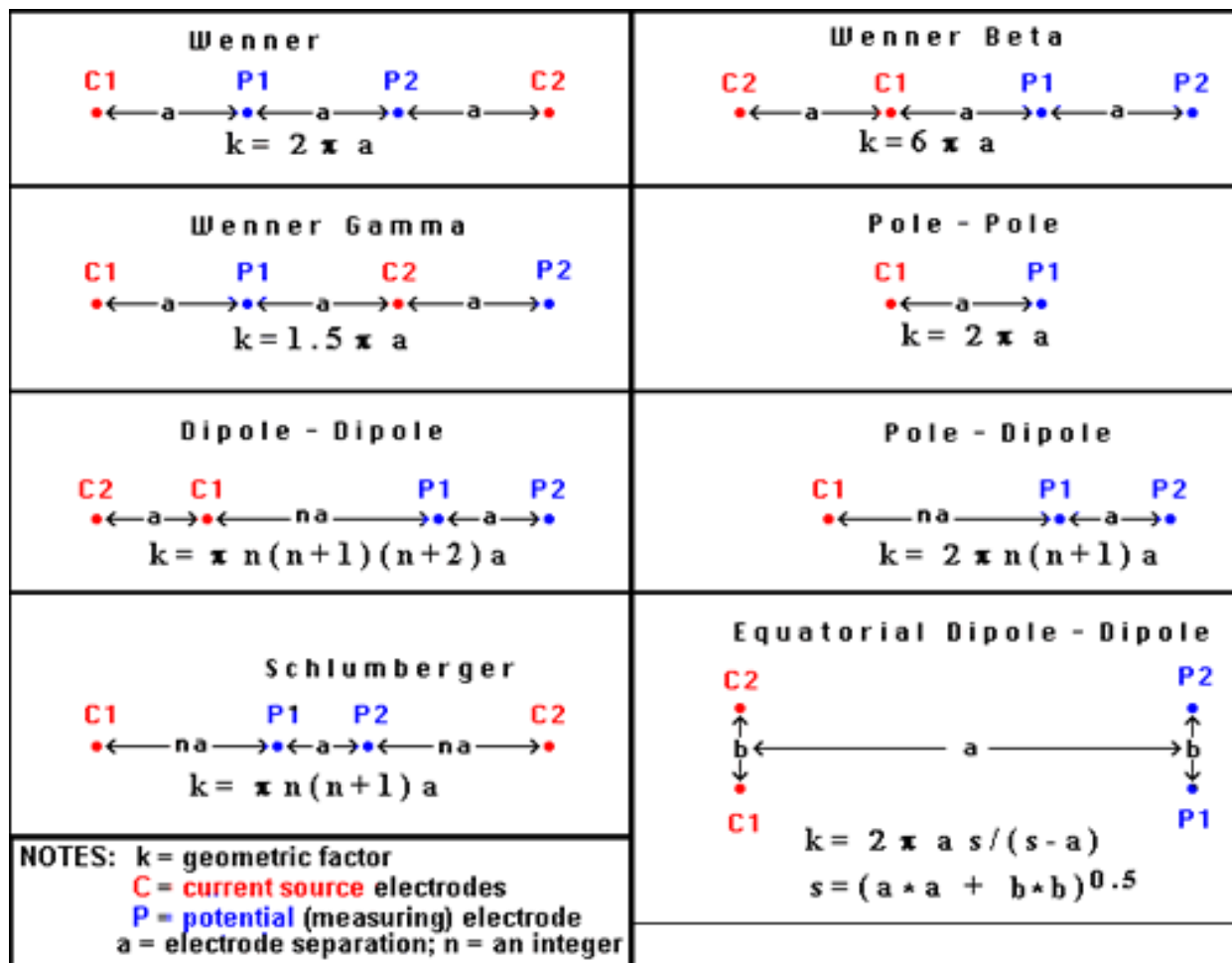


Figure 2. Survey configurations or “arrays” for ERT surveying

In general, the Wenner array is good at resolving vertical changes (i.e., horizontal structures), but relatively poor at detecting horizontal changes (i.e., narrow vertical structures). Compared to other arrays, the Wenner array has a moderate depth of investigation. Among the common arrays, the Wenner array has the strongest signal strength. This can be an important factor if the survey is carried out in areas with high background noise, since relatively small current magnitudes are needed to produce measurable potential differences. A disadvantage with the Wenner method is that to image deep into the earth, long current cables are required due to the configuration. The Wenner array is also very sensitive to near surface inhomogeneities which may skew deeper electrical responses. Another disadvantage of this array for 2-D surveys is the relatively poor horizontal coverage as the electrode spacing is increased, which can be problematic when using a system with a relatively small number of electrodes.

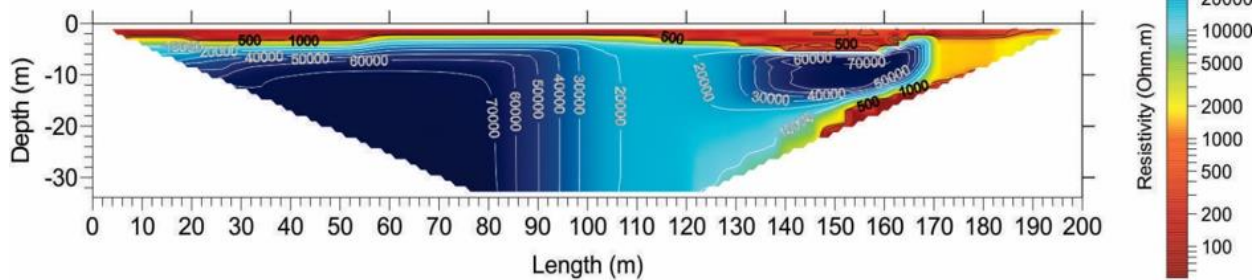
The dipole-dipole array is very sensitive to horizontal changes in resistivity, but relatively insensitive to vertical changes in the resistivity. That means that it is good for mapping vertical structures, such as dykes and cavities, but relatively poor in mapping horizontal

structures such as sills or sedimentary layers. This array has a deeper depth of investigation compared to the Wenner array, and has better horizontal data coverage than the Wenner, which can be an advantage when the number of nodes available with the multi-electrode system is small. One possible disadvantage can be a very small signal strength. However, with the proper field equipment and survey techniques, this array has been successfully used in many areas to detect structures such as cavities where the good horizontal resolution of this array is a major advantage.

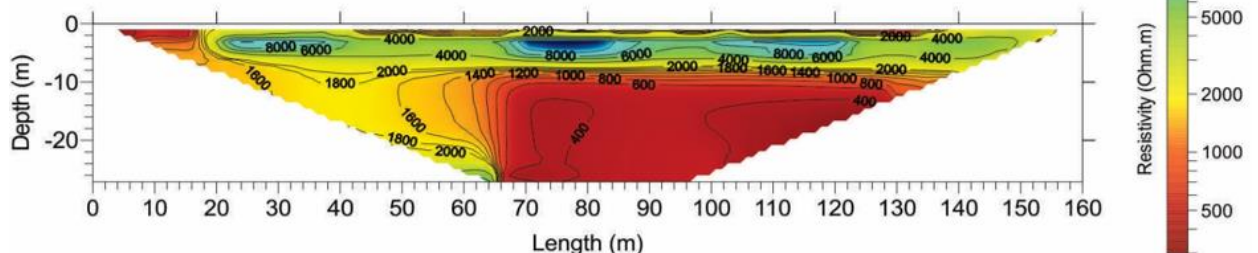
Over time, the Dipole-Dipole array has proven to be more reliable and representative of ground conditions than other array types. From field and borehole observations it appears to be more representative of permafrost characteristics than the Wenner configuration. Notably, ice rich areas appear to be more discrete and realistic in shape in the Dipole-dipole than in the Wenner, as depicted in Figure 3. This figure shows an illustrative example of ERT surveys, where there are clear differences between the Wenner and Dipole-dipole profiles, where the Dipole-dipole survey better represents reality. This is just one example, among many others. As such, the Dipole-dipole survey is the only survey-type presented in this document

Results from the field surveys are processed and analyzed using inversion software (Res2DInv 64 and Res3DInv 32) and gridded in Surfer.

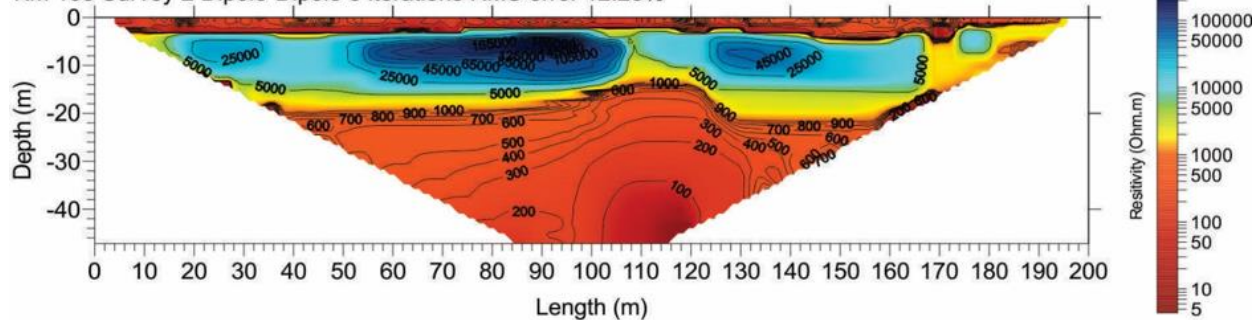
Km 103 Survey 2 Wenner 10 iterations RMS error 6.60%



Km 103 Survey 1 Wenner 3 iterations RMS error 6.31%



Km 103 Survey 2 Dipole-Dipole 8 iterations RMS error 12.23%



Km 103 Survey 1 Dipole-dipole 7 iterations RMS error 6.48%

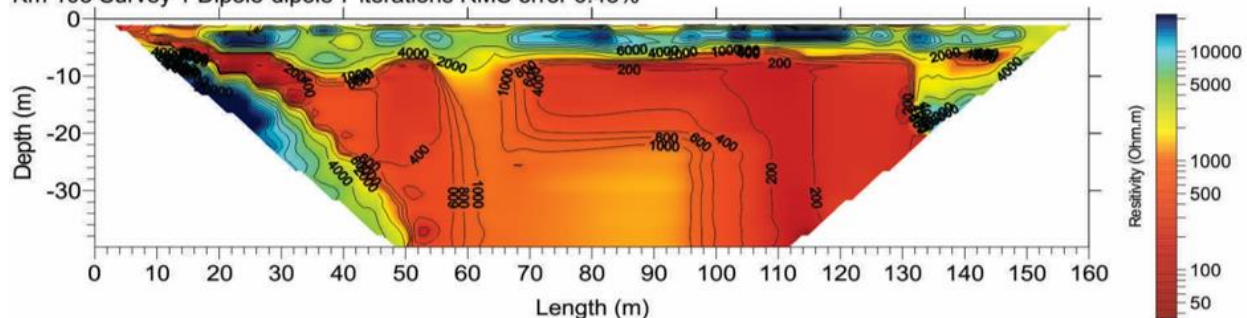


Figure 3. ERT profiles from km 103 of the Dempster Highway showing the difference between the Wenner and the Dipole-dipole surveys

2.2. Ground Penetrating Radar

Ground penetrating radar (GPR) is a geophysical tool that sends an electromagnetic signal from a transmitter that is captured by the receiver after penetrating and being reflected by the ground. GPR profiles are 2-dimensional profiles that show the interface

between materials with different dielectric properties. The frequency of the signal emitted by the GPR system determines the depth of the radar penetration. For these surveys, a Pulse Ekko system with a 50 MHz or 100 MHz antenna was used, at a separation of 2 and 1 m respectively. Whenever possible, the GPR data were integrated with GPS positions.

GPR data were processed and viewed in the GPRPy python module (Alain Plattner, 2020). This open-source software module allows for processing through the command line, or in a graphical user interface. Each GPR line underwent basic processing including a dewow process to remove very low frequency components from the data (Annan, 2005). Then, the velocity was set to calibrate the depth of the signals, since no in situ depth analyses were done. The velocity values were based on tabular data between 0.1 and 0.13 m/ns depending on the substrate. 0.1 m/ns was the most used velocity, as a compromise between silt, sand, sand and gravel and permafrost. Given the general heterogeneity in the substrate within and between sites, the depths presented in the GPR profiles should be considered approximations. Moreover, error in GPS measurements can lead to uncertainty in the position of features along the GPR profile, which should also be considered approximations.

GPR interpretations were performed using existing ERT profiles, satellite and UAV imagery and field observations.

3. Permafrost drilling and sample collection

The same sampling and drilling protocols were followed for each borehole drilled by the Yukon U research team. The site was first described (e.g., hydrology, vegetation type and density, topography), photos were taken, and locations were recorded using a hand-held GPS.

A light and portable GÖLZ Earth-drill system was used to drill shallow boreholes. Boreholes were initiated by shoveling down to the thaw front. At the thaw front, the Earth-drill system was used. The drill uses a small Stihl engine with 600 rpm high-speed transmission. The drill is coupled with stainless steel rods (1 meter in length and 4.5 cm in diameter) and a core barrel (40 cm long and 10 cm in diameter) with diamonds set in carbide alloy teeth. The drill is used in unconsolidated, fine to medium-grain material (sand to clay). A core catcher tool was used to extract frozen cores from the borehole, allowing for the collection of continuous, undisturbed permafrost samples. This type of drilling is limited to a maximum drilling depth of approximately 5 to 6 m under optimal

conditions. To drill boreholes at deeper depths, a conventional water-jet diamond drill was used. Details regarding these tools and the drilling methodology are provided in Calmels, Gagnon and Allard (2005).

Each core sample was photographed and described in situ (e.g., soil type, soil moisture, presence or absence of organic matter, any notable features). Each extracted sample was identified by borehole name and depth. Samples were put in polybags and sealed immediately after being extracted. Samples were kept frozen and stored in a freezer that was taken back to the laboratory for further analyses. In the laboratory, each core was cleaned with cold water to remove drilling mud and then photographed.

Additional drilling was performed by Midnight Sun who were contracted by YHPW to drill deep boreholes with both a sonic drill and a CRREL drill. The cores were handled and processed in the same manner as mentioned above.

4. Permafrost sample analysis

Laboratory analyses were carried out to measure the properties of the permafrost samples. Both soil grain characteristics and ice characteristics were evaluated. To evaluate soil grain characteristics, a grain-size analysis was performed on selected samples. To evaluate ice characteristics in permafrost samples, the cryostructure, volumetric excess ice content and gravimetric ice content were quantified. These methods are described below. For more information, please refer to Andersland and Ladanyi (2004).

4.1. Grain-size analysis

At Yukonu, grain size analyses were performed using sieves and hydrometers following a specifically modified American Standard and Testing Method protocol (ASTM D422-63, 2000). The sieves used were 4, 2, 1, 0.5, 0.25, 0.125 and 0.063 mm.

At UdeM, The sediments' grain-size distribution >0.25 mm was measured by sieving at 16, 8, 4, 2, 1, 0.5 and 0.25 mm. In addition to sieving, the sediments' grain-size distribution <0.25 mm of a selection of soil and permafrost samples was measured using a LASER analyzer, the model used was the Mastersizer 3000 from Malvern Panalytical.

4.2. Organic matter content

The organic matter content was calculated using the Loss-on-Ignition method with 2 g of dry sediments under combustion at 575 °C during 15 min:

$$OM = \frac{S_d - S_b}{S_d}$$

where **OM** is the organic matter content (gravimetric), measured as weight loss after a subsample of dry sediment (S_d) has burned (S_b). Results are expressed as percentages (dimensionless). The sediments were sieved to <2 mm while subsampling. The furnace used was a Lindberg/Blue M™ Moldatherm™ Box Furnaces.

4.3. Ion chromatography test (hydro geochemistry)

The dilution water of soil and permafrost sample had its content of major cation (lithium, sodium, potassium, magnesium, calcium and ammonia) measured using a chromatograph model 930 Compact IC Flex from Metrohm. For the measurement, 1 g of soil was mixed in 25 mL of deionized water and stirred for 90 min in 50 mL centrifuge tubes, and then settled during 15 min at 4000 rpm. The dilution water was then filtered to <0.45 µm before going in the instrument.

4.4. Cryostructure

Permafrost cryostructure (the geometry of the ice in the permafrost) depends on water availability, the soil's ice-segregation potential, and the time of freezing, all of which affect the development of ice structures in the soil matrix. Information such as soil genesis, climate conditions at the time of freezing, permafrost development history, and ground vulnerability when permafrost degrades can be interpreted from cryostructure (the shape of the ground ice), cryofacies (groups of cryostructures) analysis, and general cryostratigraphy (assemblages of cryofacies).

Because field descriptions are based only on a visual interpretation of the core, the samples were described a second time more thoroughly in the laboratory using standard terminology (Murton and French 1994). Frozen core samples were warmed to near 0°C and any refrozen mud was scraped off before the sample was described.

4.5. Gravimetric ice content

Ice content was calculated using:

$$Ice = \frac{M_i}{M_s}$$

where M_i is the ice weight, measured as weight loss after drying (g), and M_s is the dry soil weight in grams. Results are expressed as percentages (dimensionless).

4.6. Volumetric excess ice content

The volumetric excess ice content was calculated by immersing the frozen sample, bagged in vacuum- sealed polybags, in a recipient to measure its volume (V_{tot}). The sample was then thawed and put in the oven to dry. The remaining dry material was immersed again to determinate its volume (V_{sed}). The volume of excess content was calculated using:

$$V_{ice} = V_{tot} - V_{sed}$$

The volumetric excess ice content is expressed as percentages (fundamentally meaning cm^3/cm^3).

4.7. Borehole logs

A log for each permafrost borehole was created by assembling laboratory photos of the cores. Borehole logs include maximal depths, grain size ratio and volumetric excess ice content. These logs were used as supporting data for mapping.

5. Measurements of ice properties

5.1. Crystallography

The crystallographic analysis of the pure ice is based on pictures taken using a reflex-type Nikon camera on a tripod in a freezing room. The ice samples were sliced along relevant axis at selected points in order to initiate the thin section of ice core. The slice was photographed a first time with its initial thickness under clear light (to show bubbles) then stuck on a frozen glass plate complemented with gauges at corners for uniformizing the next step: thermo eroding the thin section to a given thickness by rubbing it against a flat stainless-steel plate and absorbing away the resulting excess meltwater.

Once ready, the thin section was photographed again, and then put in between two light-polarizing filters (showing different angle difference) over a light-table. The different

crystals were then exposed by different colors and the display was then photographed using a constant camera setting for allowing comparison among the dataset.

For each massive ice sample two thin section were analysed, one for the plane horizontal to the ground surface (H) and one that is vertical (V).

6. Measurements of water properties

6.1. Stable isotopes

The ratio of stable isotopes of oxygen and hydrogen in the water and melted ice was measured on contract by the GEOTOP laboratory in Université du Québec à Montréal (UQAM: <https://www.geotop.ca/index.php/fr/laboratoires/isotopes-stables-UQAM>). Sealed subsamples of 1.5 mL filtered to $<0.2 \mu\text{m}$ were sent.

6.2. Ion chromatography test (hydro geochemistry)

The water directly taken in the soil and from melted ice samples had its content of major cation (lithium, sodium, potassium, magnesium, calcium and ammonia) measured using a chromatograph model 930 Compact IC Flex from Metrohm. The water was filtered to $<0.45 \mu\text{m}$ before going in the instrument.

6.3. pH and electrical conductivity

The electrical conductivity (EC) and pH of the soil free water of dilution water were measured in a 30 cc content using a PCSTestr35 from Oakton (<http://envcoglobal.com/catalog/water/water-quality-pocket-meters/eutech-pocket-meter/pcstestr-35>) calibrated using pH and EC standards provided by the same manufacturer. When measuring free water, about 20 mL was directly subsampled and put in the recipient to be readily measured by the instrument. When measuring dilution water, about 5 g of the wet soil was subsampled and mixed with 20 mL of deionized water.

Such a low soil to water ratio was necessary to suit all the sediments widely ranging between fully organic and fibrous to fully mineral. The water was stirred first, then let sit for 1 h, and then stirred again, and measured after a few minutes of decantation.

7. Ground temperature and climate monitoring

For ground temperature monitoring, newly-drilled boreholes are instrumented with an Onset HOBO (UX-120) four-channel external data logger. This stand-alone weatherproof logger can record data at various intervals and uses a direct USB interface for fast data offload. The logger requires two 1.5 V AAA battery. The batteries typically last one year when logging intervals are greater than one minute. To ensure uninterrupted operation, the data loggers are placed in a sealed 15-cm x 15-cm junction box that is connected to the borehole casing. All borehole casings are made of electrical-grade PVC filled with silicone oil. The temperature sensors (TMC-HD) can accurately record temperatures ranging from -40°C to $+70^{\circ}\text{C}$. They have an accuracy of 0.15°C from 0°C to 70°C , and a resolution of 0.002°C at 25°C .

Two of the boreholes (Bh-BI-2 and Bh-Wr) were first instrumented with the abovementioned loggers, but were replaced with LogR UlogC16-32 loggers that have an integrated 3.6 V type C lithium battery that is meant to last 12 years. The temperature sensors can accurately record temperatures ranging from -55°C to $+80^{\circ}\text{C}$, with an accuracy of $\pm 0.05^{\circ}\text{C}$ between 0 - 50°C .

8. UAV Surveys

The surveys have been completed using two models of UAVs, the DJI Phantom 4 Pro V2 and the DJI Matrix RTK 210 V2. The Phantom 4 Pro V2 is equipped with a camera which produces 20MP images. When using this model, targets were placed on the ground with their position geolocated using a DGPS (differential global positioning system). The target's locations were used as ground control points (GCP) to produce centimeter-scale positional accuracy for the processed imagery. The coordinates of the GCPs were measured using a Trimble R8 GNSS receiver using a real time kinematic (RTK) configuration including a base station and rover.

The Matrice 210 RTK is equipped with a Zenmuse X7 (35mm) which produces 24MP images. During the first year of operations, surveys were completed without GCP, however for the second year GCPs were used to increase the positional accuracy for the processed imagery.

Images were processed using Agisoft Metashape Professional photogrammetry software. For each survey, a point cloud, a 3D model including mesh and texture, a digital

surface model (DSM), and an orthomosaic were produced. All final products were projected to UTM Zone 8.

9. References

- Andersland, O.B., Ladanyi, B. 2004. Frozen Ground Engineering. 2nd Edition. John Wiley & Sons, 384 p.
- Annan, A. P. (2005). GPR methods for hydrogeological studies. In *Hydrogeophysics* (pp. 185-213). Springer, Dordrecht.
- Calmels, F., Gagnon, O.; and Allard, M. 2005. A portable earth-drill system for permafrost studies. *Permafrost and Periglacial Processes* 16: 311-315.
- Plattner, Alain M. "GPRPy: Open-source ground-penetrating radar processing and visualization software." *The Leading Edge* 39.5 (2020): 332-337.

Section 3.2.1 Appendix B:

Topography, surface water and samples

Michel Sliger and Daniel Fortier

January 2022

Edited by: Frances Amyot

1. Introduction

The topography of the land was analysed in order to interpret the surface, subsurface and groundwater flow paths. In order to favor understanding the right level of detail at the scale of the site, it has been divided in eight zones, shown in Figure 1. Their relative importance to the initial objectives is unequal but we believe all of them can feed the interpretation of the subsurface hydrogeology in the thin critical area between the lake and the river. More precisely, the four first zones (A, B, C and D) should support the interpretations of the four lasts (E, F, G and H). They consist in:

- A- the highest level of the terrain where the water is less affected by mixing,
- B- the road itself, where B represents exactly the water-divide,
- C- the older gravel-borrow, where important ground settlement occurred after surface excavations,
- D- the Eastern Lake, an alternative watershed for comparing the data found elsewhere on the site,
- E- the lakeside isthmus, where the water of the roadside flows down toward the lake,
- F- the riverside isthmus, where the water of the roadside (and maybe from the lake) flows down toward the river while enhancing bank erosion,
- G- the polygon field, a water basin where the water of a higher pond, the road and the surrounding slopes migrates in an ice-wedge polygonal network toward the lake, and,
- H- the upstream bank, where the water of the roadside (and maybe from the upper pond) flows down toward the river while enhancing bank erosion.

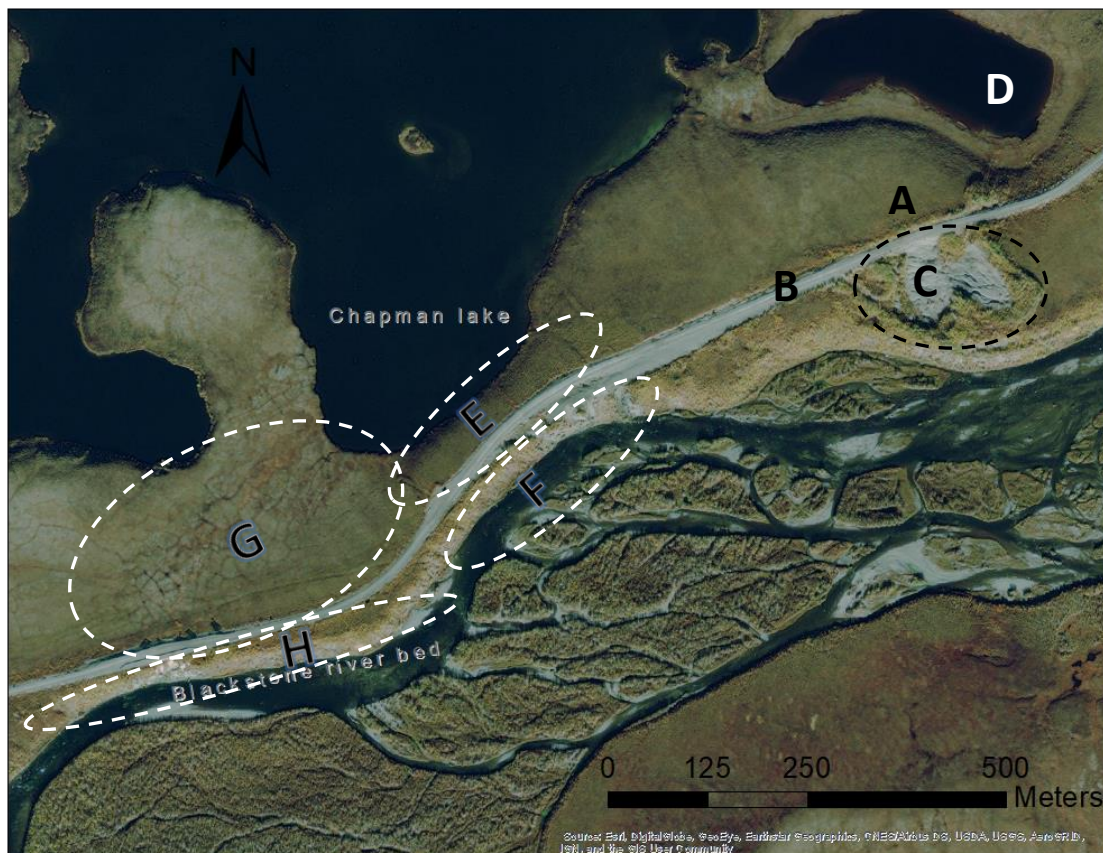


Figure 1 Location of the eight zones of the topographical analysis.

1.1. Sections A and B – Highest points, road and water-divides

Figure 2 shows sections A and B. The road seems to be cut in the original 10-m hill (relative elevation). The highest point on-site is represented by A, at this point the meteoritic water (snow and rain) can remain trapped in the tussock microtopography but during the summer, along with the development of the active layer, it might run down by the

subsurface in a diverging manner in every surrounding slopes. Most of it point toward the lake but the southern slope goes toward the road where a ditch collects the surface water and distribute it equally on both sides.

The only culvert for the surface water to cross the road in this zone is just above B; the road's highest point. Most of the portion of the terrain north of the road drains down to the lake by an ice-wedge polygonal network poorly expressed on the convex portion of the slope. The portion south of the crest drains down to the road ditch where surface water diverges to run toward both sides. A lower point exists in the lakeside ditch between A and B. At this place the surface water converge but there is no accommodation for it to cross the road.

The situation of subsurface water is unknown. Note that we are uncertain if the culvert is designed for allowing the surface water to crossing the road or for expelling sub-road drainage.

A noticeable relatively stabilized slump scarp figures downslope of the point 045, a trench parallel to the slope can be followed down to the river.

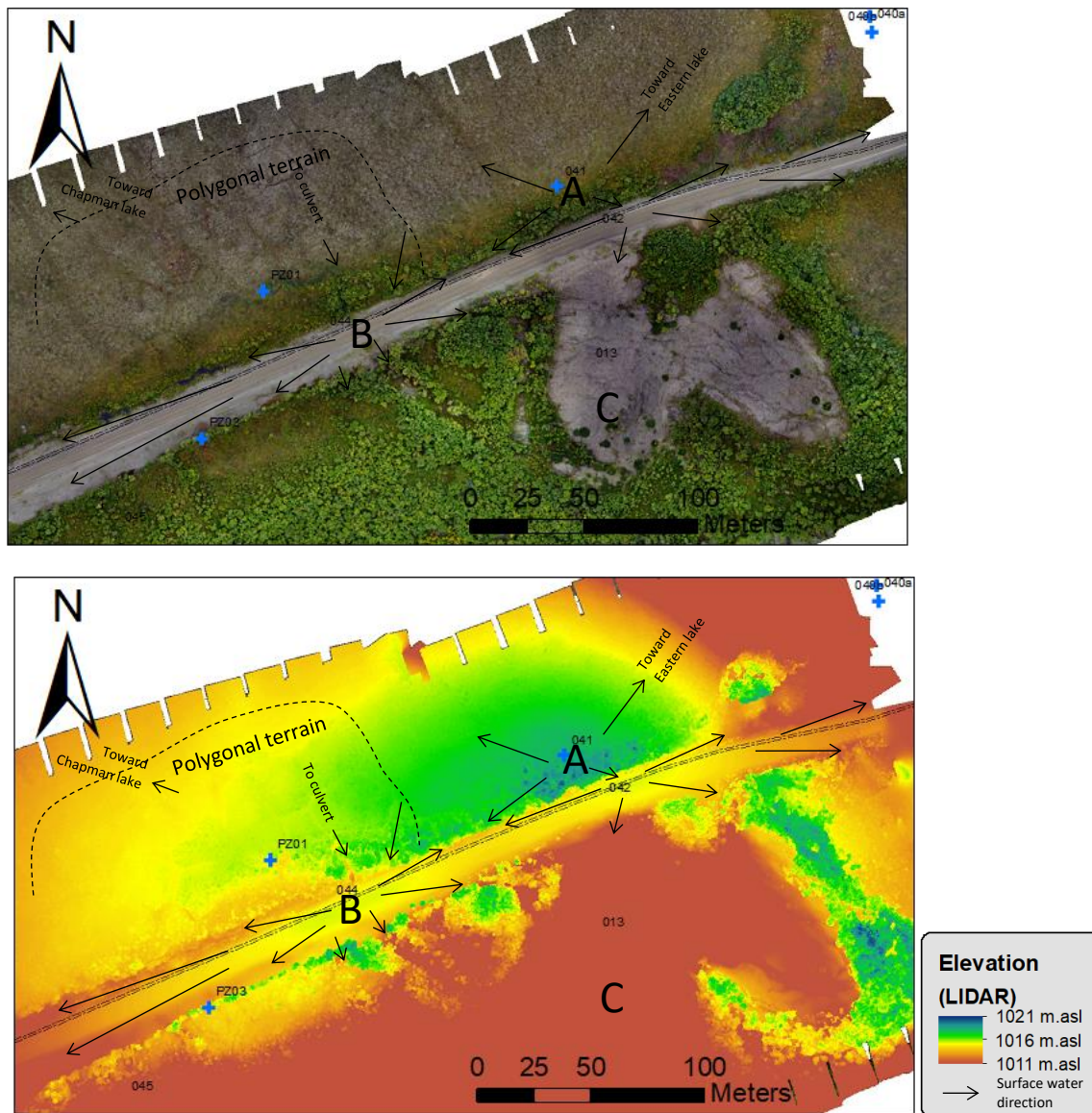


Figure 2 – Surface water direction map of zones A and B (Highest points, road and water-divides) printed on A) the aerial image derived from the drone survey and B) the elevation model from the same source.

The samples taken in this area are:

ID	Description
041	Soil water from the highest point
PZ01	Soil water from a high point on ridge
PZ03	Roadside surface water
D-BH-01	Deep borehole 20 m
D-BH-02	Deep borehole 20 m
D-BH-05	Deep borehole 25 m, sonic and CRREL recovery
046	Soil water from a flat section of a watertrack in a slump scarp
047	Surface water from the nearest tiny unactive river arm (first resurging water)
048	Surface water downstream the same river arm (collected resurging water)

1.2. Section C – Settling gravel pit

Figure 3 shows section C. The surface degradation of the old borrow pit appears as a crevasse-and-mound field with a 2-m scale microtopography and a 10-m scale topography. Note the orientation of the crevasse network; it goes along the slope in the eastern lobe while across the slope on the western one.

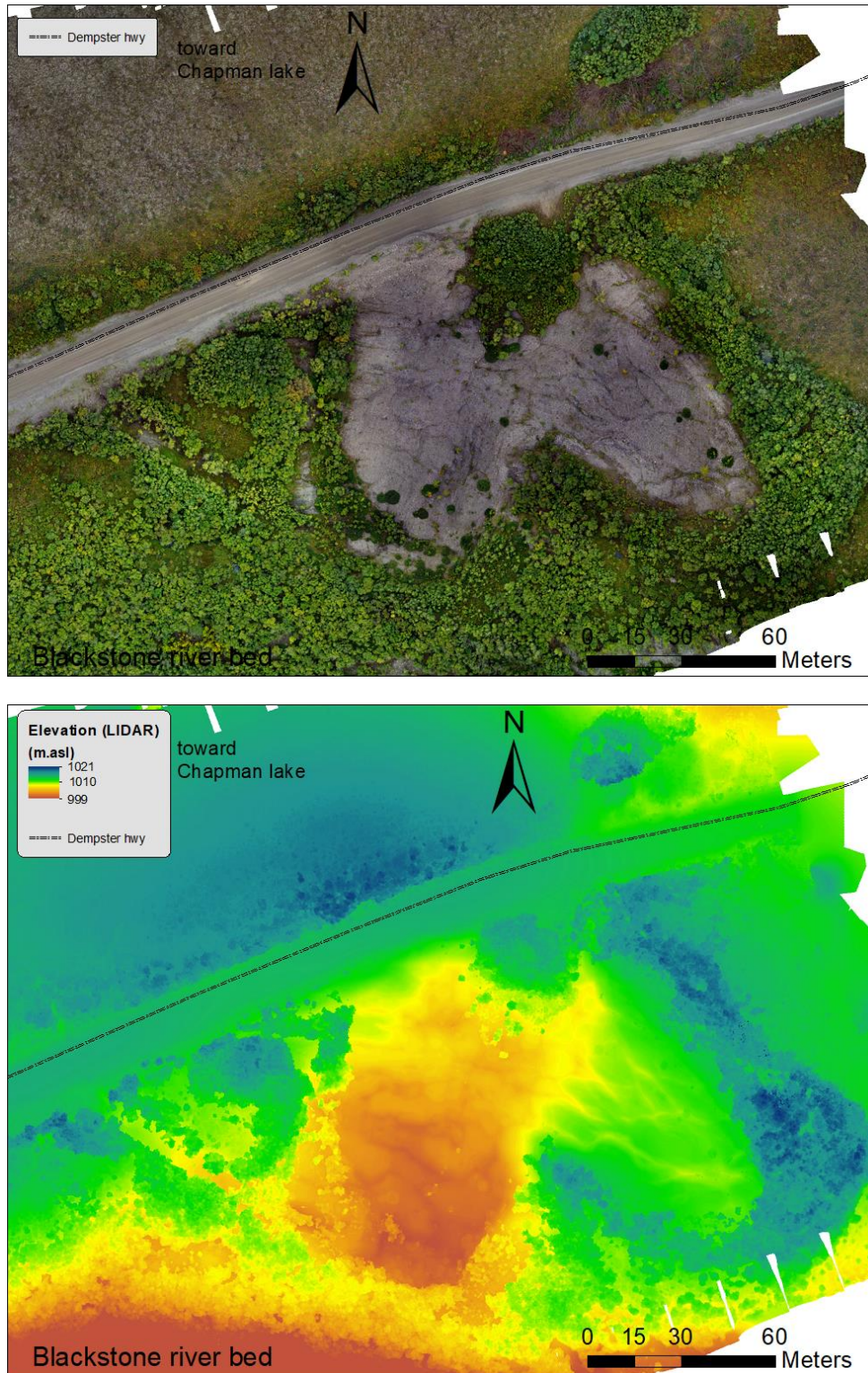


Figure 3 – Map of zones C (Gravel pit) printed on A) the aerial image derived from the drone survey and B) the elevation model from the same source.

An active tension crack (Figure 4) was observed on the riverside of the road, just upslope from the old gravel pit. There, the roadside embankment block descended about 4" since our arrival 4 days earlier.

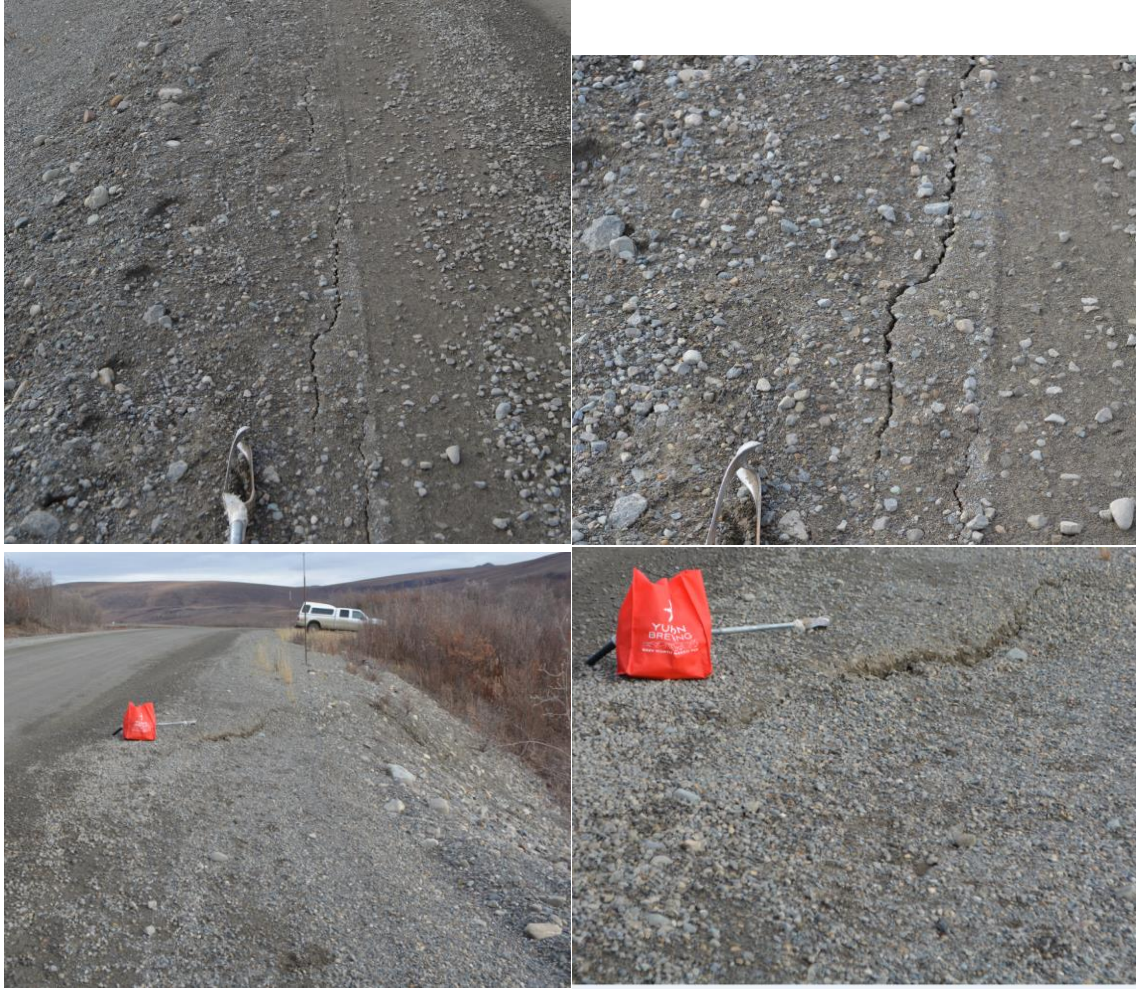


Figure 4 – Faults between the road and the gravel pit (4 different views of the same)

The surface water network upslope can be seen on the assessment of the on the Northeastern part. Nothing was sampled in this zone.

1.3. Section D – Eastern Lake

Figure 5 shows section D. The topography around the eastern lake is quite straightforward, the road passes on the water divide line, except where the hill was cut near the highest point. At this place the road ditches drain the water from the side of the hill cut. Where the road plays the role of the water divide, the surface water diverges toward the lake or the river depending on which side of the road it is. The situation of subsurface water is unknown. One could expect some downward groundwater movement along the road on the hill where it has been cut. There are two culverts crossing the road in this area, one at 019 and the other between the samples 014 and 017b. It is unsure if the culverts are designed send the surface water from one side of the road to the other, or if they serve to expel drainage water from the road's centerline.

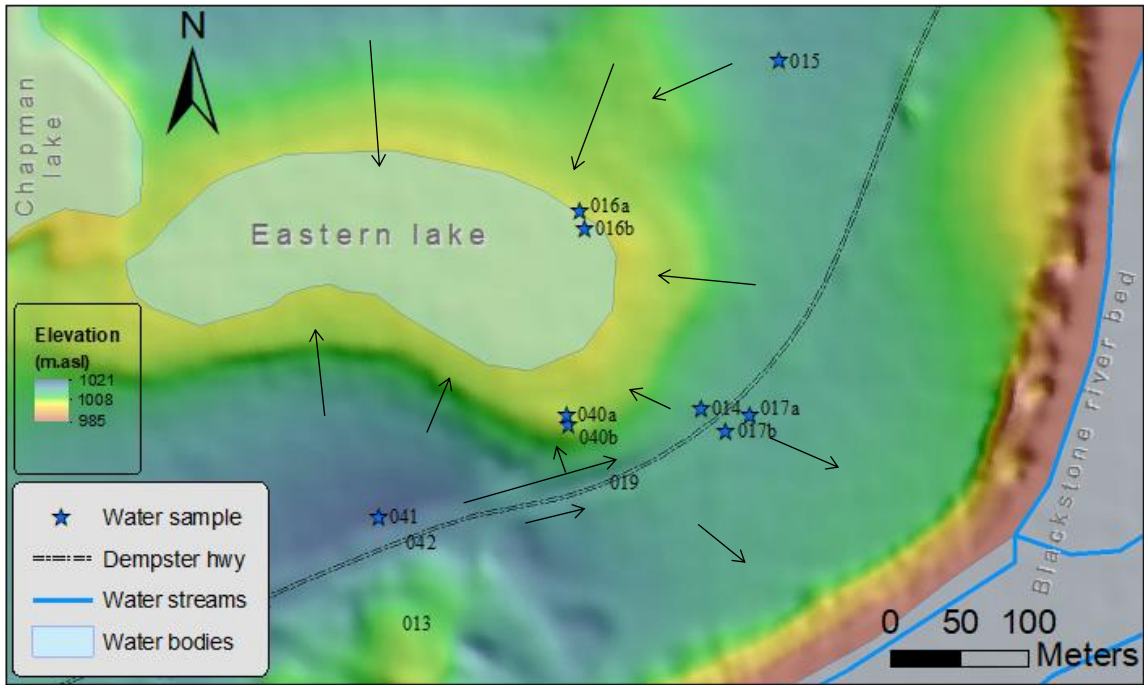


Figure 5 – Surface water direction map of zones D (Eastern Lake) printed on A) the default satellite image available in ArcGIS (ESRI database) and B) the elevation model from the Arctic DEM dataset in transparency overlying the hillshade terrain model.

The samples taken in this area are:

ID	Description
014	Roadside water flowing down a watertrack toward the lake
015	Headwater from a tiny 2-m wide pond
016a	Soil water from the saturated active layer near the lake (still 0.5 m higher)
016b	Surface water from the eastern lake
017a	Surface roadside water from the riverside
017b	Surface roadside water from the riverside
040a	Soil water from the saturated active layer near the lake (still 0.5 m higher)
040b	Soil water from the saturated active layer a bit upstream (0.5 m higher)

1.4. Sections E and F – Lakeside and riverside isthmus

Figure 6 shows sections E and F. This area consists in the thinner land strip between the lake and the river where the road sits. The road is the highest point and divides the surface water. Left-hand side drains toward the lake while the right-hand side drains toward the river. Many 3-5 m-diameter and 50-100 cm deep depressions were found in the gravel on the right-hand side of the road, giving an impression of thermokarst. Some were water filled and others were dry, they don't appear on the images or elevation models, pictures can be provided. The coarse and relatively rugged texture that appears on the DEM figure refers to bushy areas; the ground elevation is deductible from the minima observable in these areas.

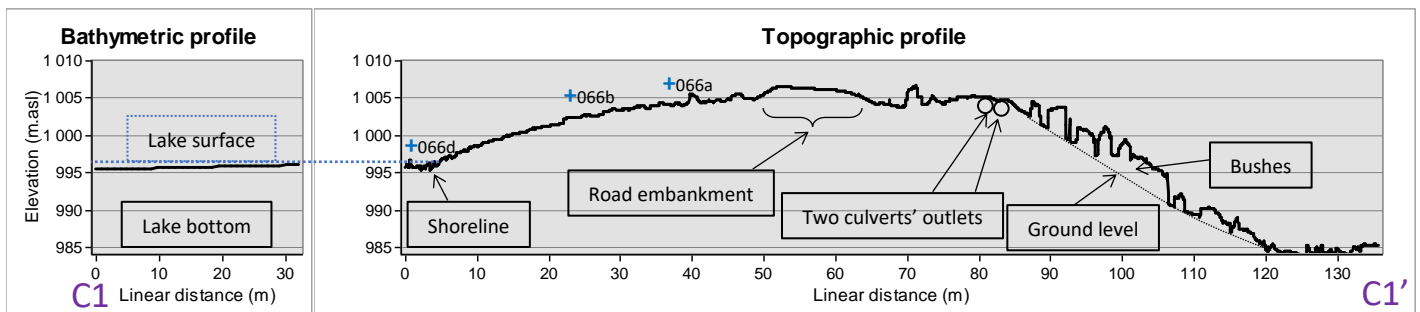
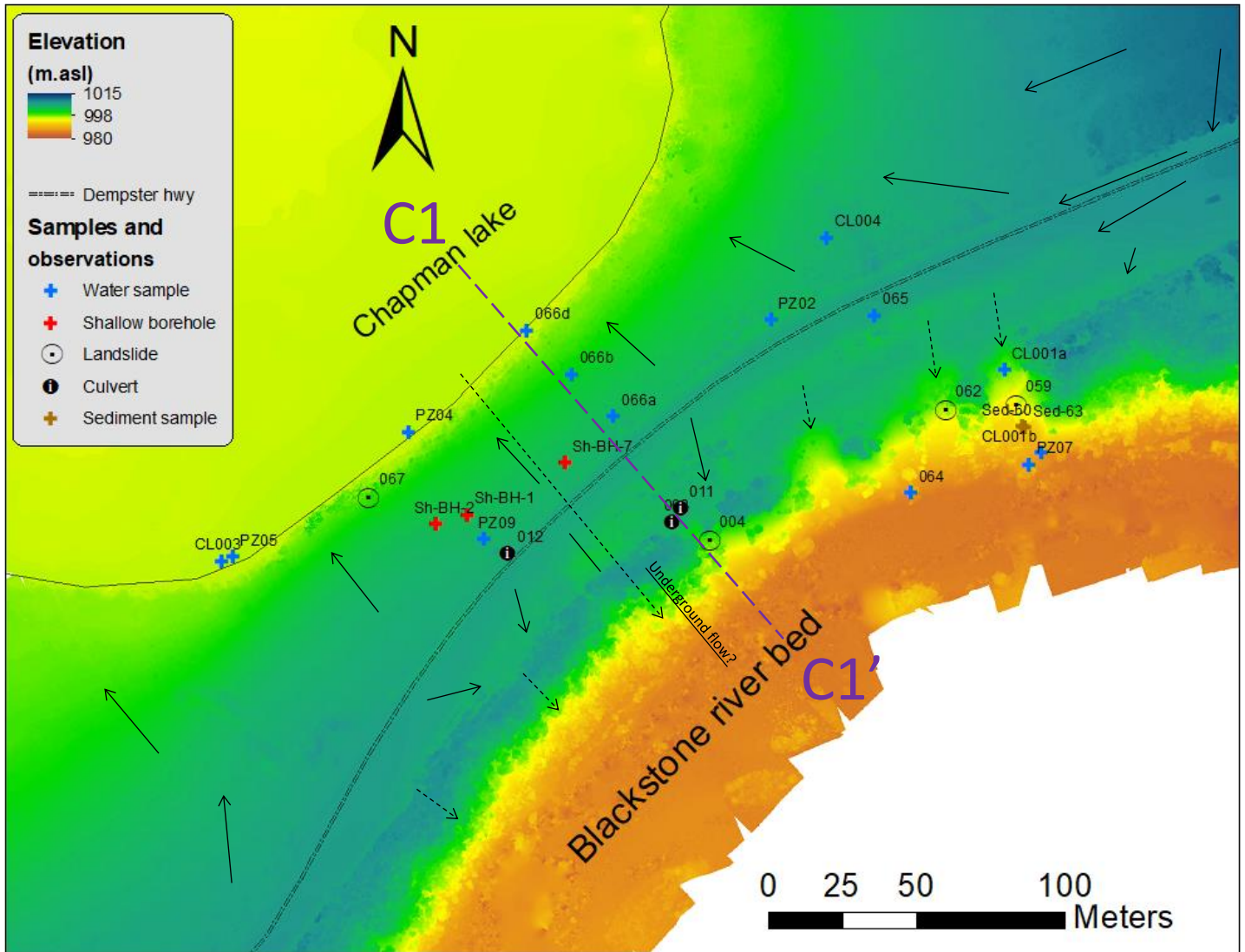


Figure 6 – A) Surface water direction map of zones E and F (Lakeside and riverside isthmus) printed on the elevation model from the drone survey and the bathymetric survey, B) Bathymetric and topographic profile C1-C1'. O66a, b and d are surface water samples.

The samples taken in this area are:

<u>ID</u>	<u>Description</u>
CL003	Lake water near the surface < 1 m from the shore in the summer (sampled by Pam)
PZ05	Lake water near the surface < 1 m from the shore
067 *	Head scarp of a small 2 m-wide slide
PZ04	Lake water near the surface < 1 m from the shore, end of a water track
PZ10	Lakeside moss water (near PZ04)
Sh-BH-2	Shallow borehole (155 cm-deep) in the sloping muskeg, not a water track
Sh-BH-1**	Shallow borehole (53 cm-deep) in the water track
PZ09	Roadside water on the lakeside, upper part of the above water track (Sh-BH-1)
012	Apparent culvert outlet on the side of the embankment
Sh-BH-7	Shallow borehole (217 cm-deep) in the slightly sloping muskeg, not a water track
066d	Lake water near the surface < 1 m from the shore, rainy day
066b	Soil water in a water track at the level of the slope shoulder, rainy day
066a	Soil water in a water track above the slope shoulder, rainy day
003	Culvert collapsing with the bank
011	Culvert collapsing with the bank (same?)
004	Bank is collapsing
PZ02	Roadside water on the lakeside, apparently in the ditch
CL004	Soil water from the bottom of the active layer in the summer (sampled by Pam)
065	Roadside water on the riverside, in a thermo-erosion crevasse-like depression on a rainy day
062	Bank is collapsing
064	River sample on a rainy day
CL001a	Seepage water in the summer, upper level (sampled by Pam)
059	Bank is collapsing
Sed-60	Sediment sample, sand?
Sed-63	Sediment sample, layered clayey silt
CL001b	Seepage water in the summer, lower level (sampled by Pam)
PZ07	River water
PZ08	River water
CL002a,b	River water in the summer (sampled by Pam)

* A quasi-continuous 2 inches-wide fault can be followed all along the same elevation level, proposing that the slope slowly slides down

** The drill broke on a stone, there had many cobbles left in the hole

1.5. Sections G and H – Polygon field and riverbank

Figure 7 shows sections G and H, and Figure 8 shows the zoomed in section of R1.

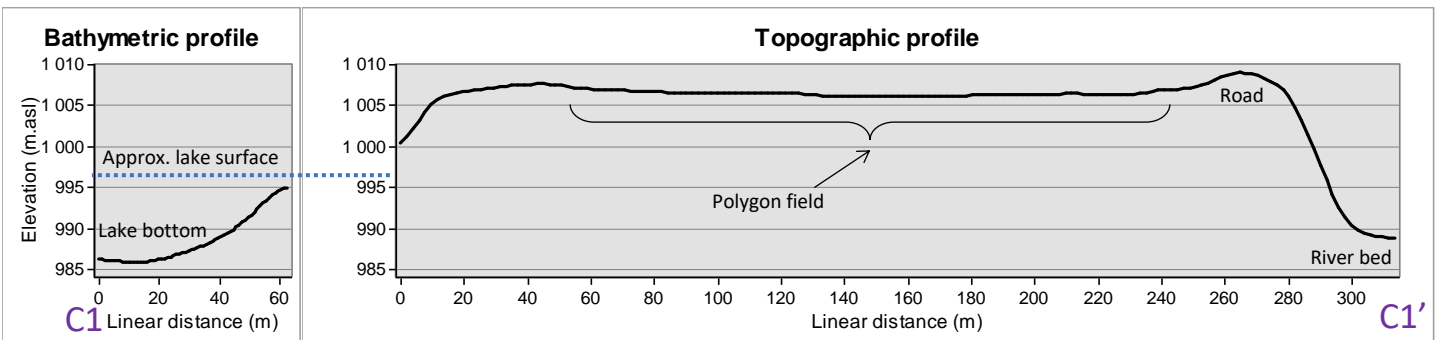
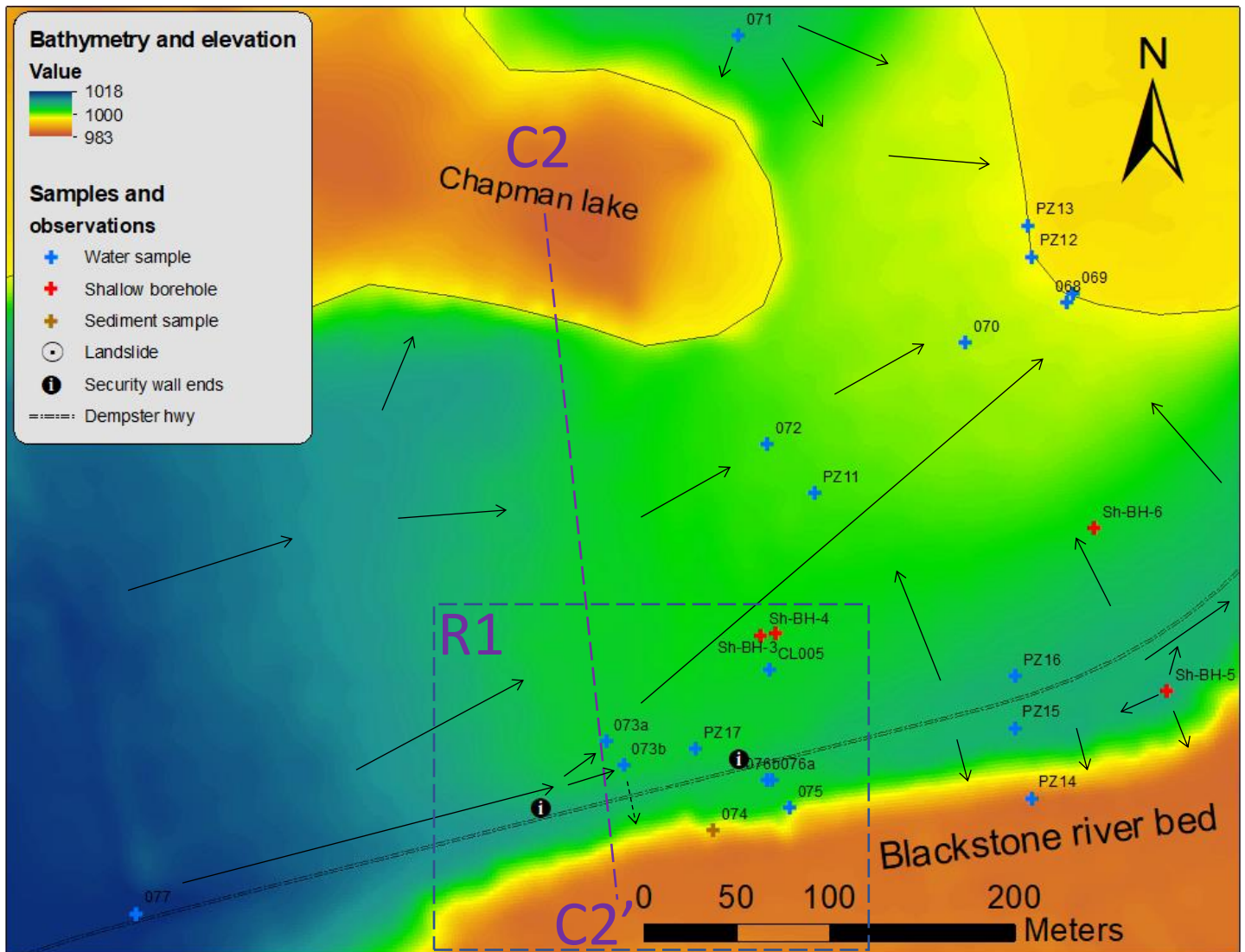


Figure 7 – A) Surface water direction map of zones G and H (Polygon field and riverbank) printed on the elevation model from the Arctic DEM dataset and the bathymetric survey, B) Bathymetric and topographic profile C2-C2'. Note that R1 zoom windows refers to Figure 8 on a following page.

Note that there is a misfit between the ArcticDEM and the bathymetric survey because it was ground-adjusted on the LIDAR DEM at a single shore location but both DEM are not identical. Despite the 5 m-underestimation, the lake's bottom elevation remains similar to that of the river bottom.

The samples taken in this area are:

ID	Description
O77	Surface water of the western pond <1 m from the shore, rainy day
073a	Surface water in a polygon through, just downstream the water divergence, toward the polygon field, rainy
073b	Roadside water, just downstream the water divergence, rainy day
PZ17	Roadside water, just downstream the 073b
074	Thick clean sand sample from the bank, rainy day
076a	Roadside water in a 3 m-deep crevasse-like depression, rainy day, covered in ice and then, rainwater
076b	Ice cover on 076a, rainy day (rain water at the ice surface was not sampled)
075	Flowingepage water at the headscarp of a >2 years old slide scar (trees recovered), rainy day
Sh-BH-3	Shallow borehole in the center of a plygon, 237 cm-deep
Sh-BH-4	Shallow borehole in the polygon through just beside Sh-BH-3, 174 cm-deep
CL005	Active layer water in a wet section of the polygon field, july 2019
071	Soil water from the highest point (headwater) on a peninsula extending in the Chapman lake, rainy day
072	Soil water from the upper midslope of the polygon field, in a through, rainy day
PZ11	Soil surface water from the upper midslope of the polygon field, in a through
PZ16	Roadside water from a quite big pond just down the embankment toe
PZ15	Roadside water from a quite big pond downslope a veryshort watertrack
PZ14	River water
070	Soil surface water from the lower midslope of the polygon field, in a through, rainy day
PZ13	Lakeside moss water
PZ12	Lake water <1 m from the shore
068	Soil surface water from lower end of the polygon field, in a through 0.5 m above the lake level, rainy day
069	Lake water <1 m from the shore, rainy day
Sh-BH-6	Shallow borehole in a steeper sideslope, 155 cm-deep
Sh-BH-5	Shallow borehole at a headwater location, 209 cm-deep

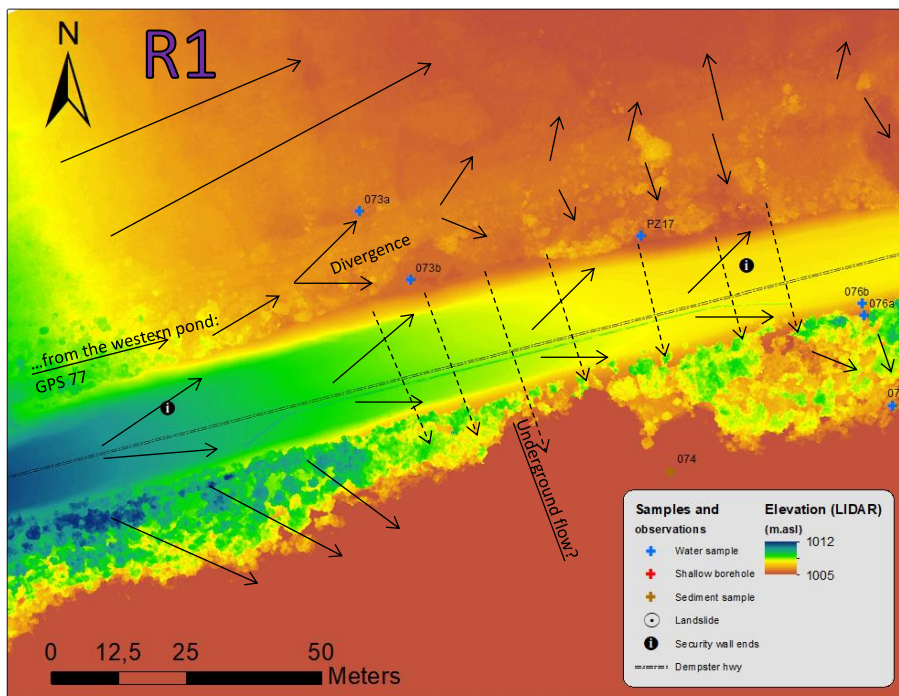


Figure 8 – Surface water direction map of the zoom window R1 (see Figure 7A) printed on A) the aerial image from the drone survey and B) the elevation model from the same source.

Section 3.2.1 Appendix C :

Soil and permafrost table cryostratigraphy

Michel Sliger and Daniel Fortier

January 2022

Edited by: Frances Amyot

1. Introduction

The shallow boreholes at the Chapman Lake site (Figure 1) were all drilled using the methodology described in Calmels et al (2005) on October 28 and 29th, 2019. The cores were extracted, scraped for cleaning, photographed and described in situ. They were kept frozen in a cooler for transportation and preserved in a freezer until subsampling and further analyses.

The active layer and sediment samples were taken using a trowel or by hand and were preserved frozen and refrigerated until further analyses.

The pH, the major cation content and the electrical conductivity of the dilution water was measured for a selection of samples. The grain-size distribution of some selected samples was measured. The organic matter content by loss-on-ignition was measured on every sample.

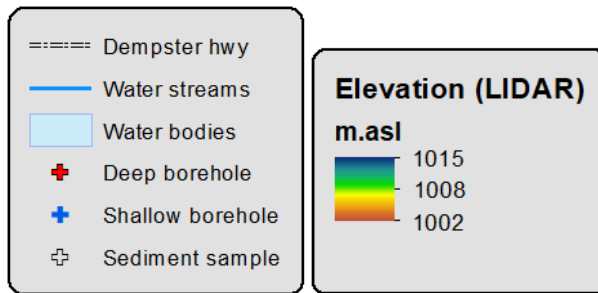
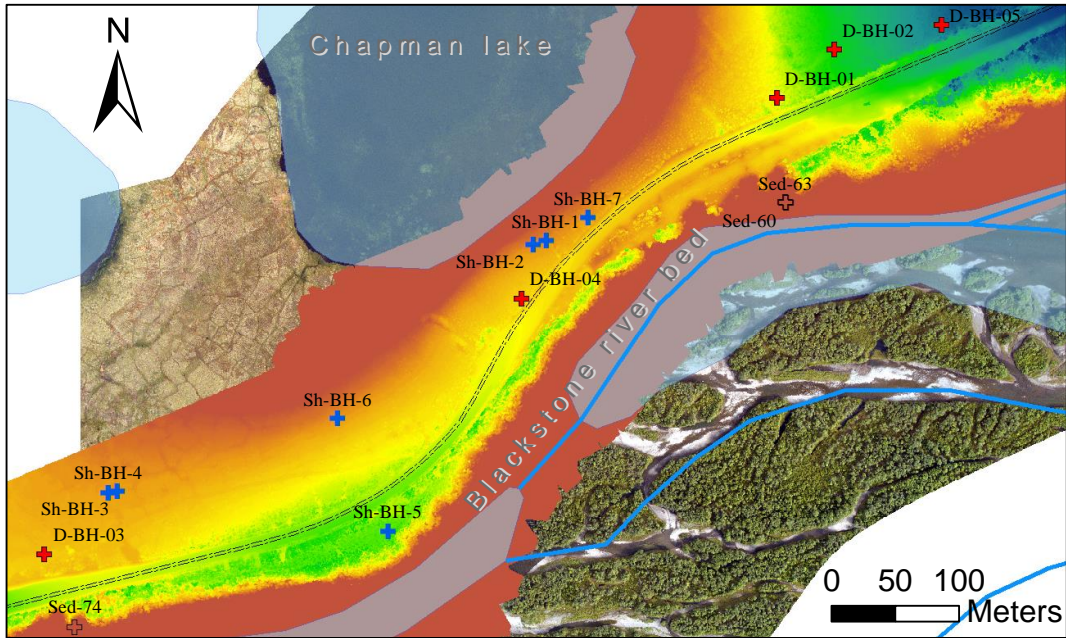
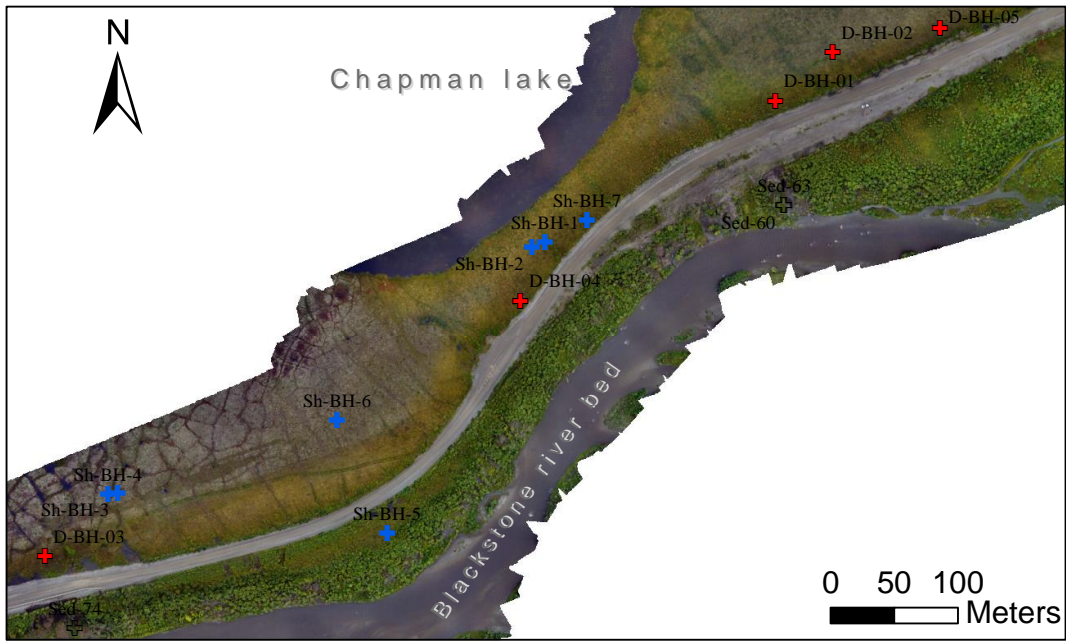


Figure 1 – Maps of the boreholes printed on the aerial image from the drone survey and B) from the elevation model derived from the same source displayed over the default image from ArcGIS (ESRI database). Sh-BH are for shallow boreholes (about 2 m-deep), D-BH are for deep boreholes (about 20 m-deep) and Sed are from sediment samples.

1.1. Shallow borehole: water track

Borehole 1 is located on the isthmus, in the upper part of the western water track that links the road culvert to the lake. This borehole intersects the upper ERT survey parallel to the lakeshore.

The vegetation in the water track is sedge tussock surrounded by moss (mostly besides the water track). There is more and higher willows in the water track than around.

The elevation of the water track surface is around 0.5 m lower than around.

Borehole log

The borehole is right under a tussock, and cryoturbation is likely. The drill broke on the pebbly layer preventing further drilling.

0-7 cm	Moss (the tussock was excavated)	No grainsize	OM (0-15) = 2.3 %
7-33 cm	Moss roots and fibrous peat, irregular upper and lower contact lines following the tussock's microtopo	No grainsize	OM (15-23-33) = 3.2 & 3.6 %
33-43 cm	Sandy clayey gravelly silt, grey-brown, saturated, upper contact gradual and patchy		OM (38-43) = 11.8 %
	<i>Frost level: 43 cm</i>	<i>Water level: 25 cm</i>	
43-53 cm	Sandy rounded gravels and pebbles		

Samples

0-15 cm	15-23 cm	23-33 cm	38-43 cm	
---------	----------	----------	----------	--

1.2. Shallow borehole 2: plain sloping muskeg

Borehole 2 is located on the 'lakeside' isthmus, in the plain muskeg just beside the water track. It is also in the slope shoulder. This borehole also intersects the upper ERT survey parallel to the lakeshore.

The vegetation is mainly composed by moss, sedge tussock and sparse and short willows.

Borehole log

Cryoturbation is likely. In order to prevent the drill from breaking on a deeper layer, drilling ended in a layer of massive ice.

0-7 cm	Moss, irregular lower contact line		
7-20 cm	Moss roots and fibrous peat		
20-35 cm	Brown silt		OM (20-33-35) = 15.0 & 3.9 %
	<i>Frost level: 35 cm</i>	<i>Water level: No water</i>	
33-90 cm	Organic brown silt and peat cryoturbated patches, porous invisible ice in the peat and finely reticulate ice in the silt		OM (33-67-101) = 12.4 & 11.7 %
90-135 cm	From top to bottom: grey silt to fine sand, reticulate ice to lenticular ice		OM (101-116) = 1.9 %
135-143 cm	Grey silty sand, porous invisible ice		OM (116-143) = 3.0 %
143-155 cm	Massive ice		OM (143-155) = 2.5 %

Samples

0-20 cm	20-33 cm	33-35 cm		
33-67 cm (#1)	67-101 cm (#2)	101-116 cm (#3)	116-143 cm (#4)	143-155 cm (#5)

1.3. Shallow borehole 3: upslope polygon center

Borehole 3 is located in the center of a polygon (15-20 m wide) located in a wetter portion of the upper part of the polygonal field. This wetter portion appears to support the water flow from the hill and the road ditch at the west.

The vegetation is mainly composed by moss, lichen, sedge, short willows, Labrador tea and cranberries.

Borehole log

The borehole is under the highest point, and cryoturbation is likely. In order to prevent the drill from breaking on a deeper layer, drilling ended in a layer of massive ice.

0-15 cm	Moss + root, light brown		
15-32 cm	Peat + root, brown		OM (15-33) = 53.6 %
32-37 cm	Dark brown peat		
37-42 cm	Almost black peaty silt		
	<i>Frost level: 42 cm</i>	<i>Water level: No water</i>	
42-140 cm	Brown silty peat horizontally layered, porous visible ice, some singular ice lenses		OM (42-76-101-124) = 28.3, 85.0 & 35.7 %
140-150 cm	Brown silt and peat cryoturbated patches, porous invisible ice in the peat and microlenticular ice in the silt, some singular ice lenses with a slight tilt		OM (140-150) = 18.2 %
150-182 cm	Brown silty peat layered and increasingly sloping, porous visible ice, apparent horizontal singular ice lense at 178 cm (to confirm)		OM (150-180) = 76.8 %
182-213 cm	Brown peat wedged in grey silt (very inclined sharp contact), porous invisible ice to microlenticular in the peat (to confirm) and microlenticular ice in the silt, the cryostructure appears to be relatively horizontal		OM (180-201) = 11.1 %
213-237 cm	Massive ice		OM (213-237) = 4.6 %

Samples

0-15 cm	15-32 cm	32-42 cm		
42-76 cm (#6)	76-101 cm (#7)	101-124 cm (#8)	124-150 cm (#9)	150-180 cm (#10)
180-213 cm (#11)	213-237 cm (#12)			

1.4. Shallow borehole 4: upslope polygon trough

Borehole 4 is located in the trough of the same polygon as the previous borehole. The polygon's trough is about 0.3 m lower than the surroundings, and it is about 1.5 m-wide.

The vegetation is mainly composed of moss, lichen and sedge tussocks.

Borehole log

The active layer sampled directly is in the trough, where there was too much water to drill. Cryoturbation is likely. In order to prevent the drill from breaking on a deeper layer, drilling ended in a layer of massive ice.

0-52 cm	Peat (1 st hole, discontinued because of flooding in the trench)		
	The borehole is under a higher point just beside the saturated trench (<1m beside)		
0-30 cm	Moss + peat		OM (5-20) = 20.2 %
30-41 cm	Peaty silt		
	<i>Frost level: 41 cm Water level: approx. 40 cm (near the bottom)</i>		
41-100 cm	Dark to lighter peat (from top to bottom), diagonally layered, tilt increases with depth, porous invisible ice		OM (41-77) = 66.3 %
100-125 cm	Grey sand and silt, diagonally layered, reticulate ice, some thicker ice lenses with similar tilt, upper and lower sharp inclined contact, its tilt is similar to the overlying peat layers		OM (77-116) = 38.7 %
125-150 cm	Brown and grey sand, porous invisible ice, some ice veins		OM (116-142) = 3.7 %
150-157 cm	Grey sand and silt, reticulate ice, thicker ice lenses with similar tilt at the bottom of unit, upper gradual inclined and lower sharp inclined contact, their tilt is similar to the overlying mineral layers		OM (142-165) =4.0 %
157-174 cm	Massive ice with lots of bubbles		

Samples

? cm	? cm	? cm		
41-77 cm (#13)	77-116 cm (#14)	116-142 cm (#15)	142-165 cm (#16)	167-174 cm (#17)

1.5. Shallow borehole 5: headwater

Borehole 5 is located in an upper area in the natural ground, just between the convex side of the road and the middle point between the riverside isthmus and the upstream riverbank hydro-systems. This borehole is located at the highest point of the relative elevation; it is a headwater location.

The vegetation is mainly composed by moss, sedge, willows, and taller unknown bushes. The borehole was drilled in the moss.

Borehole log

The borehole is under the moss, at the highest relative elevation. Cryoturbation is likely. In order to prevent the drill from breaking on a deeper layer, drilling ended in a layer of massive ice.

0-8 cm	Moss		
8-15 cm	Peat + moss root		OM (0-20) = 2.4 %
15-60 cm	Silt with sparse gravels (and pebbles?), grey with orange rust marbling, relatively deep roots		OM (20-30-50) = 3.1 & 4.0 %
	<i>Frost level: 60 cm</i> <i>Water level: no water</i>		
69-105 cm	Patchy grey silt-fine sand and brown peat, and charcoal marbling, porous invisible ice in peat and microlenticular ice in silt		OM (69-99) = 32.9 %
105-122 cm	Grey sand and silt with sparse gravels, reticulate ice, a thicker tilted ice lens at the bottom, lower sharp contact, upper contact is relatively gradual		OM (99-130) = 7.9 %
122-150 cm	Patchy grey silt-fine sand with sparse gravels, and brown peat, porous visible ice in peat and reticulate to microlenticular ice in silt		OM (130-155) = 11.5 %
150-188 cm	Grey pebbly-sandy silt, pebbles are rounded, lenticular ice, sharp and horizontal upper contact		OM (155-188) = 5.7 %
188-209 cm	Pebbly-gravelly sand-silt, microlenticular and crustal ice		OM (188-209) = 3.3 %

Samples

0-20 cm	20-30 cm	40-50 cm		
69-99 cm (#18)	99-130 cm (#19)	130-155 cm (#20)	155-188 cm (#21)	188-209 cm (#22)

1.6. Shallow borehole 6: steeper sideslope

Borehole 6 is located in a poorly expressed polygon (15-20 m wide) located on the slope shoulder, where it slightly increases (between the shoulder and the inflexion point), at the southern margin of the polygonal field.

The vegetation is mainly composed by moss, lichen, sedge, short and taller willows, Labrador tea and cranberries. The tussocks and taller willows upslope don't look healthy.

Borehole log

The borehole is under the highest point. Cryoturbation is likely. In order to prevent the drill from breaking on a deeper layer, drilling ended in a layer of massive ice.

0-15 cm	Moss + root moss		OM (0-20) = 33.6 %
15-32 cm	Peat + root moss, very water conducive		OM (20-30) = 4.0 %
32-42 cm	Brown silt		OM (30-40) = 3.6 %
	<i>Frost level: 42 cm</i> <i>Water level: 21 cm</i>		
42-61 cm	Brown peaty silt diagonally layered, porous visible ice to lenticular, a horizontal ice band near the bottom intersecting the sharp oblique lower contact		OM (42-78) = 8.8 %
61-75 cm	Beige organic silt, microlenticular ice, sharp lower contact (flat or oblique in another direction?)		
75-81 cm	Grey sandy silt, reticulate ice		OM (78-115) = 5.0 %
81-102 cm	Grey sandy silt, some organic marbling, microlenticular ice, sharp flat upper contact marked by a singular ice lens (81 cm), some veins go across, down to a second singular flat lens (87 cm), there is a third one (97 cm)		
102-112 cm	Tilted layered grey sandy silt and brown peaty silt, gradual upper and lower contacts		
112-124 cm	Grey sandy silt, horizontal microlenticular ice, some diagonal veins connect a singular ice lens marking the flat sharp lower contact		
124-138 cm	Grey sandy silt, diagonal microlenticular ice, singular ice lens marking the oblique sharp lower contact		OM (115-141) = 2.3 %
138-155 cm	Massive ice		

Samples

0-15 cm	15-32 cm	32-42 cm		
42-78 cm (#23)	75-115 cm (#24)	115-141 cm (#25)	141-155 cm (#26)	

1.7. Shallow borehole 7: plain muskeg

Borehole 7 is located in the natural ground just beside the road in a wet area that appears to be water-fed by the roadside catchment but it does not appear as a water track. The terrain is slightly sloping at this point.

Note that just downslope, on the shoulder, there is a longitudinal crack that is not necessarily new but it is clear from the vegetative microtopography. It must be significant enough to be expressed despite the thick moss and peat cover.

The vegetation is mainly composed by moss, short and taller willows.

Borehole log

Cryoturbation is likely. In order to prevent the drill from breaking on a deeper layer, drilling ended in a layer of massive ice.

0-17 cm	Moss + root moss		
17-27 cm	Peat + root moss		OM (17-27) = 2.6 %
32-42 cm	Grey sandy silt with roots		OM (27-45) = 6.2 %
	Frost level: 42 cm	Water level: no water	
42-100 cm	Grey sandy silt and brown silty peat cryoturbation-like patches, porous visible to invisible ice in the silty peat and banded to lenticular ice in the silt, gradual but quick transition to the lower unit		OM (42-85-113) = 10.2 & 10.4 %
100-140 cm	Grey sandy silt with an oxidation zone in the middle, banded to lenticular ice, mostly away from the oxidation zone		OM (113-148) = 8.4 %
140-190 cm	Diffuse sandy silt and ice mixture, not much apparent air bubble, oblique sharp lower contact		OM (148-177) = 8.4 %
190-217 cm	Brownish grey pebbly sand, porous invisible ice and overlying crustal ice, pebbles are sub-rounded		OM (177-214) = 11.1 %

Samples

0-17 cm	17-27 cm	27-45 cm		
42-85 cm (#27)	85-113 cm (#28)	113-148 cm (#29)	148-177 cm (#30)	177-214 cm (#31)

2. References

Calmels, F., et al. (2005). "A portable earth-drill system for permafrost studies." Permafrost and Periglacial Processes **16**(3): 311-315.

Section 3.2.1 Appendix D: Deep borehole analysis

Michel Sliger and Daniel Fortier

January 2022

Edited by: Frances Amyot

1. Introduction

The deep boreholes were drilled between 2017 and 2019. All the cores (Chap2, Ch2) are from BH02. A graph depicting the organic matter from the borehole Chap 2 can be seen in Figure 1 below.

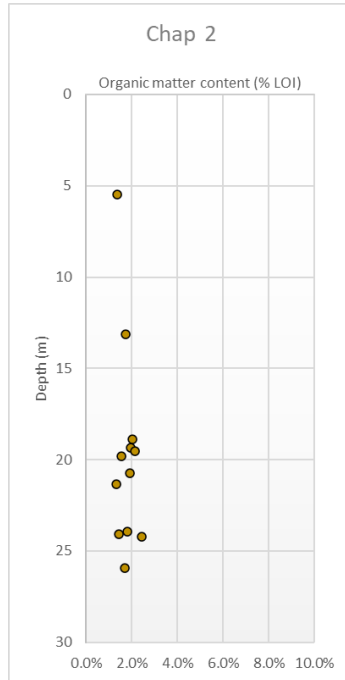


Figure 1 – Organic matter content of the sediments in the core Chap 2, acquired by Loss-on-ignition

1.1. Crystallography

The crystallographic analysis of the pure ice is based on pictures taken using a reflex-type Nikon camera on a tripod in a freezing room. The ice samples were sliced along relevant axis at selected points in order to initiate the thin section. The slice was then stuck on a frozen glass plate complemented with gauges at corners for uniformizing the next step: thermoeroding the thin section to a given thickness by rubbing it against a flat stainless-steel plate and absorbing away the resulting excess meltwater. Once ready, the thin section was then put in between two light-polarizing filters (showing different angle difference) over a light-table. The different crystals were then exposed by different colors and the display was then photographed using a constant camera setting for allowing comparison among the dataset.

For each massive ice sample two thin sections were analysed, one for the plane horizontal to the ground surface (H) and one for the vertical (V).

1.1.1. Ice block

The ice block seen in Figure 2 is the one that was cut using a chainsaw in the exposure of the eroding cliff during the spring of 2017. The ice is clear and bubble-rich, the bubbles are elongated and the crystals are medium equigranular, mostly subangular and the H-plane tend to appear with a similar hue (green-to-blue) under polarization, suggesting a preferential angle.

The smaller more spherical crystals in the periphery of the V-plane are thought to be refrozen and/or metamorphosed since the original sampling.

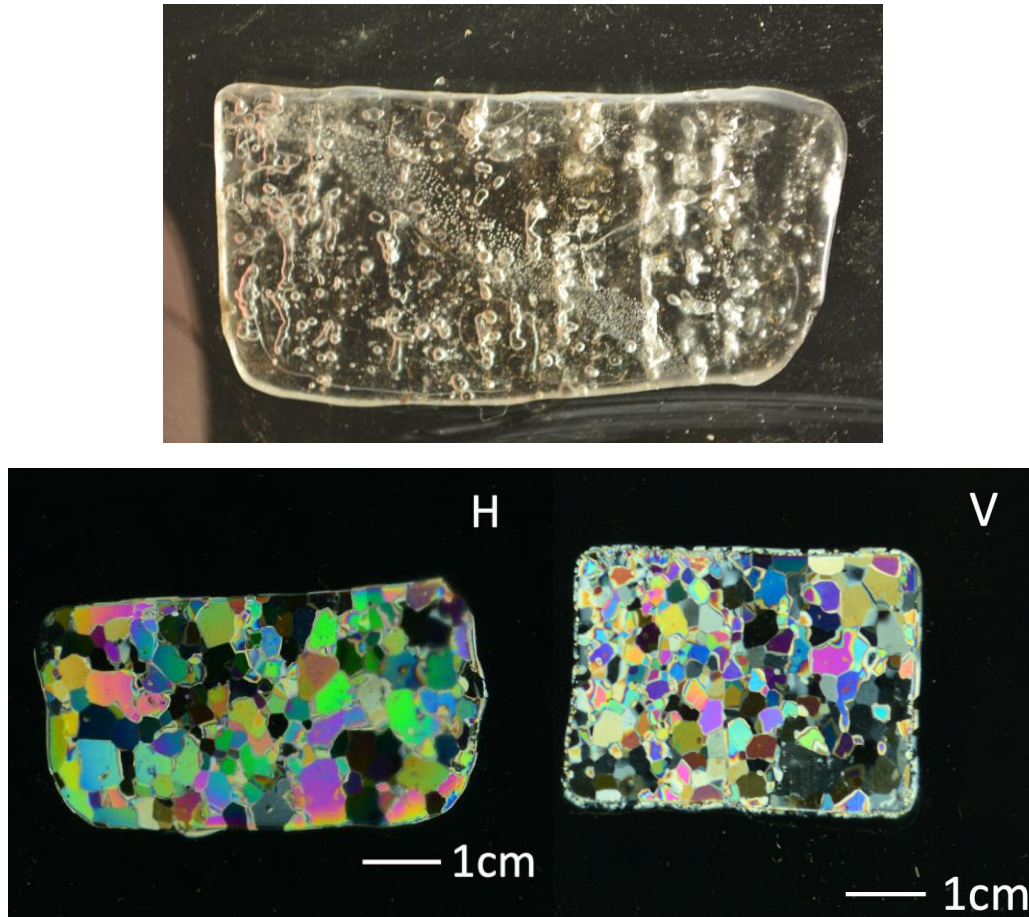


Figure 2 – Horizontal thin section of the ice block seen under A) the natural light and B) polarized light. C) Vertical thin section seen under polarized light.

1.1.1.1. Ch1-71'

The massive ice subsample of Chap1-71' seen in Figure 3 shows ice that is clear but has a brown shade in some areas, indication some fine sediments. It is bubble-rich, with smaller round bubbles that are broadly distributed and other bigger ones that are elongated and diagonally organized.

On the H-plane the crystals are medium-to-big, subhedral, and appear with a random hue except near at the bottom-left corner where two clusters appear in two different hues (yellow and blue). The big crystals of these two clusters are almost exactly aligned in the same direction.

On the V-plane the crystals appear medium-to-big-sized and their dominant hue appears from yellow to pink, suggesting a slight gradation in the crystals' orientation.

The smaller more spherical crystals in the periphery of the V-plane are though to be refrozen and/or metamorphosed.

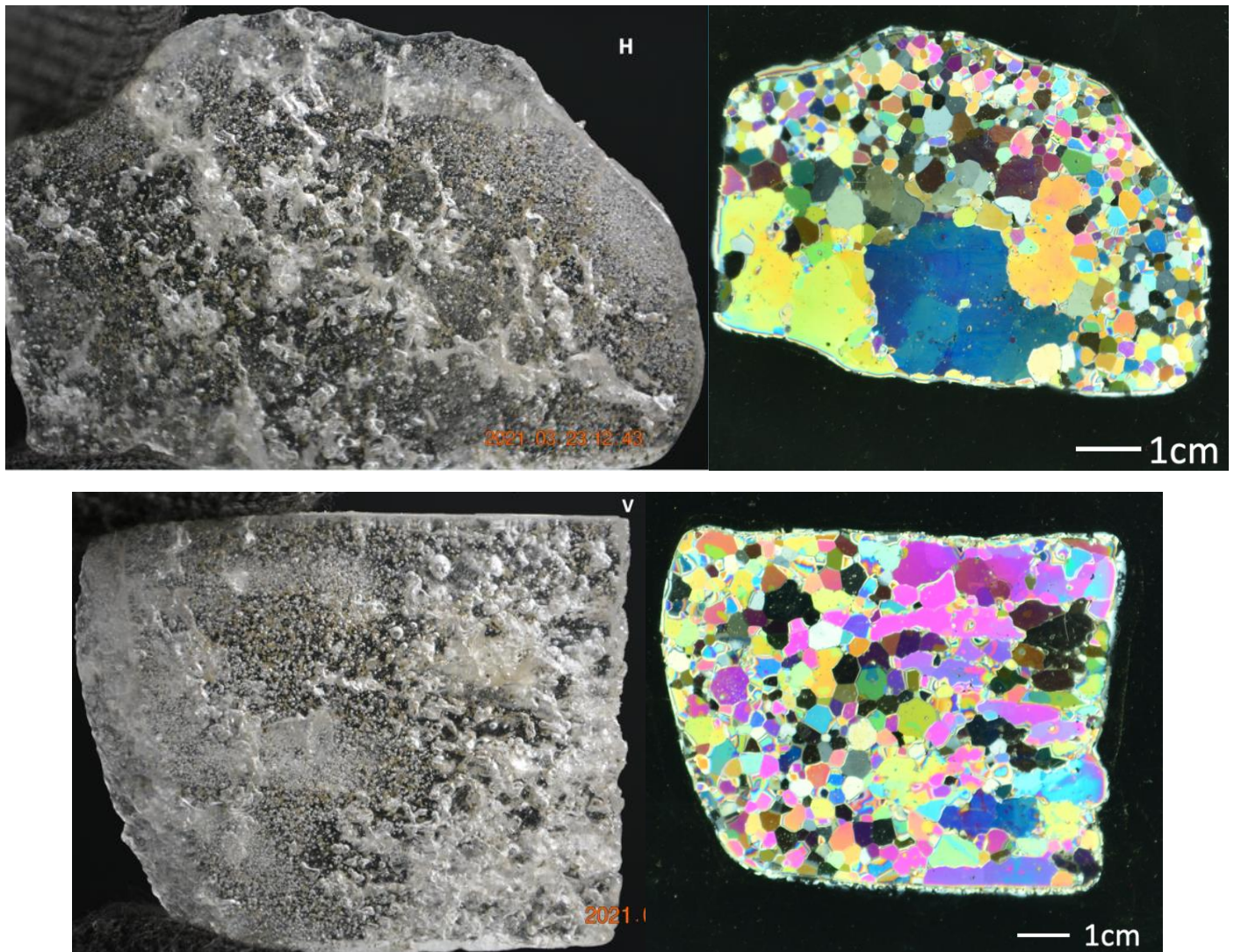


Figure 3 – A) Horizontal thin section of Chap1-71' seen under the natural light and B) polarized light. C) Horizontal thin section of Chap1-71' seen under the natural light and D) polarized light.

1.1.1.2. Ch1-73'

The massive ice subsample of Chap1-73' seen in Figure 4 shows ice that is clear but has a brown shade in the center, which is indicative of fine sediments. It is bubble-rich, with smaller round bubbles that are broadly distributed and other bigger ones that are elongated and clustered. The pattern changes with depth.

On the H-plane the crystals are big, subhedral, and appear with a similar hue (from blue to yellow), except near the middle where a cluster appears in orange. The uniform hue suggests a preferential angle. Crystals are generally big in the center and diminish in size toward the periphery.

On the V-plane the crystals appear medium-sized, equigranular and their dominant hue appears almost random but a slight gradation in the color dominance seems to appear from top-left corner of the picture to its bottom-right corner.

The smaller more spherical crystals in the periphery of the V-plane are thought to be refrozen and/or metamorphosed.

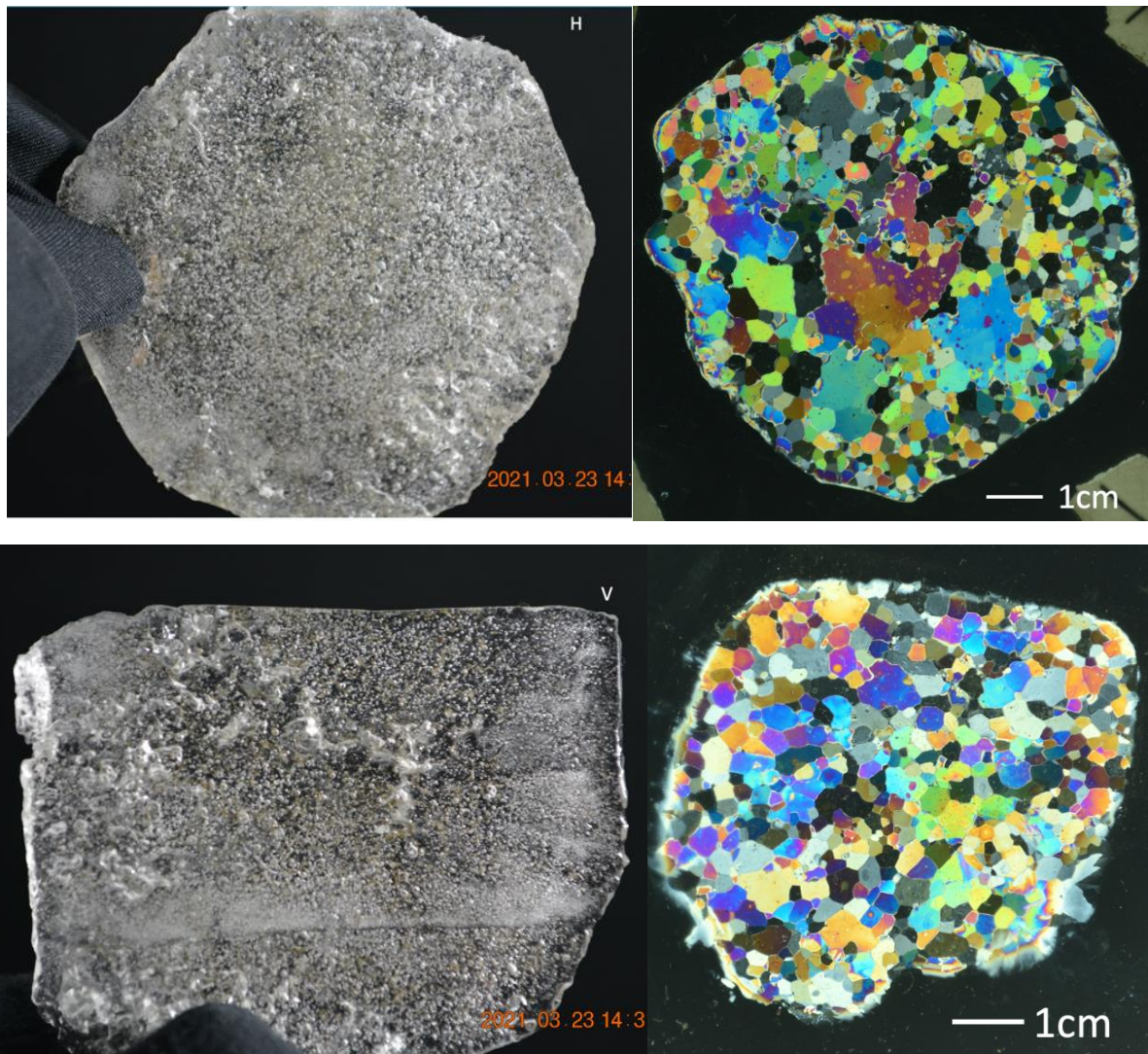


Figure 4 – A) Horizontal thin section of Chap1-73' seen under the natural light and B) polarized light. C) Horizontal thin section of Chap1-73' seen under the natural light and D) polarized light.

1.1.1.3. Ch1-75'

The massive ice subsample of Chap1-75' seen in Figure 5 shows ice that is clear but has a brown shade in the center, which is indicative of fine sediments. It is bubble-rich, with smaller round bubbles that are broadly distributed and other bigger ones that are elongated and clustered.

On the H-plane the crystals are big, subhedral, and appear in grey-tone in the center and diminish in size toward the periphery, and express heterogeneous and evenly distributed colors.

The smaller more spherical crystals in the periphery of the V-plane are thought to be refrozen and/or metamorphosed after the original sampling. The bigger darker crystals at the center may be a consequence of a section too thin.

On the V-plane the crystals appear medium-sized, equigranular and have a relatively uniform hue (pink-to-yellow) under polarization, suggesting a preferential angle.

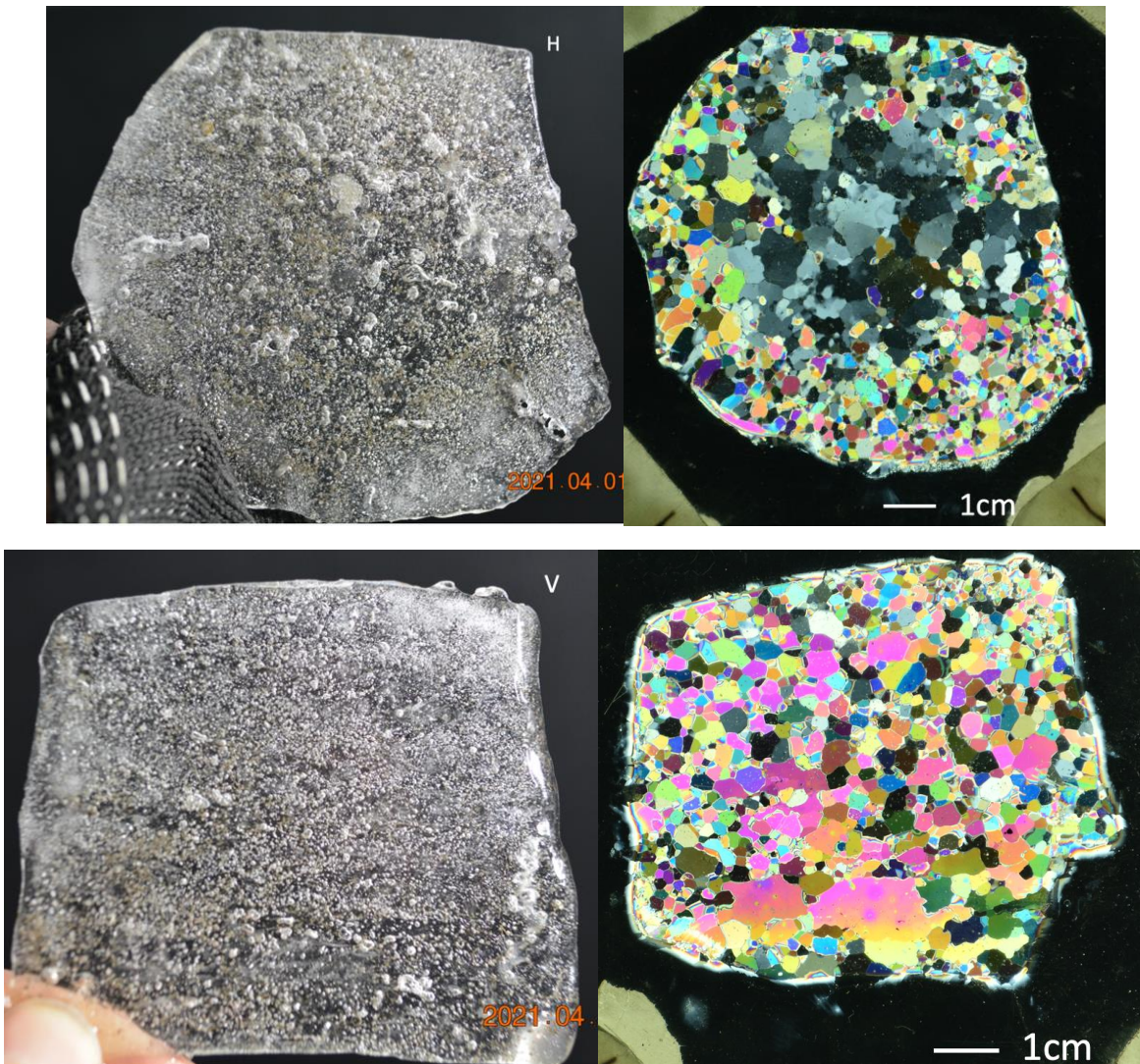


Figure 5 – A) Horizontal thin section of Chap1-75' seen under the natural light and B) polarized light. C) Horizontal thin section of Chap1-73' seen under the natural light and D) polarized light.

1.1.1.4. Ch2-CREEL-73.6'

The massive ice subsample from Ch2-CREEL-73.6' can be seen Figure 6.

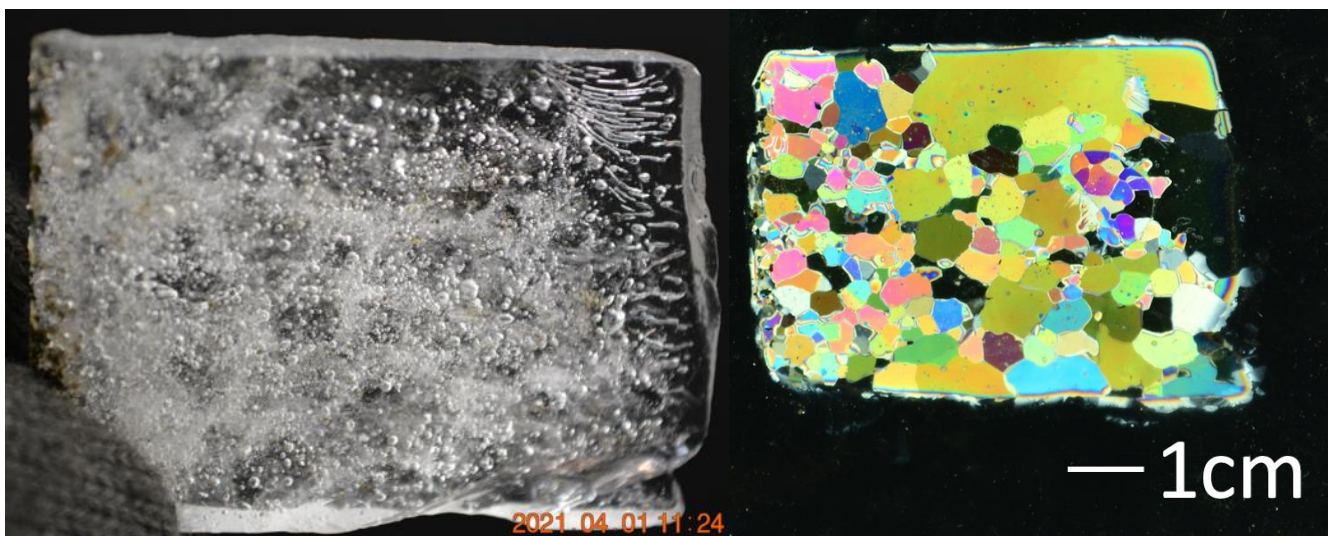
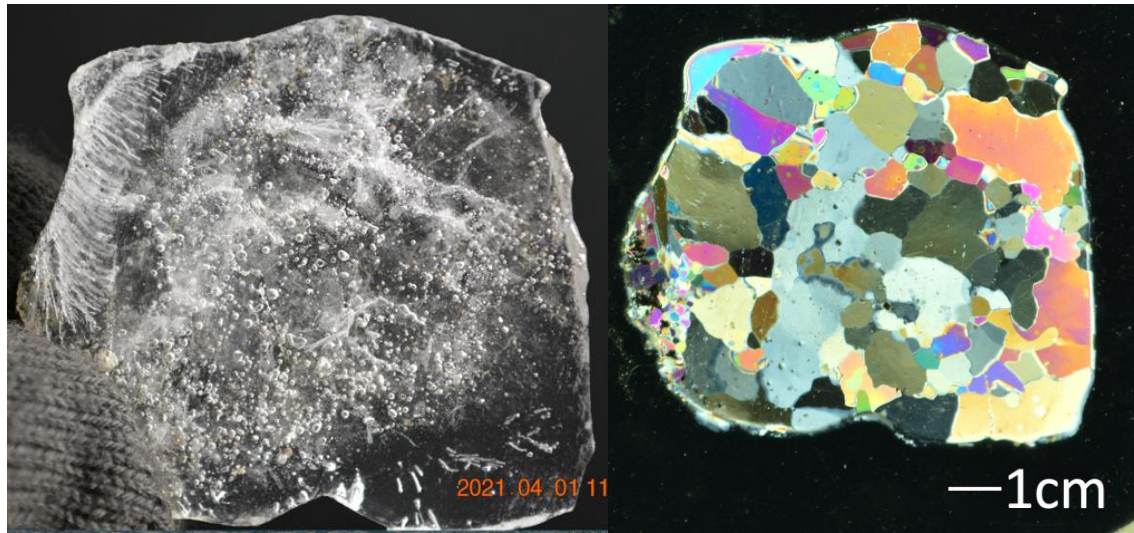


Figure 6 – A) Horizontal thin section of Chap2-73.6' CREEL seen under the natural light and B) polarized light. C) Horizontal thin section of Chap2-73.6' CREEL seen under the natural light and D) polarized light.

1.1.1.5. Ch2-CREEL-75'

The massive ice subsample from Ch2-CREEL-75 can be seen Figure 7.

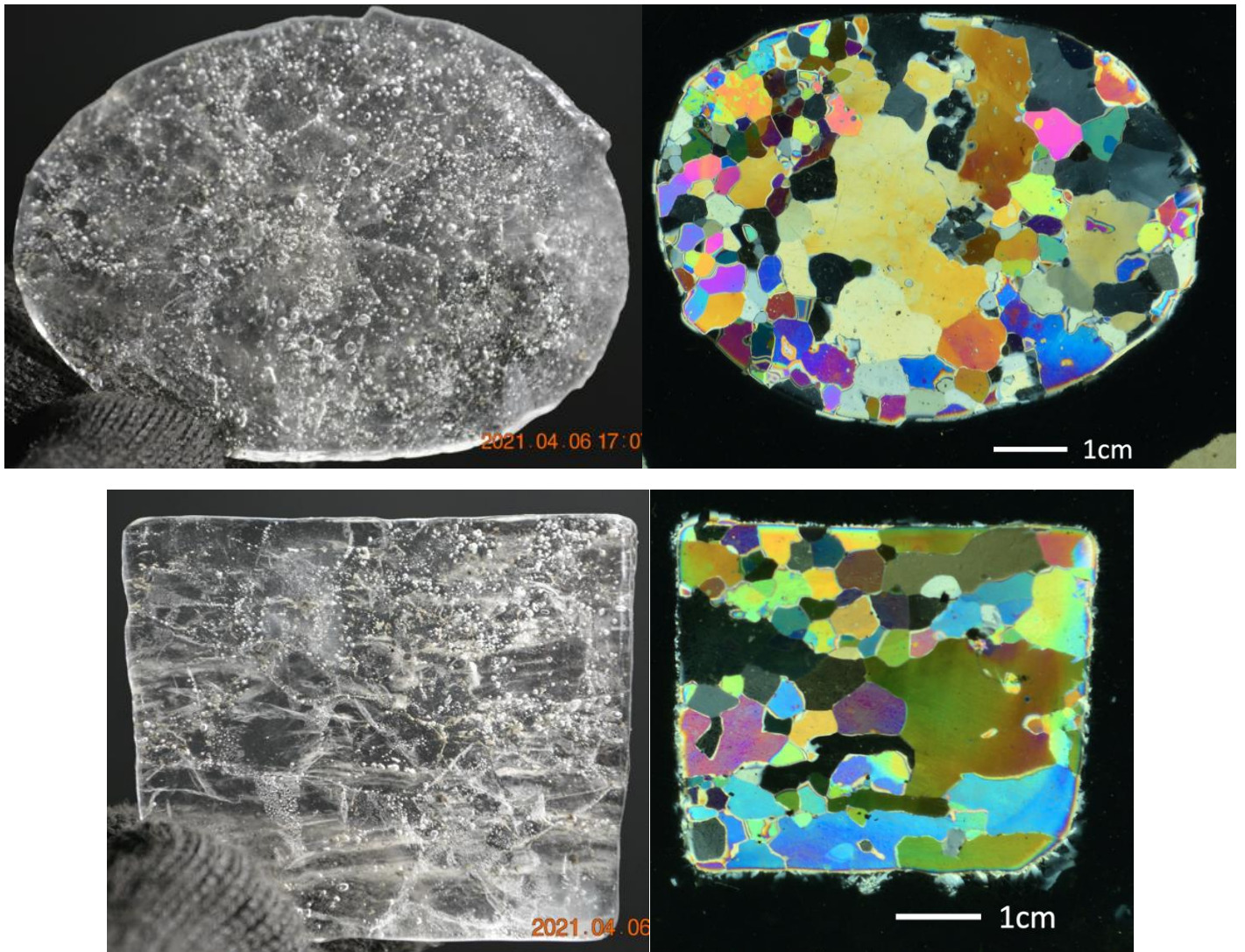


Figure 7 – A) Horizontal thin section of Chap2-75' CREEL seen under the natural light and B) polarized light. C) Horizontal thin section of Chap2-75' CREEL seen under the natural light and D) polarized light.

1.1.1.6. Ch2-CREEL-76.6'

The massive ice subsample from Ch2-CREEL-76.6' can be seen Figure 8. The sample is bubble-rich, with irregular small bubbles that are clear to pale brown. The crystals are medium in size and vary in color. The sample may be refrozen on the edge of an ice sheet.

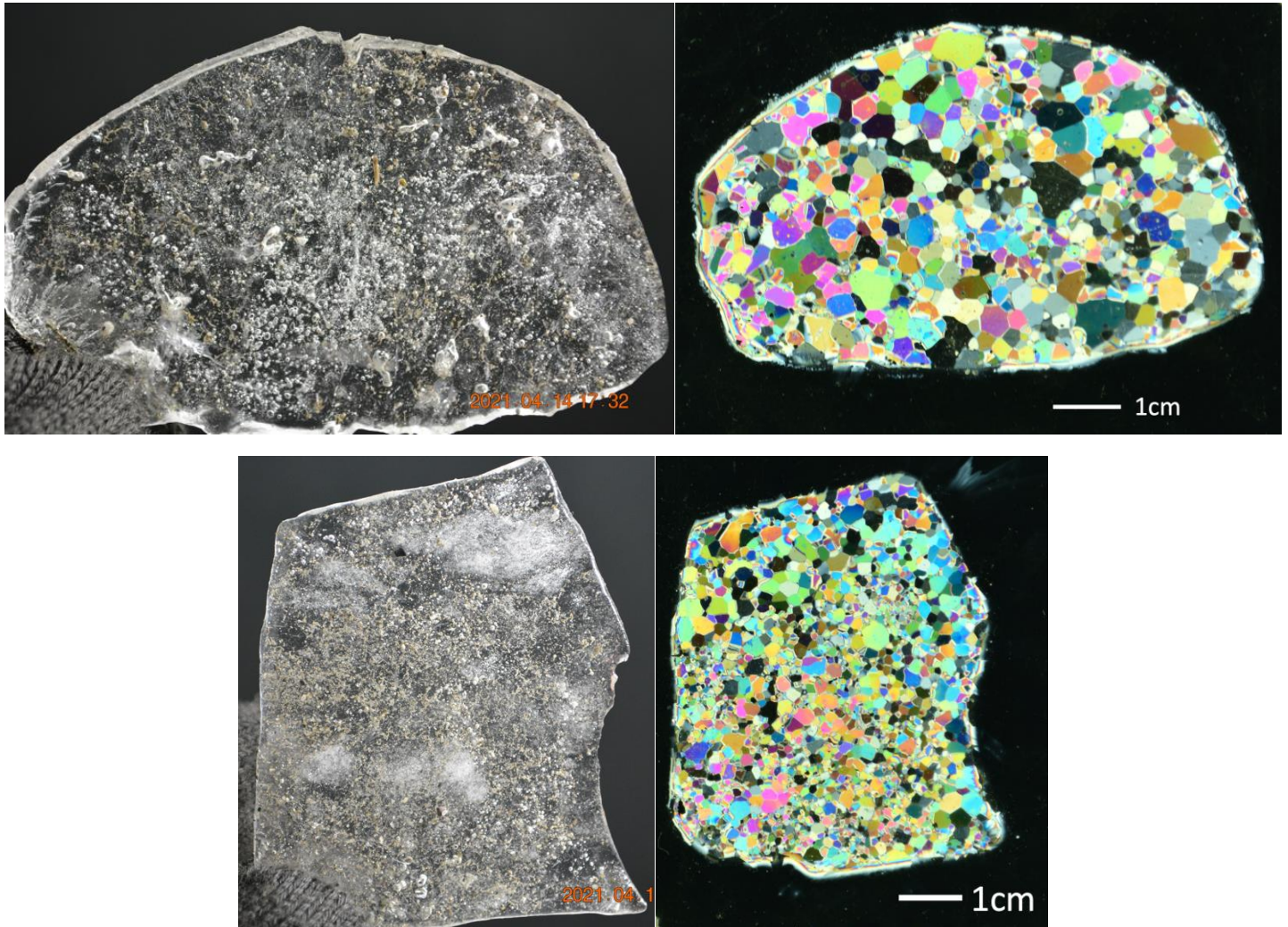


Figure 8 – A) Horizontal thin section of Chap2-76.6' CREEL seen under the natural light and B) polarized light. C) Horizontal thin section of Chap2-76.6' CREEL seen under the natural light and D) polarized light.

Section 3.2.1 Appendix E: Isotopic Analysis

Michel Sliger and Daniel Fortier

January 2022

Edited by : Frances Amyot

1. Introduction

The classes of water samples for the analysis of the stable isotopes were determined according to their nature:

- a- the active layer (generally speaking) [al]
- b- the active layer at higher points (headwater) [head]
- c- the lakes [lake]
- d- the ice lenses of the shallow boreholes (S-BH-2/7) [lens]
- e- the massive ice from the deep borehole (D-BH-5) [massive]
- f- the rain at the camp [rain]
- g- the river [river]
- h- puddles from the roadsides [road]
- i- seepage areas in the eroding cliff [seep]
- j- the snow [snow]
- k- the ice wedges of the shallow boreholes (S-BH-2/7) [wedge]
- l- the active layer in water tracks [wt]

1.1. Meteoric water line and variation of the isotopic signature across classes

According to Craig (1961), Clark and Lauriol (1997) Kendall et al. (2014) and Baranova (2017), the Meteoritic water line represents the stable relation between O18 and D2 of meteoritic waters that have not undergone significant evaporation. We expect the lakes of the region to be affected by a strong evaporation process and they should be excluded of the MWL. We also ruled the soil, subsurface and groundwater, and ground-ice out of the trend line because of all the processes that can modify its isotopic signature (i.e. soil processes and freezing). However, due to the lack of rain samples to get an average value, we included the water from the river, which is considered a mixture reflecting the water from all the reservoirs, but dominated by rain, and surface and shallow soil water in the summer.

Note that the local trend line is nothing more than a constructed tool helping to compare other values. In order to get a good grasp on various soil and groundwater types, segregating it from mostly meteoritic waters looked like the best compromise possible.

The trend line that intercepts all our snow, river and rain samples is $7.1492x-13.403$. It is considerably less steep than the global one (8x) but similar to what was reported by Lacelle et al. (2009) at Inuvik and by Baranova (2017) at Ogilvie River crossing. They both show a slope of 7.3x. A bit offset, Lacelle et al. reported a slope of about 6.3x at Mayo in the paper where they analysed the isotopic signature of the glacier ice found near Chapman Lake (Lacelle et al., 2007); data were from the Global Network of Isotopes in Precipitation (GNIP) (<https://www.iaea.org/services/networks/gnip>).

The local meteoric water line based on the data we found will be used to analyse how the various ground waters differ from fresh waters, as seen in Figure 1.

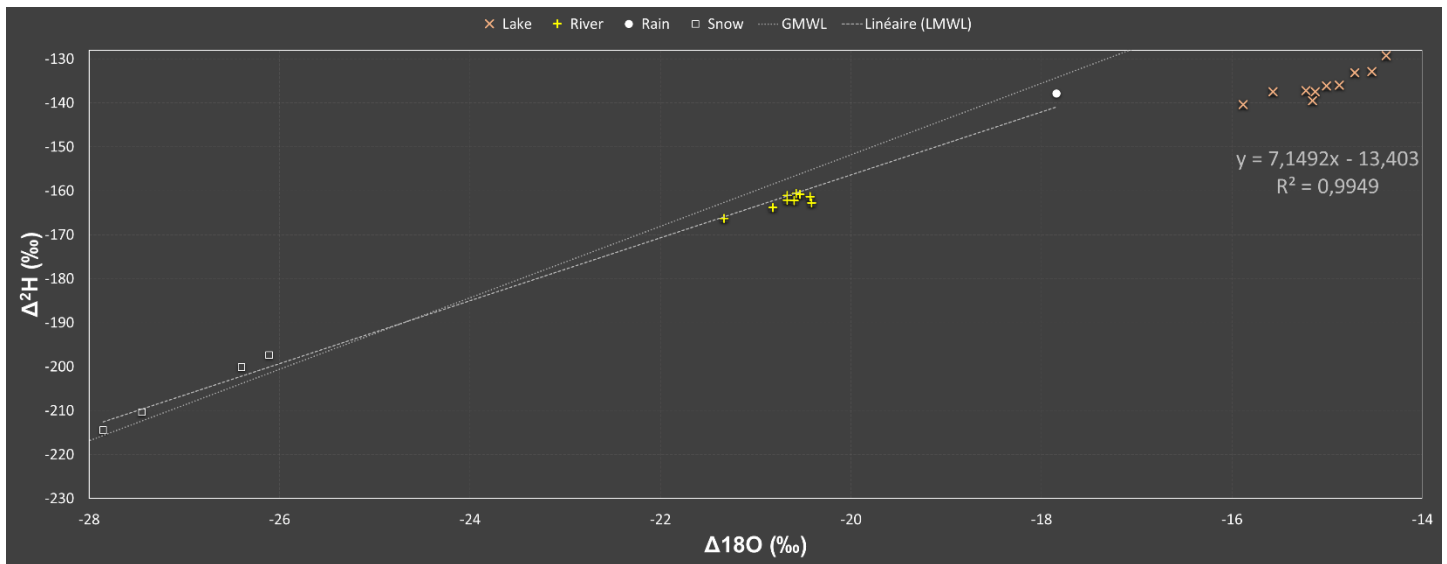


Figure 1 – Global and local meteoritic water lines (GMWL and LMWL) computed from the isotopic signature of the snow, river and rainwater. Lake samples are displayed for information but unused for computing the trend line

The strong evaporation component in the water budget has the effect of enriching the water in stable isotopes (less-negative values); also, the increase of $\Delta\text{O}2$ is favored compared to that of ΔD , as seen in Figure 2. Figure 3 shows box plots that represent the variation of O18 D2 and the relative concentration of D2 from the LMWL model.

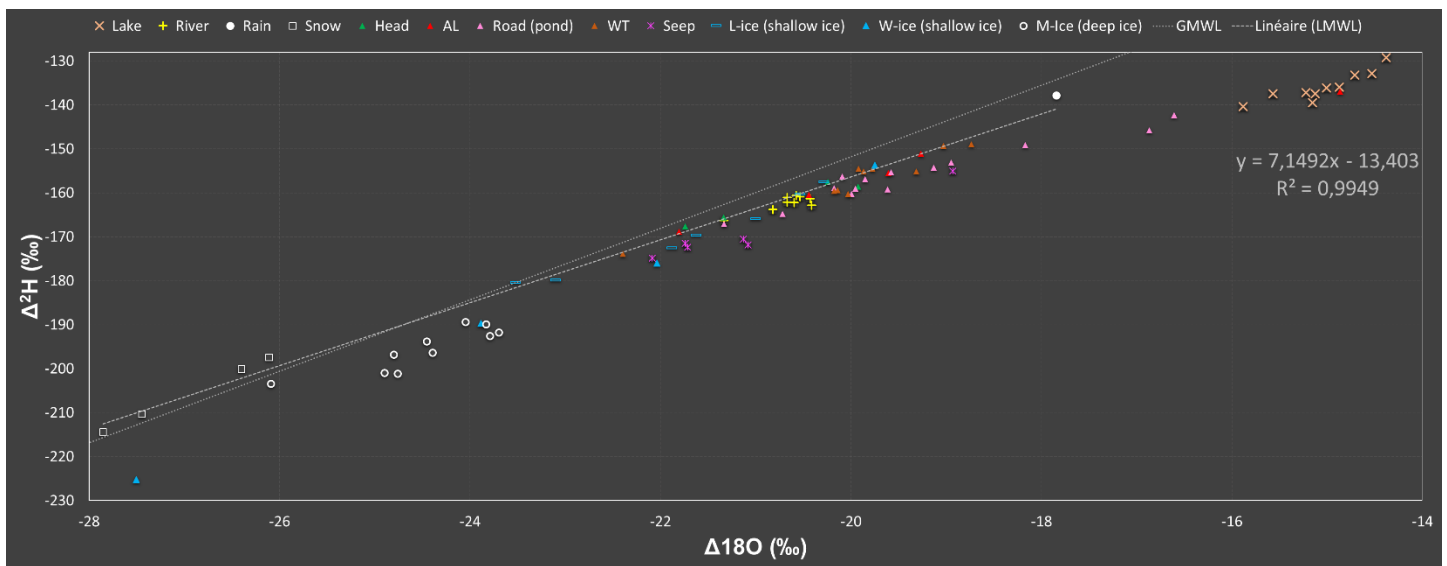


Figure 2 – Isotopic signature of every ice and water sample from the 2019 field campaign at the research site plot over the GMWL and the LMWL. Note the extreme values of the lake samples.

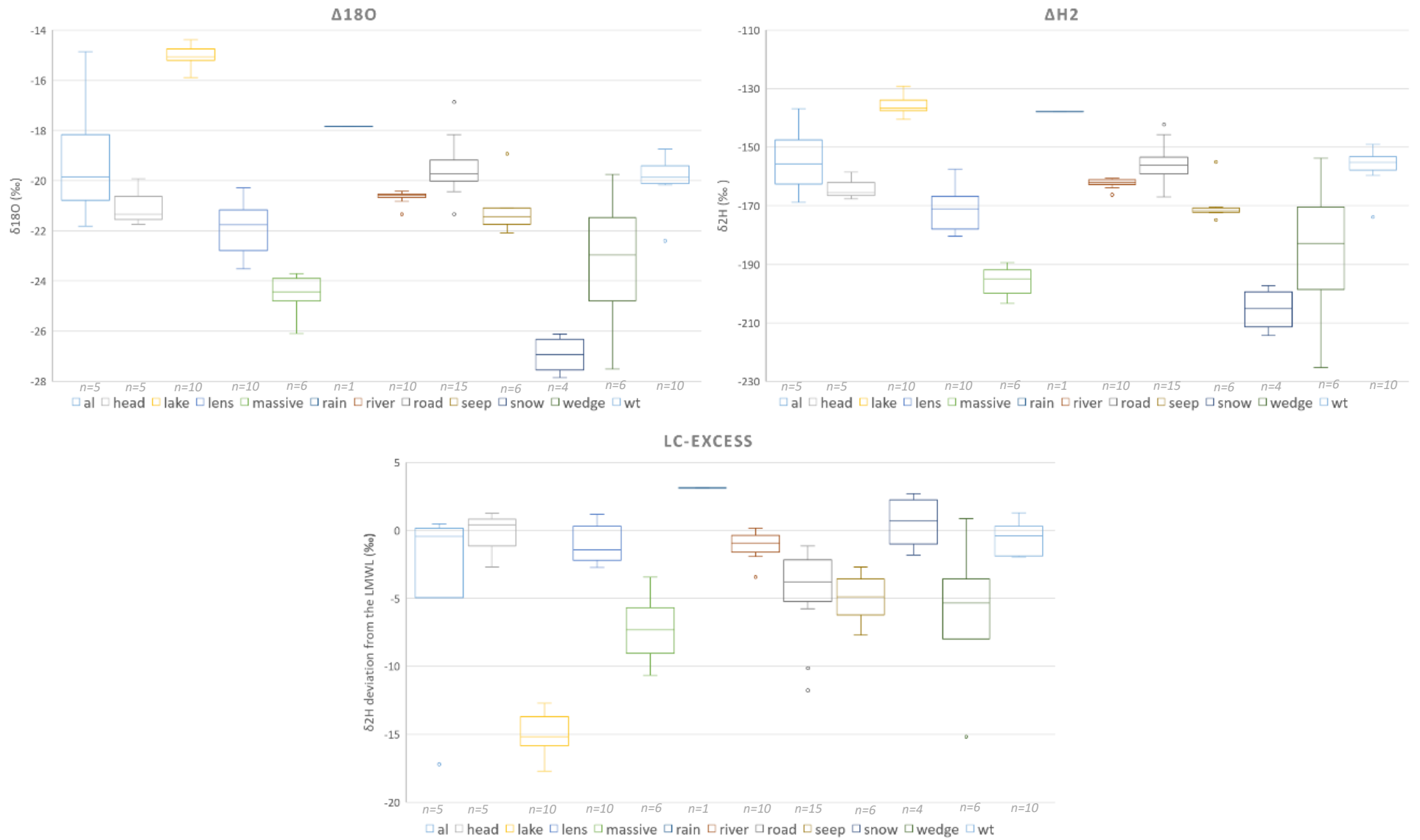


Figure 3 – Box plots representing the variation of A) δO^{18} , B) δH^2 and C) the deviation of relative δH^2 concentration regarding the LMWL model (LC-Excess)

1.2. Isotopes of the ground ice

Figure 4 shows that the ice lenses follow the trend line quite well, while the ice wedges follow a linear progression that is steeper than would cross the trend line just below the isotopic value of the rain. Note the extremely wide range of isotopic signature of the ice wedges; the lowest value is well lower than the massive ice found in the deep borehole. This one is clearly depleted in ΔD compared to what it should be regarding the LMWL. Also, note the value appearing in the range of massive ice (Figure 5) from the deep borehole, and the fact that this massive ice intersects the trend line of isotopic signature of ice wedges from shallow boreholes. Finally, the trend of massive ice (from surface ice-wedge and deep boreholes) leads directly to the value measured for the sample of rain gathered.

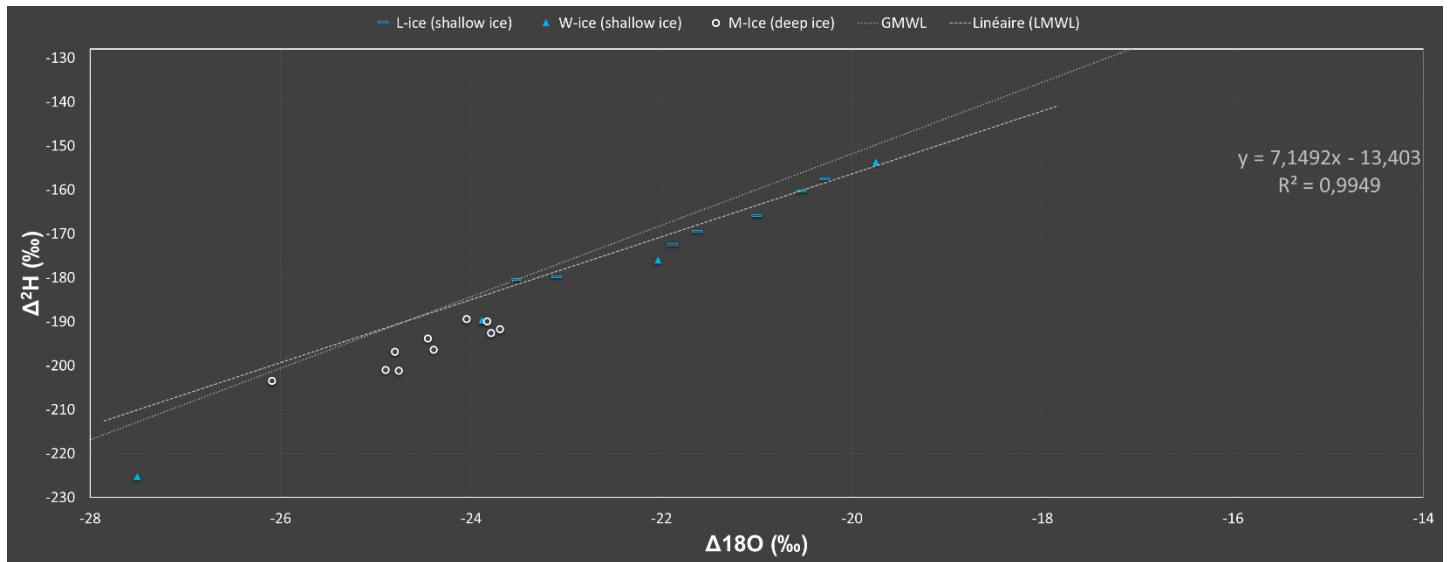


Figure 4 – Isotopic signature of the ice from lenses and wedges in the shallow boreholes (L-ice and W-ice respectively in the legend) and massive buried ice from the deep boreholes (M-ice in the legend), over the GMWL and the LMWL

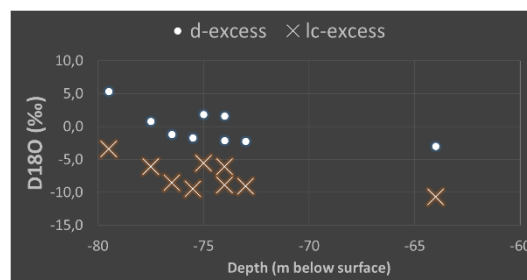


Figure 5 – Deviation of the massive ice's dO^{18} from the GMWL (d-excess) and from the LMWL (lc-excess) along the depth

1.3. Isotopes of the soil water

All the soil water shows similar trends to the LMWL with one exception (Figure 6). This exception shows the same isotopic signature as lake samples (far right on the graphic). It has been sampled from the trough of the polygon field where it is possible that the water has been standing for some time without any movement downslope due to a significant micro topography. Regarding the isotopic values, all the water samples from the active layer could have been grouped without changing the interpretation, but a closer look at where they exactly come from could also be informative.

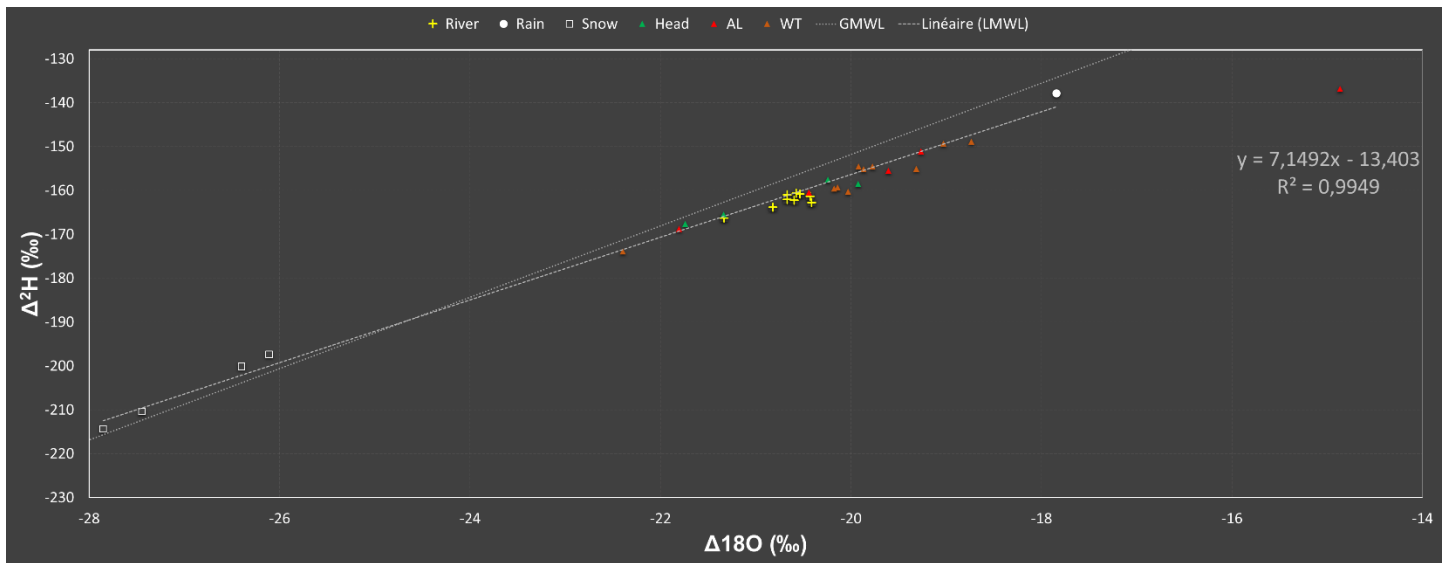


Figure 6 – Isotopic signature of the soil water from the headwater spots, the active layer, and water tracks (respectively head, AL and WT in the legend), over the GMWL, the LMWL, the snow, river and rain isotopic signature

1.4. Isotopes of the roadsides and seepage

The water from the roadside puddle is distinctively enriched in stable isotopes, slightly more so ΔO_2 than ΔD (Figure 7). The water from the puddles appears to follow the same trend of the lakes, suggesting that that it is affected primarily by evaporation. Finally, the water from the seepage clearly deviates from the LMWL and is in the lower range, suggesting older water that is more influenced by the massive ice and/or ice-wedges but not necessarily by the lake. Note that two samples are especially lacking ΔD regarding the LMWL, and one other sample appears in the range of the roadside water. A geographical analysis would provide a deeper look in these irregularities.

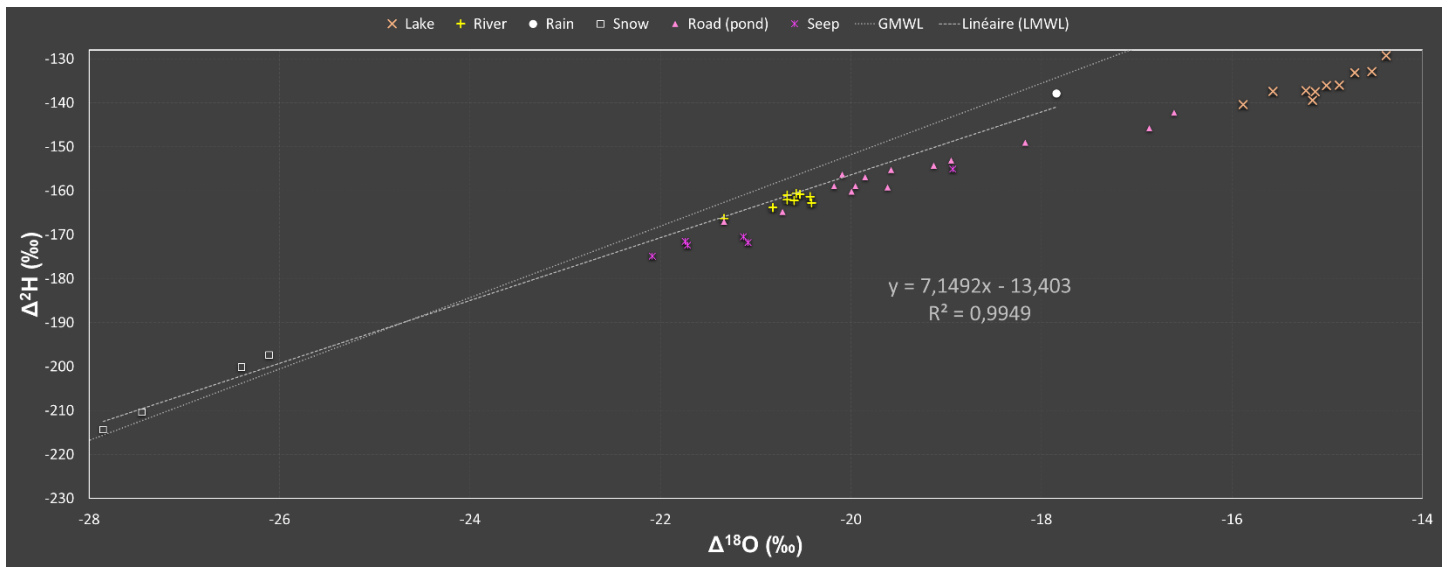


Figure 7 – Isotopic signature of the road-related water from the roadside ponds and the seepages in the riverside cliff (respectively road and seep in the legend), over the GMWL, the LMWL, the snow, river, rain and lake isotopic signature for comparison

2. References

- Baranova, N. (2017). *Evaluating Groundwater In a Permafrost Watershed Using Seasonal Geochemical and Isotope Discharge Trends, Ogilvie River, Yukon* (Doctoral dissertation, Université d'Ottawa/University of Ottawa).
- Clark, I. D., & Lauriol, B. (1997). Aufeis of the Firth River basin, northern Yukon, Canada: Insights into permafrost hydrogeology and karst. *Arctic and Alpine Research*, 29(2), 240-252.
- Craig, H. (1961). Isotopic variations in meteoric waters. *Science*, 133(3465), 1702-1703.
- Kendall, C.; Doctor, D.H.; Young, M.B. (2014). Environmental isotope applications in hydrologic studies. *Treatise on Geochemistry, Second Edition*. Eds. H.D. Holland and K.K. Turekian. Volume 7, p. 273-327. 7.9 - Environmental Isotope Applications in Hydrologic Studies.
- Lacelle, D., Lauriol, B., Clark, I. D., Cardyn, R., & Zdanowicz, C. (2007). Nature and origin of a Pleistocene-age massive ground-ice body exposed in the Chapman Lake moraine complex, central Yukon Territory, Canada. *Quaternary Research*, 68(2), 249-260.
- Lacelle, D., Fontaine, M., Forest, A. P., & Kokelj, S. (2014). High-resolution stable water isotopes as tracers of thaw unconformities in permafrost: A case study from western Arctic Canada. *Chemical Geology*, 368, 85-96.

Section 3.2.1 Appendix F: Hydro-geochemical analysis

Michel Sliger and Daniel Fortier

January 2022

Edited by: Frances Amyot

1. Geochemical analysis methods

For the analysis of the geochemistry, the water and sediment samples have been classified according to their nature, and the sampling operation had to respect this classification. The water samples are from:

- the active layer (generally speaking) [al], n=4
- the active layer at higher points (headwater) [head], n=5
- the lakes [lake], n=10
- the ice lenses of the shallow boreholes (S-BH-2/7) [lens], n=6
- the massive ice from the deep borehole (D-BH-5) [massive], n=10
- the rain at the camp [rain], n=1
- the river [river], n=10
- puddles from the roadsides [road], n=15
- seepage areas in the eroding cliff [seep], n=6
- the snow [snow], n=4
- the ice wedges of the shallow boreholes (S-BH-2/7) [wedge], n=6
- the active layer in water tracks [wt], n=10

The deionized water from the laboratories (Yukon University and Université de Montréal) also have been tested

- Deionized laboratory water [di], n=5

The measures of soil diluted in water are from:

- the cliffside [cliff], n=4
- subsamples of the active layer related to shallow boreholes [al-s], n=23
- subsamples of the sediments from the shallow boreholes (S-BH-1/7) [s-bh], n=30
- subsamples of the sediments from the deep borehole (D-BH-5) [d-bh], n=6*

Box plots in Figures 1-7 below show variation in the water and soil samples of lithium, sodium, potassium, magnesium, calcium, ammonia and conductivity, respectively. Note that the order of the samples is different in all the graphs, but the four soil samples are always on the right of the graphs.

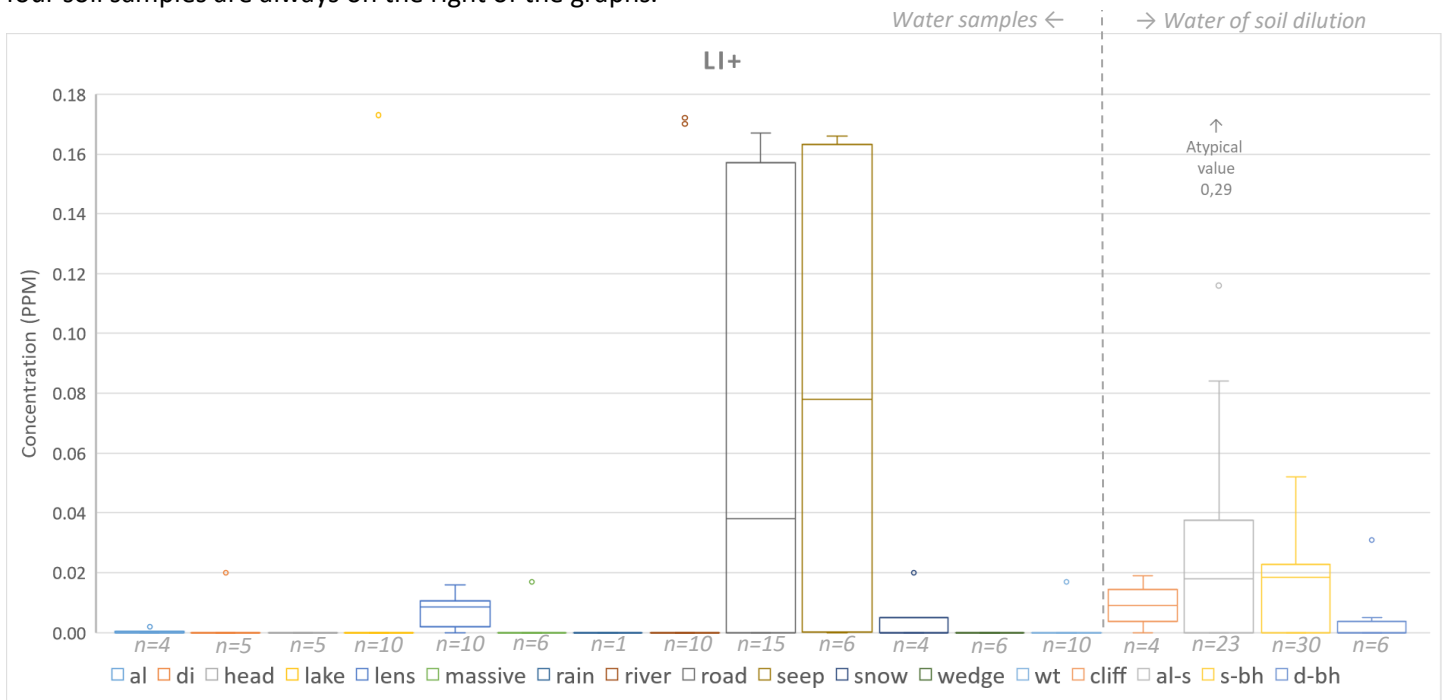


Figure 1 – Box plot representing the variation of the lithium across water samples and the dilution water of soil samples

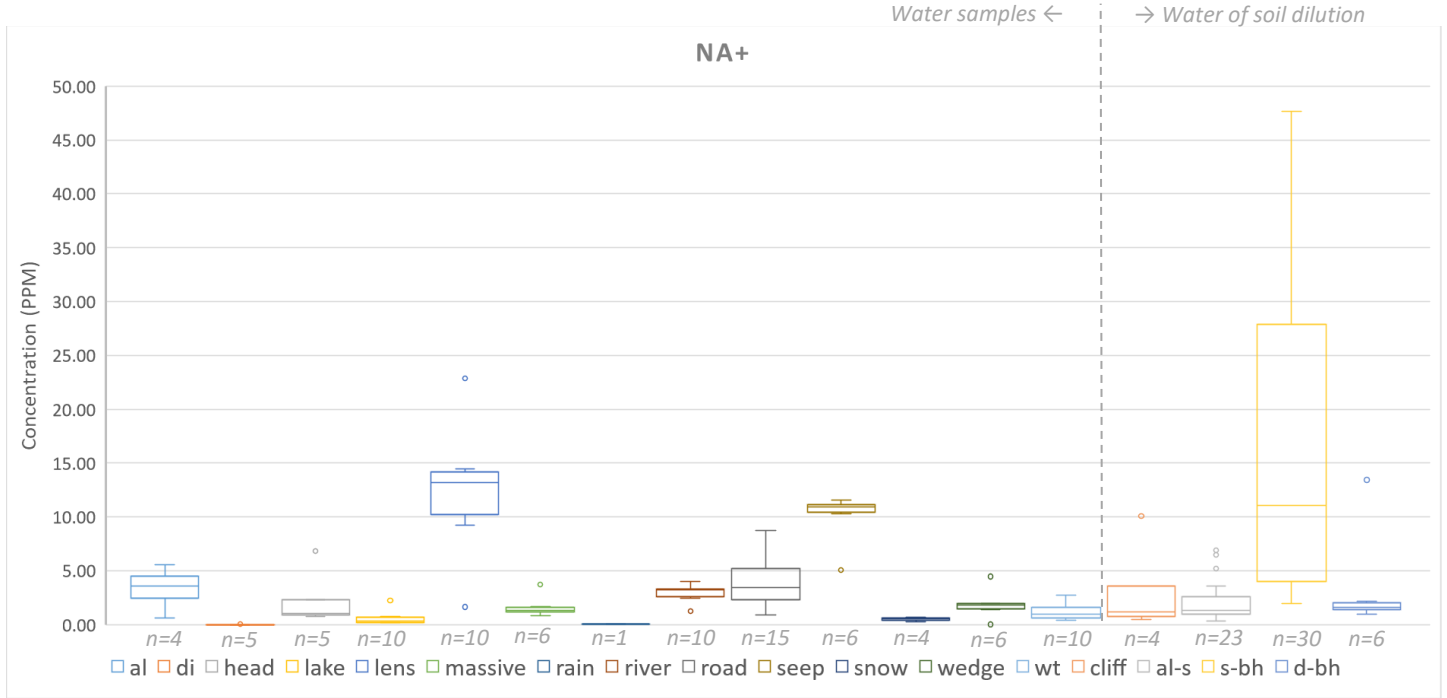


Figure 2 – Box plot representing the variation of the sodium across water samples and the dilution water of soil samples

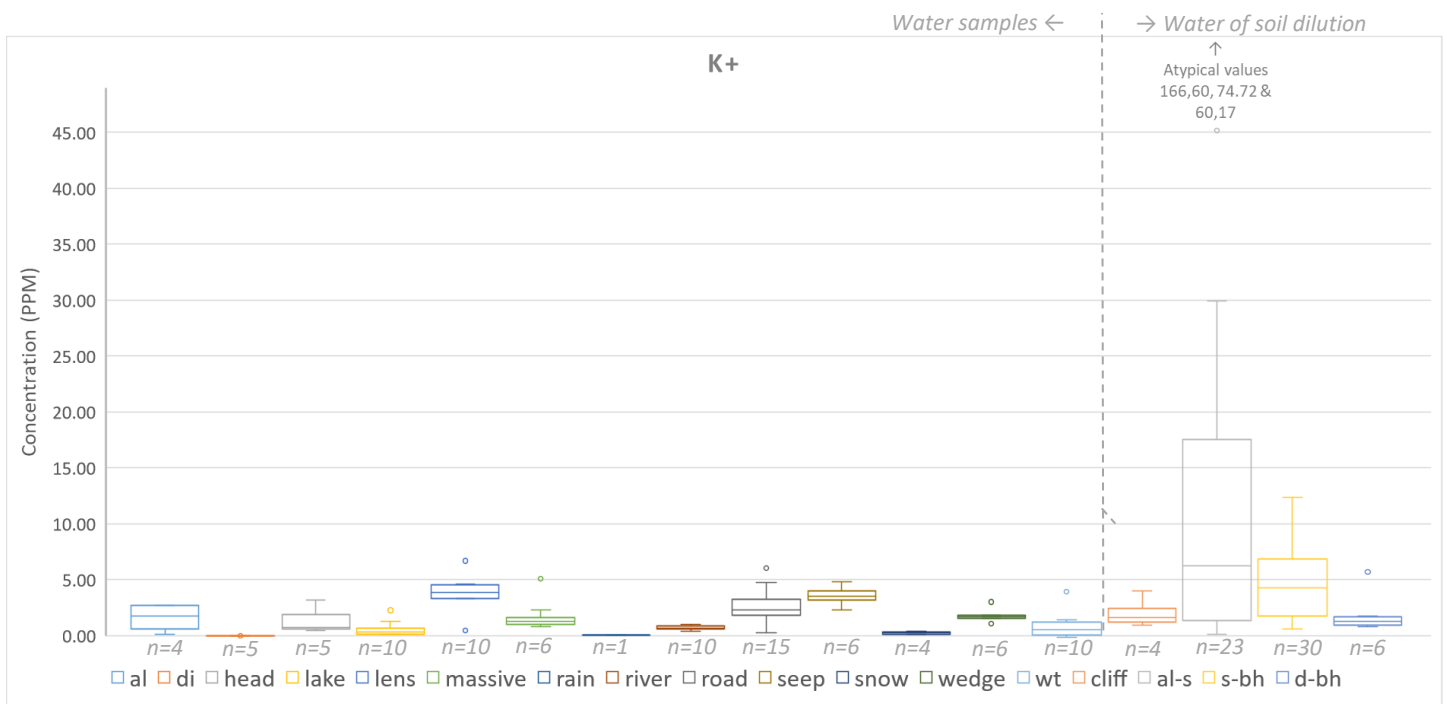


Figure 3 – Box plot representing the variation of the potassium across water samples and the dilution water of soil samples

Water samples ← → Water of soil dilution

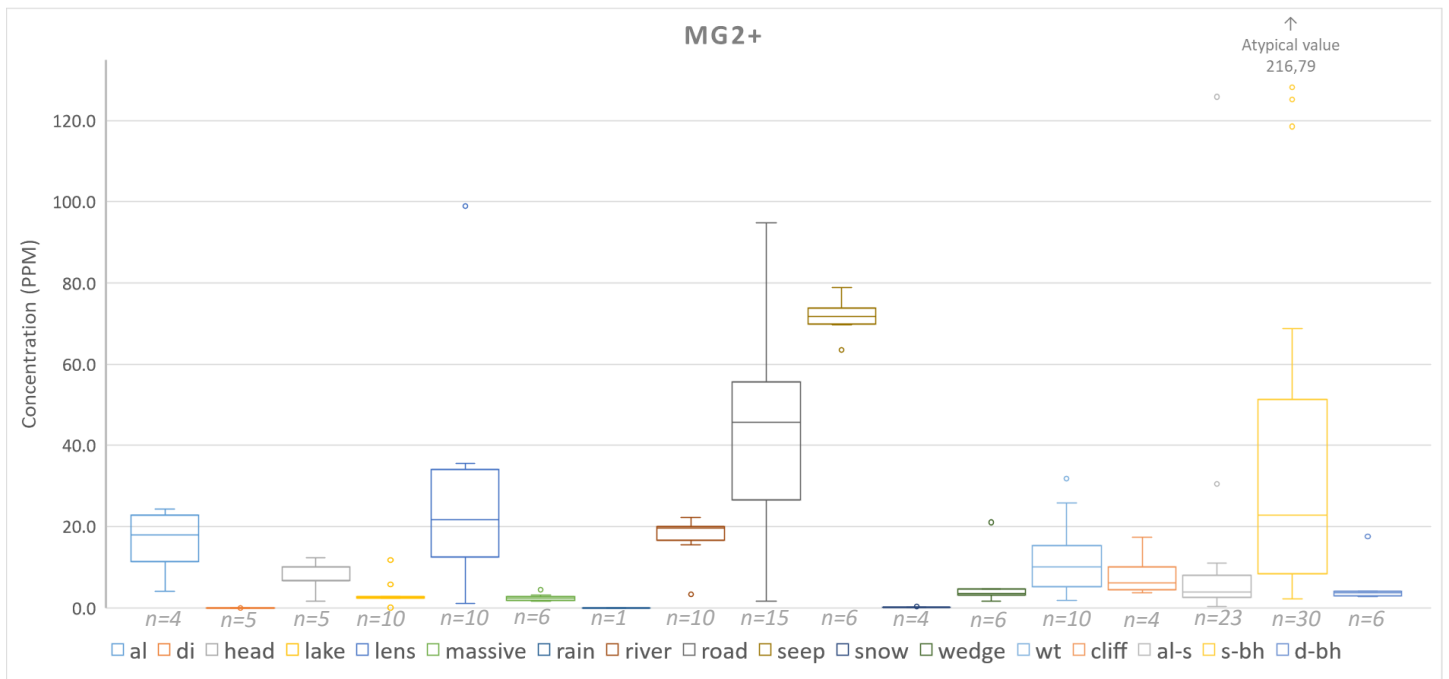


Figure 4 – Box plot representing the variation of the magnesium across water samples and the dilution water of soil samples

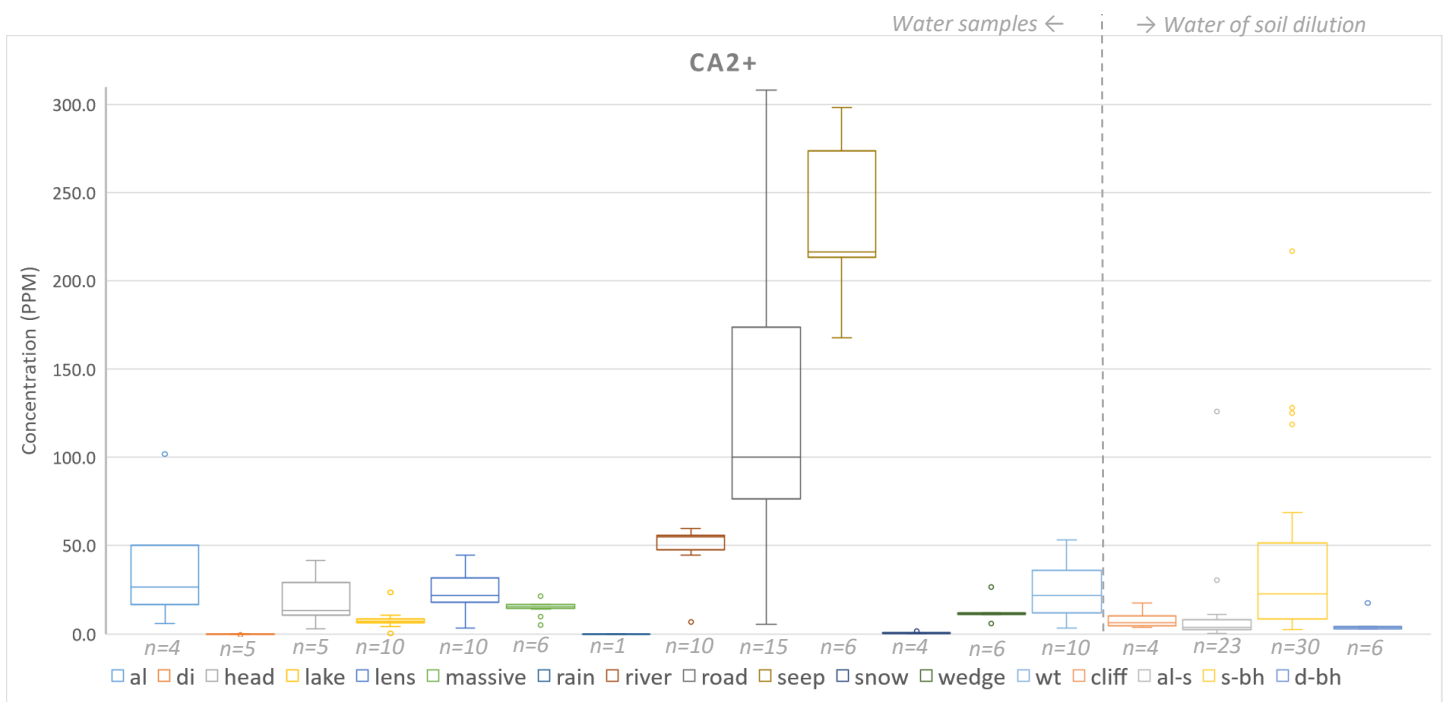


Figure 5 – Box plot representing the variation of the calcium across water samples and the dilution water of soil samples

Water samples ← → Water of soil dilution

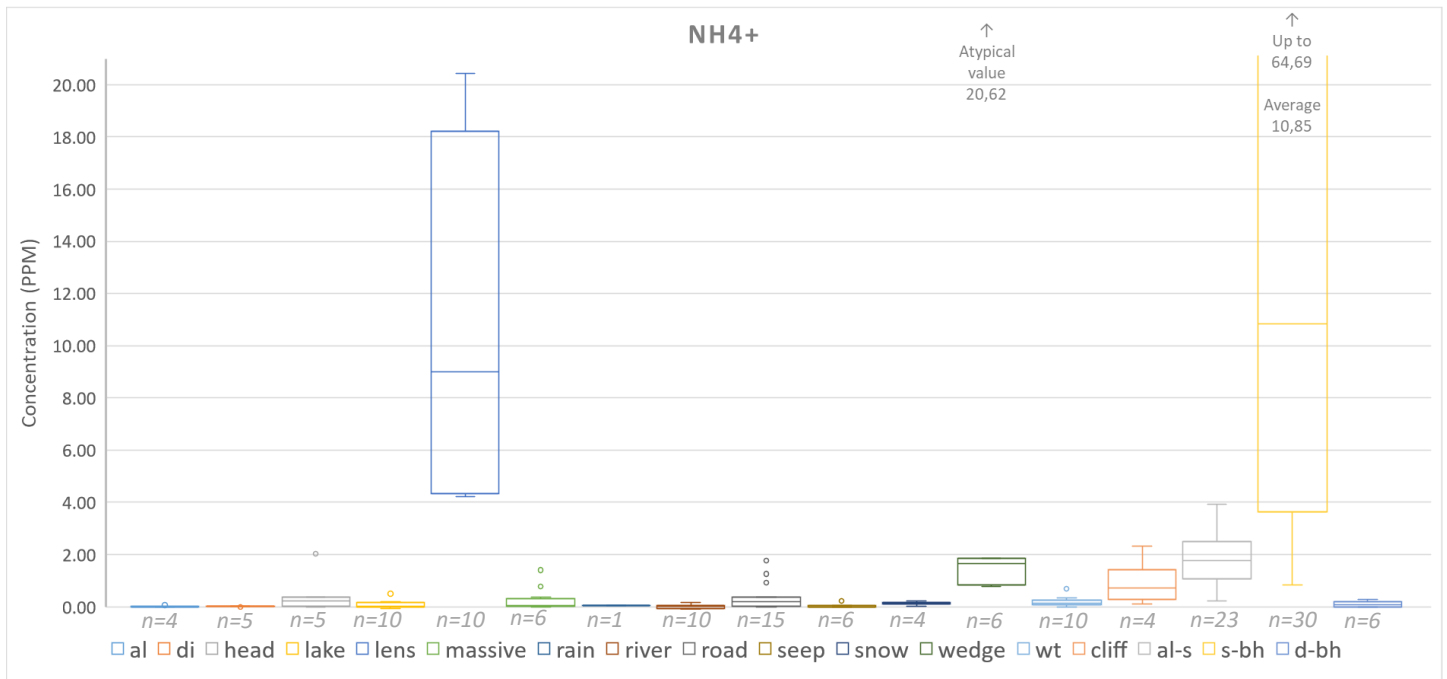


Figure 6 – Box plot representing the variation of the ammonia across water samples and the dilution water of soil samples

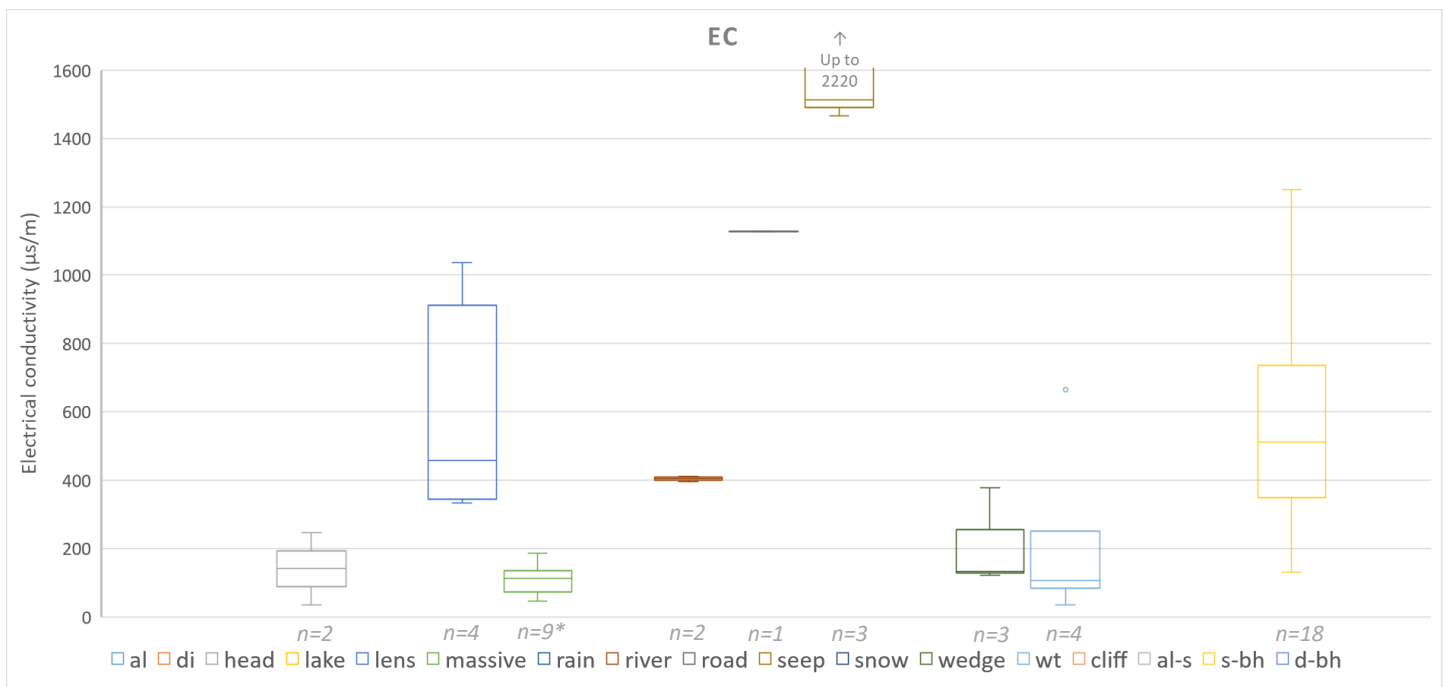


Figure 7 – Box plot representing the variation of the electric conductivity across water samples and the dilution water of soil samples. * Unlike for sediments, the values of massive ice relative to the cores drilled by sonic drill are included in the lot because they are similar. The sediments showed extremely higher ionic content when drilled with sonic compared to the ones drilled with CREEL. Sonic were considered unreliable and maybe contaminated.

There were 11 more samples than are presented, but the high values of cation when the sonic drill was used suggests that something occurred during the drilling process. Two possible explanations are that: 1) drilling fluids or surface water was injected and diffused in the sediments' porosity or 2) the vibrating-pushing action smashed the rock and allowed the release of fresh and easily dissolvable material. Local surface water injection is not a preferred hypothesis due to the low ammonia content (NH₄⁺) of the deep borehole sediments [d-bh]. No difference appears between the ice geochemistry drilled by both techniques (sonic and CREELL)

Section 3.2.2 Appendix A:

NTAI Report: Assessment and monitoring of a new retrogressive thaw slump at km 1456 of the Alaska Highway: A rare opportunity

F. Calmels, L.P. Roy, C. Laurent, F. Amyot, J. Cubley, P. Lipovsky

February 2021

Assessment and monitoring of a new retrogressive thaw slump at km 1456 of the Alaska Highway: A rare opportunity

By

Fabrice Calmels

Louis-Philippe Roy

Cyrielle Laurent

Fanny Amyot

Joel Cubley

Panya Lipovsky



Prepared by: Permafrost and Geoscience, YukonU Research Centre, Yukon University

February, 2021

Contents

1. Context of the survey: an introduction	6
1.1. General introduction	6
1.2. Study goals.....	7
2. Study area.....	9
2.1. General site description.....	9
2.2. Climate and vegetation.....	10
2.3. Geology.....	11
2.4. General permafrost and ground conditions.....	12
3. Methods	13
3.1. Geotechnical boreholes.....	13
3.1.1. Boreholes	13
3.1.2. Grain size, ice content and borehole log analysis.....	15
3.1.3. Ground temperature and environmental conditions	17
3.1.4. Inclinator	17
3.1.5. Soil moisture	17
3.2. ERT and EM.....	18
3.2.1. Brief introduction to methodologies and novel use of 3D	18
3.2.2. ERT.....	18
3.2.3. 3D Surveys.....	21
3.3. Geospatial analyses	26
3.3.1. Drone image collection and processing methodology	26
3.3.2. Benchmark survey.....	27
4. Results.....	29
4.1. Geotechnical boreholes.....	29
4.1.1. Grain size, ice content and borehole log analysis.....	29
4.1.2. Ground temperature and environmental conditions	31
4.1.3. Soil moisture	35
4.1.4. Inclinator	35
4.2. ERT and EM.....	41
4.2.1. ERT.....	41

4.2.2.	3D ERT & EM	44
4.3.	Geospatial analyses	48
4.3.1.	Field and UAV observation.....	48
4.3.2.	Benchmark survey.....	51
5.	Synthesis of results	51
5.1.	General permafrost characteristics and history.....	51
5.2.	Retrogressive thaw slump processes	54
6.	References	57

1. Context of the survey: an introduction

1.1. General introduction

Retrogressive thaw slumps (RTS) are a form of slope failure resulting in a mass-wasting landform. This category of landslide results from the thawing of ice-rich permafrost, i.e., permafrost containing a significant amount of excess ice. RTSs usually begin when ice-rich permafrost is exposed because of erosion, mass movement, forest fires, construction, or mining. A steep headwall develops; where ground ice is visible and unprotected, then retreats in a retrogressive manner while the slumping of thawed soil occurs. In more dramatic cases, the RTS is quickly enlarged by the slumping and a steep or vertical headwall develops leaving a low-gradient floor covered by slumped soil, a mixture of thawed sediment and meltwater that slides down the face of the headwall and flows as it retreats.

Retrogressive thaw slumps are common in ice-rich glaciolacustrine sediments and fine grained diamictons. Such is the case for an active RTS that was found adjacent to the Alaska Highway at km 1456 in April 2019 during a field study led in partnership with the Yukon Geological Survey (YGS) aiming to provide permafrost characterization, monitoring, and climate change analysis in the greater Whitehorse area. The slump developed on a hillslope along the shoreline of the Takhini River. In the area, permafrost is discontinuous and found in sporadic isolated patches that can be significantly ice-rich and thaw-sensitive. This RTS is located 200 m west of another RTS that was initiated prior to 1979 and was partially stabilized by 2004. Between these two features stands a wooded area showing signs of slope instability (collapsed trees, cracking) where a third RTS may soon develop (Figure 1).

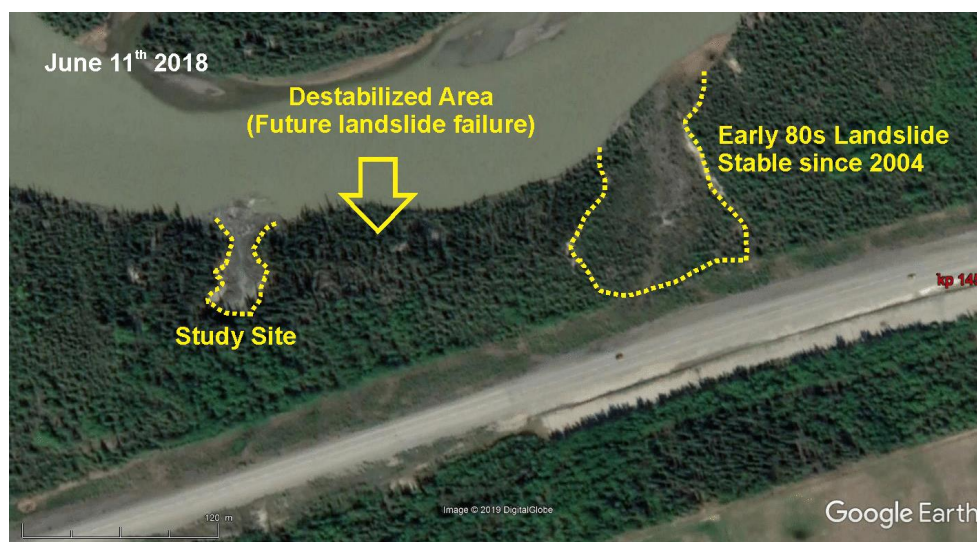


Figure 1. Study area at Km 1456 on the Alaska Highway



Figure 2. A) View of the RTS; B) Headwall of the RTS exposing ice-rich permafrost; C- 10 cm thick ground ice lenses

This is an alarming situation, but also one that presents an opportunity for climate change adaptation research, as well as outreach and engagement with Yukon transportation professionals, and Yukon University students. The RTS has been active for six or seven years (initiated in 2013 or 2014) based on an analysis of Google Earth satellite and aerial imagery. According to aerial imagery, the 1979 RTS remained active for 25 years, suggesting that this RTS will likely continue expanding during the next several summers, with the potential risk of it eventually impacting the road.

1.2. Study goals

The purpose of this study was to act before any serious damage occurs and seize the opportunity of the site being located near the city center to develop an intensive research program at a low cost. The objective was to develop an innovative research program around this RTS site that will:

- Develop a better understanding of retrogressive thaw slumps that impact road corridors in the North;
- Develop and test a multi-technical monitoring approach using complementary instrumentation for RTSs that will eventually be used for the development of geohazard alarm systems;
- Inform an approach to mitigate the threat caused by RTSs on road corridors.
- Engage Yukon transportation professionals and Yukon University students in order to advance their understanding of the threats posed by RTSs; their lessons learned can then be applied to RTSs in more remote locations.

To reach this objective, several research activities were carried out on site, including:

- Drilling of sampled boreholes, from RTS to the right of way, instrumented with ground temperature cables, soil moisture sensors, and inclinometer arrays to monitor ground parameters and RTS failure in real-time;
- Monitoring ground surface movement with differential GPS (DGPS) measurement tying in with benchmarks and existing legal survey pins and establishing surface survey monuments;
- Imaging and topography monitoring using UAV (drone) photogrammetry;
- Two-dimensional Electrical Resistivity Tomography (ERT) surveying;
- Testing a new geophysical approach using 3D ERT and 3D Electromagnetic (EM) surveys to map permafrost properties and ground water movements;
- Mapping and monitoring of the propagation of tension cracks, and other ground movement markers as precursory indicators of failure.

The study addresses key knowledge gaps in mapping of RTS formation and evolution processes, as well as methodological gaps in the monitoring of such geohazards. To develop understandings of RTS processes, the survey focuses on 4 parameters:

- Frozen soil properties (through borehole data such as grain-size distribution, excess ice content, etc., geophysics - ERT): which provides geotechnical information such as thaw sensitivity and potential consolidation;
- Ground thermal regime (borehole monitoring): which provides information such as ground temperature, active layer thickness, thaw rates, indications of water movement;
- Ground water dynamics (borehole monitoring/humidity sensor): which provides links between ground moisture, environmental conditions, and the timing and rate of the failure;
- Ground movements (below ground surface using inclinometers in boreholes; above ground surface including DGPS monitoring, UAV surveys, mapping of ground movement indicators): which provides information on the rate of deformation as well as its spatial distribution in three-dimensions.

The project monitored these parameters in real-time through the implementation of an array of sensors located in two boreholes instrumented with ground temperature cables, moisture sensors, and inclinometer arrays. One 20-25m borehole was drilled in the right of way (ROW), about 50 m from the location of the RTS headwall at the time of the drilling, to monitor failure indicators at a distance from the RTS during multi-year monitoring. The intention is to provide long term monitoring for signs of instability at depth. This monitoring station could be upgraded with warning and alarm systems in the future as part of a safety plan for monitoring the instability as it progresses towards the highway. A second, 6 m borehole was located close to the RTS (5-6 m from the headwall) to monitor the parameters during RTS failures. This borehole was checked regularly to recover the instrumentation when the RTS headwall retreated to the location of the borehole. Another 6-m borehole was attempted at an intermediary position, between the ROW borehole and the RTS borehole. However, ground conditions were such that it was not possible to drill deeper than 3 m.

Electro-resistivity tomography (ERT) surveys were conducted to complement borehole observations, characterize ice-rich permafrost thickness, distribution, and boundaries, as well as identify ground water movements. An innovative approach was developed, combining 3-dimensional ERT and Electro-magnetic (EM) surveys.

DGPS monitoring of an array of benchmarks, matched with UAV imagery monitoring provided a complete assessment of ground surface movement that can be integrated with geophysics and borehole data to provide a complete 3D representation of the RTS development, integrated in a geo-database.

This project provides information that will be used to model RTS processes, determine the relationships between the variety of measured parameters and the timing/rate of RTS failure. Ultimately, the information will be used to monitor other RTSs that impact transportation systems, and to design a system that could anticipate failure and alert highways operators. To the best of our knowledge, this type of multidisciplinary approach has never been used for characterizing and monitoring RTS formation processes.

2. Study area

2.1. General site description

The Takhini River retrogressive thaw slump site is located at kilometer 1456 of the Alaska Highway, approximately 30 km west of Whitehorse (Figure 3). The site is situated in the Takhini valley in the sporadic discontinuous permafrost zone, along the Takhini River. In 2014, a large retrogressive thaw slump developed along the Takhini River bank, and has progressively moved towards the highway. The slump will likely continue to move towards the highway, which could eventually result in the collapse of the highway.

The retrogressive thaw slump was initiated by the erosion on the outer bend of a meander of the river. A tributary creek and alluvial fan enter the Takhini River on the opposite bank, which forces the river further to the outside on this bend. Nine other failures of the same type have occurred within 6 km of this location, including a 40 000 m³ retrogressive thaw slump, only 180 meters east of this site. This last thaw slump was initiated in 1979 by river bank erosion and stayed active until 1986 when the slumping led the headscarp to retreat 112 m to approximately its present position. Since 2004, that thaw slump stabilized a few meters short of the highway. However, cracks in the road surface are continuing to propagate parallel to the landslide headscarp. The active retrogressive thaw slump has been retreating towards the highway at an average rate of 8 meters per year since 2014. Since, several multi-meter long tension cracks have formed between the failure and the road. The closest being 20 meters from the road embankment.

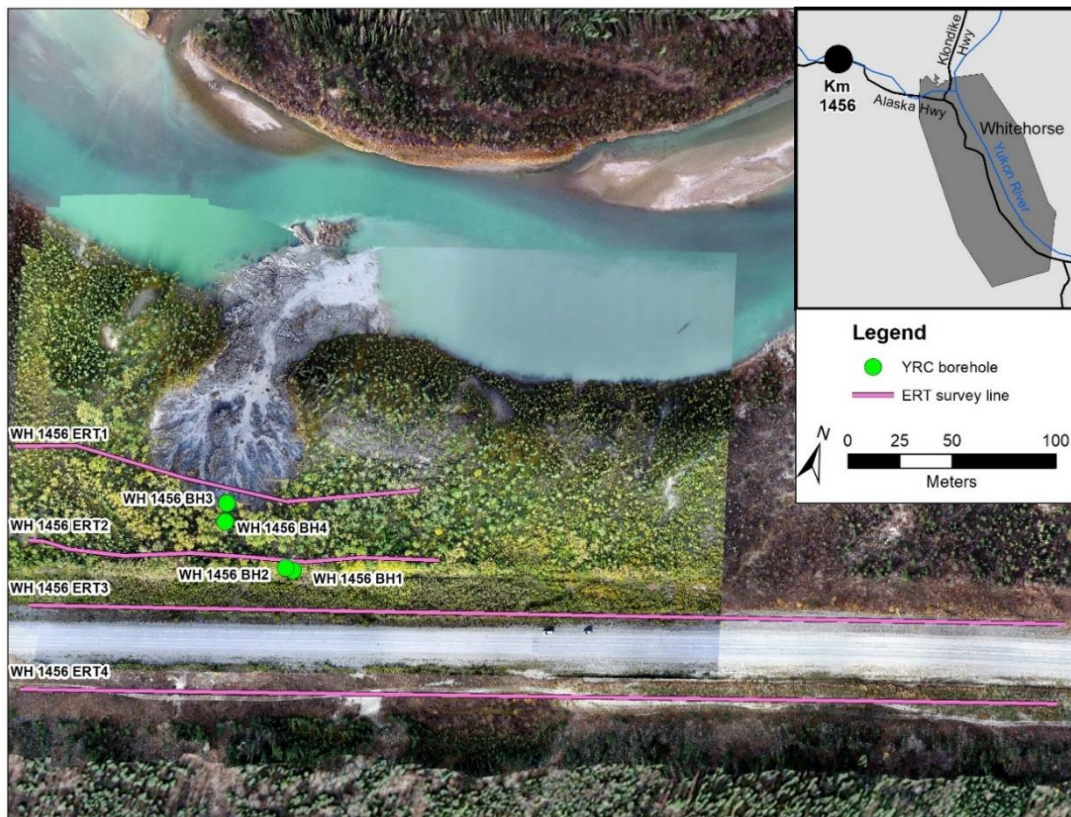


Figure 3. Location of the Alaska Highway km1456 retrogressive thaw slump with borehole and geophysical survey locations

2.2. Climate and vegetation

This section of the Alaska Highway is located in the Southern Lakes Ecoregion. The climate is subarctic with large seasonal variations in temperature and a mean annual air temperature (MAAT) of -3.0°C , which is 2.3°C cooler than the Whitehorse airport (Burn, 1998). This area is also characterized by low precipitation and low humidity due to the rain shadow of the Coast Mountains. The forest is deciduous mixed consisting of lodgepole pine (*Pinus contorta*), white spruce (*Picea glauca*), and aspen (*Populus tremuloides*) (Figure 4). Shrubs such as willow (*Salix spp.*) and soapberry (*Shepherdia canadensis*) are present throughout much of the site. Common plant species are forbs such as fireweed (*Chamaenerion angustifolium*) and alpine sweetvetch (*Hedysarum alpinum*), mosses, and lichens such as *Cladonia spp.*

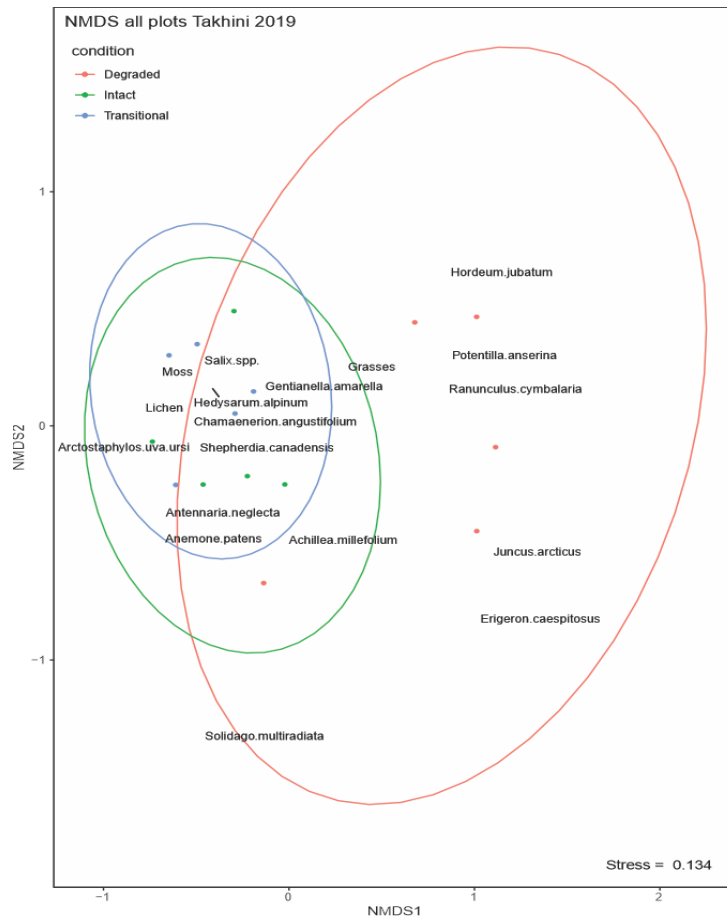


Figure 4. Vegetation plots comparing distribution with ground conditions

2.3. Geology

The entire study area is underlain by the mid-Cretaceous (116 Ma) Whitehorse Pluton which is largely comprised of granodiorite (Yukon Geological Survey, 2019).

The surficial geology and landscape features of the study site are largely a product of the most recent (Late Wisconsinan) McConnell Glaciation, which occurred between 24,000 and 11,000 years ago (Figure 5). Deglaciation of lowland areas began approximately 14,000 years ago. During deglaciation, large volumes of meltwater were dammed in some valleys and formed large glacial lakes. In the Takhini River, Glacial Lake Champagne deposited up to 75 m of silt and clay between 9,000 and 10,000 years ago. Glaciolacustrine silt and clay commonly contain massive ice bodies and are prone to retrogressive thaw slides and thermokarst degradation when disturbed by river erosion, forest fires, or other changes in surface conditions.

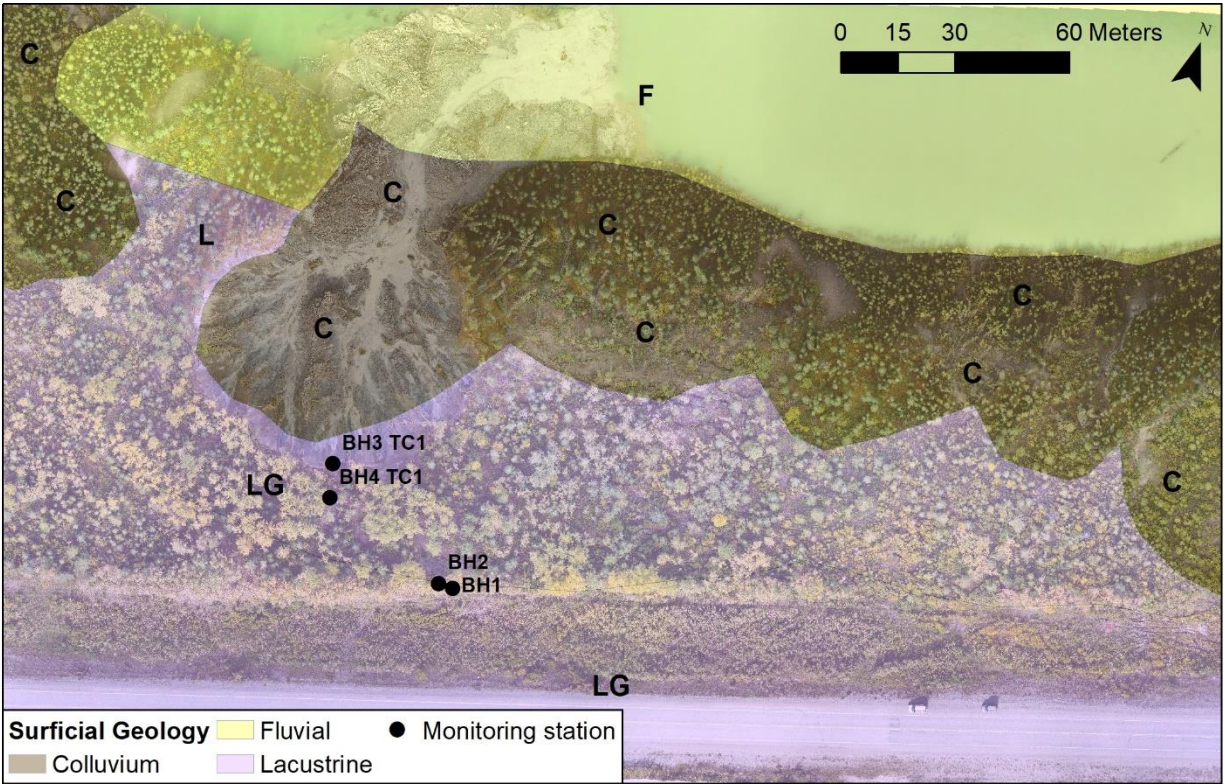


Figure 5. Surficial geology at Takhini retrogressive thaw slump site (YGS, 2021)

2.4. General permafrost and ground conditions

The only signs of permafrost degradation noticeable on site in the forested area are those associated with the development of the retrogressive thaw slump. These include meter wide tension cracks and split trees due ground movements. Along the road in the cleared area, some shallow ponds are present, which probably have thermokarstic origins.

Retrogressive thaw slumps occur when ice-rich permafrost thaws, and generally form on hillslopes. They usually occur along the shorelines of lakes, rivers, and coastlines. Generally, they occur in areas underlain by massive ice bodies, or ice-rich silts. Retrogressive thaw slumps are very similar to landslides in more temperate regions, although they do not have a failure surface. They are typically fast-developing feature but tend to be short-lived: most retrogressive thaw slumps stabilize between 30 and 50 summers after their initiation (French and Egginton, 1973). Retrogressive thaw slumps represent one of the most rapid erosive processes operating in present-day periglacial environments.

3. Methods

3.1. Geotechnical boreholes

3.1.1. Boreholes

A total of four boreholes of various depths were dug at the site, using a variety of methods outlined below. These boreholes were outfitted with multiple sensors, as discussed in sections 3.1.3, 3.1.4, and 3.1.5 below. Table 1 outlines the specifics of the boreholes.

Table 1. Geotechnical boreholes

Site	Date	Coordinates (UTM)	Depth	Sensor Depths
WH_1456_BH1	16/10/2019	8 V 471985 6746876	10 m	No sensors were installed
WH_1456_BH2	23/10/2019	8 V 472000 6746887	25 m	Temperature: AT, 0, 0.5, 1.0, 1.5, 2.0, 3.0, 4.0, 5.0, 6.0, 7.0, 8.0, 9.0, 10.0, 15.0, 20.0 m. Inclinometer: every 50 cm from 0 to 20.0 m
WH_1456_BH3	13/05/2020	8 V 471970 6746905	6 m	Temperature: 0, 0.5, 1.0, 2.0, 3.0, 4.0, 5.0, 6.0 m. Inclinometer: every 50 cm from 0 to 6.0 m. Soil Moisture: 0.5, 1.0, 2.0, 3.0, 4.0, 5.0, 6.0 m.
WH_1456_BH4	22/05/2020	8 V 471973 6746893	3 m	No sensors were installed

Borehole BH1 (WH_1456_BH1) and BH2 (WH_1456_BH2) were drilled on October 16th and 23rd 2019, respectively, by Midnight Sun Drilling under the supervision of Louis-Philippe Roy and Panya Lipovsky, as seen in Figure 6. The purpose of WH_1456_BH1, was to provide a relatively complete cryostratigraphical record and geotechnical assessment of permafrost in the area and better estimate the risk that the RTS poses on the Alaska Highway. The location of WH_1456_BH1 was selected based on ERT survey WH_1456_ERT2, which showed indications of ice rich sediments at this location. At 10 meters depth, a point of refusal was reached in unfrozen clayey silt sediment. The wall of the borehole started to collapse due to the amount of water intercepting the borehole, threatening to trap the CRREL core barrel in the borehole. WH_1456_BH2 was drilled 2 meters away from WH_1456_BH1 using a Hollow Stem destructive drill to reach the target depth of 25 meters. Once drilling was completed, the boreholes were cased with two 1-inch PVC conduit, and backfilled to the surface using fine gravel and bentonite.



Figure 6. Midnight Sun Drilling CRREL drill rig and permafrost cores (WH_1456_BH1)

Two shallow boreholes, BH3 (WH_1456_BH3) and BH4 (WH_1456_BH4) were drilled in the late spring of 2020 by the Permafrost and Geoscience department of the Yukon University Research Centre (YRC) (Philippe Roy, Fabrice Calmels and Cyrielle Laurent). WH_1456_BH3 was drilled on May 13th 2020, 10 meters beyond the headwall of the RTS. The borehole was created by removing the unfrozen active layer using a shovel down to the thaw front (31 cm). The borehole was drilled using a GÖLZ MT portable core-drill system down to 6.0 meters. The GÖLZTM portable core-drill system is a light hand drill with a high rotation speed (600 rpm) that can be controlled by two people and is therefore used with minimal impact on the environment. Stainless steel rods measuring 1 m in length and 4.5 cm in diameter, and a core barrel 40 cm long and 10 cm in diameter were used, making it possible to drill up to 5 m into unconsolidated, fine to medium grained material (sand to clay). A core catcher was used to extract the frozen core out of the borehole, which allows for continuous undisturbed permafrost sampling.

Once drilling was completed, the borehole was cased with two 1-inch PVC conduits, and backfilled to the surface. This location was specifically chosen close to the headwall so that the conditions leading to failure could be recorded and analyzed to better understand the initiating factors of rapid slump movements. Borehole failure occurred on August 12th 2020, as seen in Figure 7.



Figure 7. WH_1456_BH3 (BH3) failure, image taken on August 13th 2020

WH_1456_BH4 was drilled on May 22nd 2020, 12.6 meters south of WH_1456_BH3 and 23 meters beyond the headwall of the RTS, between the ROW and the slump. The borehole was created by removing the unfrozen active layer using a shovel down to the thaw front (50 cm). The borehole was drilled using a GÖLZ MT portable core-drill system down to 2.97 meters where a point of refusal was reached. The dry nature of the sediment made it extremely hard for the core barrel to cut through the material. Once drilling was completed, the borehole was cased with a 1-inch PVC conduit, and backfilled to the surface.

3.1.2. Grain size, ice content and borehole log analysis

Cores were extracted from WH_1456_BH1 and WH_1456_BH3 allowing for laboratory analyses to measure geotechnical properties of the active layer and permafrost samples. Soil grain characteristics, ice characteristics as well as plasticity index, remolded bulk density, porosity, specific gravity, and thaw settlement potential were calculated for representative samples. To evaluate ice characteristics in permafrost samples, the cryostructure, volumetric ice content, gravimetric ice content and settlement potential were quantified. The specific methods for these analyses are described below. A log for each permafrost borehole was then created by assembling laboratory photos of the cores. Borehole logs include maximal depths, grain size ratio and volumetric excess ice content.

3.1.2.1. Grain size analysis

Sieve and hydrometer analyses of grain size were performed following a specifically modified American Standard and Testing Method protocol (ASTM D422-63, 2000). The sieves used were 4, 2, 1, 0.5, 0.25, 0.125 and 0.063 mm. The data was then compiled in GRADISTAT to generate the statistical analysis and integrated into the borehole log.

3.1.2.2. Ice characteristic analysis

Ice characteristics were assessed by evaluating the cryostructure, as well as measuring the gravimetric ice content, the volumetric ice content, and the volumetric excess ice content, which are described in more detail below.

3.1.2.2.1. Cryostructure

The cryostructure of the cores was described *in situ* during the drilling process, using standard terminology (Stephani et al., 2010; Murton and French, 1994). The classification was validated with the visual analysis of high-resolution pictures of each sample taken in the field.

3.1.2.2.2. Gravimetric ice content

Gravimetric ice content was calculated using the following equation:

$$u_I = \frac{(M_I)}{(M_S)}$$

where M_I is the ice weight (measured as weight loss after drying (g)) and M_S is dry soil weight (g). Results are expressed as percentages (dimensionless).

3.1.2.2.3. Volumetric ice content

Volumetric ice content was measured using a water displacement method. The frozen sample was weighed and lowered into a four-inch diameter PVC tube filled with 1.5 L of water. Water was then extracted from the tube until the initial water level (1.5 L) was achieved. The amount of water displaced was measured using a 250 mL graduated cylinder with a precision of ± 2 mL. The sample was then removed from the tube, placed in a clean tin tray, and dried completely in a drying oven at 60°C. The dry sample was then weighed, crushed using a mortar and pestle, vacuum sealed in a clear plastic bag, and labelled according to the borehole and sample increment. The volumes of the vacuum-sealed dry samples were measured using the same methods as the frozen cores, and the volume of the vacuum bags was subtracted from the measurement to obtain a dry sample volume. Assuming the density of ice to be 1.09 cm³/g, the volumetric ice content was calculated using:

$$IVC_{(\%)} = \left(\frac{W_c \times 1.09}{V_{tot}} \right) \times 100$$

where W_c is the water mass content and V_{tot} is the total (frozen) core volume. Results are expressed as percentages. For the consolidation test samples, the volume has been measured using Glycol displacement. This allowed the possibility to keep the samples under 0°C and avoid the use of vacuumed sealed bags. The volume of excess ice content was calculated using:

$$V_{ice} = V_{tot} - V_{sed}$$

where V_{tot} is the total frozen core volume and V_{sed} is the dry soil volume. The volumetric excess ice content (V_{ice}) is then divided by the total frozen core volume (V_{tot}) and expressed as a percentage (fundamentally meaning cm^3/cm^3). This method is valid for mineral soils only.

3.1.3. Ground temperature and environmental conditions

As mentioned in section 3.1.1, only boreholes WH_1456_BH02 (BH2) and WH_1456_BH03 (BH3) were outfitted with ground temperature sensors (Table 1). Borehole BH2 was instrumented with a 16-channel LogR Systems thermistor and logger to record ground temperatures at 0, 0.5, 1.0, 1.5, 2.0, 3.0, 4.0, 5.0, 6.0, 7.0, 8.0, 9.0, 10.0, 15.0, 20.0 m of depth. The piping was filled with silicone oil to improve the accuracy of the temperature readings. Recording began on February 28th, 2020 at 24:00 and data was last downloaded on December 30th, 2020. Therefore, there are 10 months of ground temperature data available for this borehole.

Borehole BH3 was instrumented with two 4-channel Hobo UX120 loggers to record ground temperatures at 0, 0.5, 1.0, 1.5, 2.0, 3.0, 4.0, 5.0, 6.0 m of depth. The piping was also filled with silicone oil to improve the accuracy of the temperature readings. Recording began on June 1st, 2020 at 18:00 and ended on August 12th, 2020 at 08:00, after a major slumping event caused the slump to retreat beyond the location of the borehole, releasing the piping in the process.

To complement ground temperature data from the thermistors, air temperature and other climatic variables such as precipitation were downloaded from Environment and Climate Change Canada for the Whitehorse Airport.

3.1.4. Inclinerometer

Borehole WH_1456_BH02 was instrumented with a MeasureAnd SAAV Shape Array inclinometer to monitor deformation and slope movements every 50 cm from the surface to 20m of depth, for a total of 41 reading depths. Recording began on April 17th, and data was last downloaded on December 30th, 2020.

Borehole WH_1456_BH03 was also instrumented with a MeasureAnd SAAV Shape Array inclinometer to monitor deformation and slope movements every 50 cm from the surface to 6m of depth, for a total of 13 reading depths. Recording began on June 4th, 2020 at 18:00 and ended on August 12th, 2020 at 08:00, after a major slumping event caused the slump to retreat to the location of the borehole, releasing the piping in the process.

The data were downloaded and processed in the MeasureAnd software SAASuite to convert the data to deformation and deviation values.

3.1.5. Soil moisture

Borehole WH_1456_BH03 was outfitted with METER EC-5 soil moisture sensors at 0.5, 1, 2, 3, 4, 5 and 6 m of depth, and a CR1000X data logger. Recording began on June 1st, 2020, and ended on August 12th, 2020 at 08:00, after a major slumping event caused the slump to retreat to the location

of the borehole, releasing the piping in the process. Due to uncertainties in the sensor's programming, the percentage of soil moisture cannot be assessed. However, by rescaling the data to values between 0 and 1, the moisture values can be compared across the data set to expose any trends. To do so, the min-max normalization method was used, according to the following equation:

$$X_{norm} = \frac{x - x_{min}}{x_{max} - x_{min}}$$

Where X_{norm} is the scaled value of soil moisture;

x_{min} is the minimum value of x across the dataset;

And x_{max} is the maximum value of x across the dataset.

3.2. ERT and EM

3.2.1. Brief introduction to methodologies and novel use of 3D

The specific objective of the 3D geophysics surveys was to perform three-dimensional Electro-resistivity tomography (ERT) and Electro-magnetic (EM) surveys of a square area between the headwall of the RTS and the highway to develop a better understanding of ground ice distribution as well as the groundwater movements occurring within the RTS area.

3.2.2. ERT

Electrical resistivity tomography (ERT) is a geophysical method that passes electrical current through stainless steel electrodes that are driven into the ground surface. A terrameter located at a central "station" measures the resistivity distribution of the subsurface between electrode pairs. Resistivity is the mathematical inverse of conductivity and indicates the ability of an electrical current to pass through a material. Mineral materials (except for specific substances such as metallic ores) are mostly non-conductive. Therefore, variation in the resistivity of a soil or rock profile is governed primarily by the amount and resistivity of pore water present in the profile, and the arrangement of the pores. This makes ERT very well suited to permafrost and hydrology applications. Because most water content in frozen ground is in the solid phase and typically has a higher resistivity than unfrozen water content, permafrost distribution can be inferred based on changes in resistivity between frozen and unfrozen ground.

An ERT system consists of an automated imaging unit and a set of wires connected to an electrode array. The system used for the surveys presented in this report is an ABEM Terrameter LS electrical resistivity and tomography system, consisting of a four-channel imaging unit and four electrode cables, each with 21 take-outs at five-meter intervals. To conduct a survey, 81 electrodes are driven into the ground along a survey line and connected to the electrode cables (Figure 8).

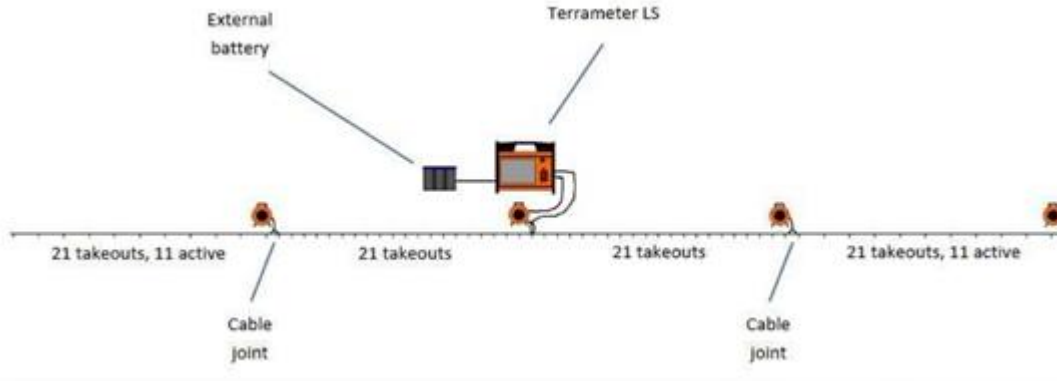


Figure 8. Instrument set-up for ERT surveying

Two different types of electrode configurations or arrays were used during the surveys: the Wenner and dipole-dipole arrays. These arrays differ in how they pair current and potential electrodes (Figure 9). A direct current electrical pulse is sent from the resistivity meter along the survey line in two current electrodes (C1 and C2), and the measurement is performed by two potential electrodes (P1 and P2). The resulting data consists of a cross-sectional (2D) plot of the ground's resistivity (ohm·m) versus depth (m) for the length of the survey.

<p>Wenner</p> <p>C1 P1 P2 C2</p> <p>$k = 2 \times a$</p>	<p>Wenner Beta</p> <p>C2 C1 P1 P2</p> <p>$k = 6 \times a$</p>
<p>Wenner Gamma</p> <p>C1 P1 C2 P2</p> <p>$k = 1.5 \times a$</p>	<p>Pole - Pole</p> <p>C1 P1</p> <p>$k = 2 \times a$</p>
<p>Dipole - Dipole</p> <p>C2 C1 P1 P2</p> <p>$k = x \cdot n(n+1)(n+2)a$</p>	<p>Pole - Dipole</p> <p>C1 P1 P2</p> <p>$k = 2 \times n(n+1)a$</p>
<p>Schlumberger</p> <p>C1 P1 P2 C2</p> <p>$k = x \cdot n(n+1)a$</p>	<p>Equatorial Dipole - Dipole</p> <p>C2 P2</p> <p>C1 P1</p> <p>$k = 2 \times a \cdot s / (s-a)$</p> <p>$s = (a+a + b \cdot b)^{0.5}$</p>
<p>NOTES: k = geometric factor C = current source electrodes P = potential (measuring) electrode a = electrode separation; n = an integer</p>	

Figure 9. Survey configurations or "arrays" for ERT surveying

In general, the Wenner array is good in resolving vertical changes (i.e. horizontal structures), but relatively poor in detecting horizontal changes (i.e. narrow vertical structures). Compared to other arrays, the Wenner array has a moderate depth of investigation. Among the common arrays, the Wenner array has the strongest signal strength. This can be an important factor if the survey is carried in areas with high background noise. Relatively small current magnitudes are needed to produce measurable potential differences. The disadvantage is that to image deep into the earth, it is necessary to use longer current cables. The Wenner array is also very sensitive to near surface inhomogeneities which may skew deeper electrical responses. One disadvantage of this array for 2-

D surveys is the relatively poor horizontal coverage as the electrode spacing is increased, which can be a problem when using a system with a relatively small number of electrodes.

The dipole-dipole array is very sensitive to horizontal changes in resistivity, but relatively insensitive to vertical changes in the resistivity. That means that it is good for mapping vertical structures, such as dykes and cavities, but relatively poor in mapping horizontal structures such as sills or sedimentary layers. This array can have a shallower depth of investigation compared to the Wenner array, but it has better horizontal data coverage than the Wenner, which can be an advantage when the number of nodes available with the multi-electrode system is small. One possible disadvantage can be a very small signal strength. With the proper field equipment and survey techniques, this array has been successfully used in many areas to detect structures such as cavities where the good horizontal resolution of this array is a major advantage.

There is no single model that fits the observed resistivities. Instead, the modelled results converge by iteration with the measured values. The choice of when to stop iteration in the RES2DINV software is made by the operator. Too few iterations lead to large Root Mean Square (RMS) errors (i.e., the model does not fit the measurements). Too many iterations can result in model 'over-fit' in which the broad patterns are lost. Analyses for this study were stopped after the 4th iteration as RMS errors were all very low (less than 5%) by that point. The profiles are presented with a linear depth scale and no vertical exaggeration. ERT profiles were interpreted in conjunction with the results of frost probing along the profiles, field descriptions of vegetation cover at the site, borehole and laboratory analyses undertaken by the research team, and surficial mapping. Results of the surveys are post-treated and analyzed at the YRC using inversion software (Res2DInv 64 and Res3DInv 32).

The specifications for the ERT surveys are shown in Table 2 below, and their locations in Figure 10 below.

Table 2. ERT survey specifications

WH_1456_ERT1	30/5/2019	Dipole-Dipole & Wenner	Length: 200 m	Electrode Spacing: 2.5 m
0 m		8 V 472063 6746934		
50 m		8 V 472017 6746915		
100 m		8 V 471969 6746906		
150 m		8 V 471919 6746905		
200 m		8 V 471871 6746896		
WH_1456_ERT2	27/06/2019	Dipole-Dipole & Wenner	Length: 200 m	Electrode Spacing: 2.5 m
0 m		8 V 472080 6746905		
50 m		8 V 472034 6746889		
100 m		8 V 471985 6746876		
150 m		8 V 471938 6746862		
200 m		8 V 471887 6746857		
WH_1456_ERT3	20/08/2019	Dipole-Dipole	Length: 500 m	Electrode Spacing: 2.5 m
0 m		8 V 471908 6746785		
100 m		8 V 472003 6746814		
200 m		8 V 472098 6746843		
300 m		8 V 472194 6746871		

400 m		8 V 472290 6746898		
500 m		8 V 472385 6746927		
WH_1456_ERT4	11/9/2019	Dipole-Dipole	Length: 500 m	Electrode Spacing: 2.5 m
0 m		8 V 471900 6746826		
100 m		8 V 471998 6746853		
200 m		8 V 472093 6746880		
300 m		8 V 472184 6746907		
400 m		8 V 472280 6746935		
500 m		8 V 472378 6746964		

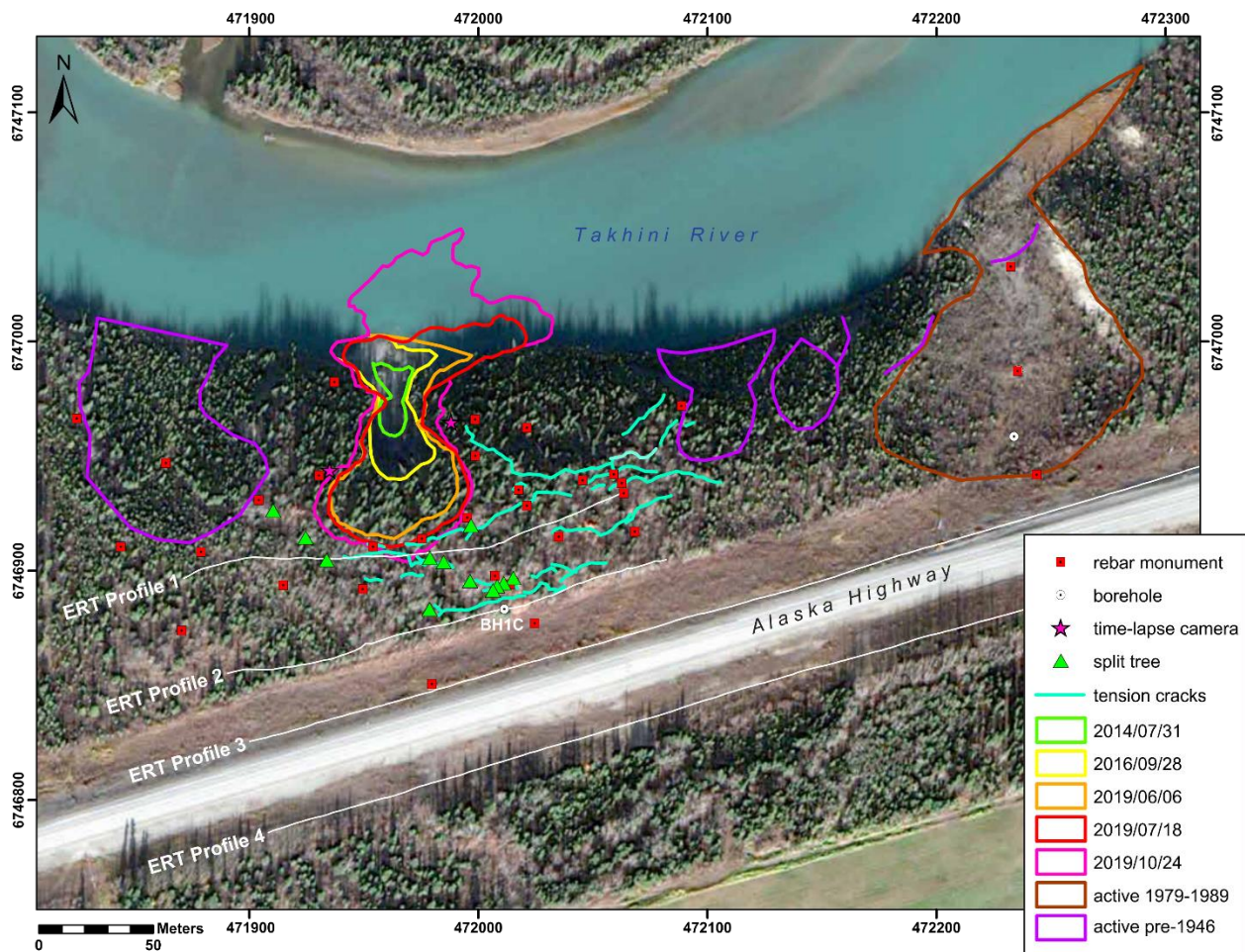


Figure 10. Field site with ERT survey lines

3.2.3. 3D Surveys

The approach merges 2 techniques, ERT and EM. EM systems are used to measure electrical and magnetic ground properties. Consisting of a transmitter and a receiver these instruments are suited for mineral exploration and geological mapping, but also can be used in permafrost science, in a

similar way to electrical resistivity tomography (ERT). The EM System has the advantage of being a quicker acquisition technique, but it has not been tested thoroughly in permafrost environments compared to ERT. By acquiring measurements following a grid pattern on the investigated zone, the Yukon University system can be used to develop a 2D mapping of EM properties of the underground using 3 frequencies at the same time, i.e., to produce three 2D horizontal EM maps at 3 different depths at once. The three 2D maps, or slices, are then integrated together to produce a 3D model of the EM properties for the investigated area, where any vertical and/or horizontal slices of the EM properties can be extracted and interpreted.

By calibrating and comparing EM data with borehole and ERT data, the project aims to map and assess ground conditions that may play a role in the RTS development: thickness of the active layer, thermal state of the ground (frozen/unfrozen), presence of ground ice; groundwater movement patterns (absence/presence).

The survey grid

A 40 by 40 m grid with data acquisition nodes located every two meters, was designed in ArcGIS based on UAV imagery. The grid was then set up on site using stakes and cords, and nodes were surveyed with a DGPS (Figure 11).



Figure 11. Grid used for EM and 3D ERT surveys

3.2.3.1. 3D ERT

For the 3D ERT survey, the ABEM Terrameter only used one electrical cable with 21 take-outs at two-meter intervals to acquire 21 parallel ERT surveys located two meters apart along 20 m survey lines.

Each node corresponding to the location of an electrode, the 21 surveys covered the entire 40 m x 40 m grid. The twenty-one 2D ERT profiles were created using a dipole-dipole array following the east-west direction. The resulting data consists of a cross-sectional (2D) plot of the ground's resistivity (ohm·m) versus depth (m) for the length of the survey.

After field data acquisition, RES3DINV software was used to integrate the 21 surveys and produce a 3D resistivity model. RES3DINV is a computer program that automatically determines a three-dimensional (3-D) resistivity model for the subsurface using the data obtained from the 3-D electrical imaging survey. The process was facilitated by the fact that electrodes were arranged in an orthogonal grid. While RES3DINV produces 3D model data, it does not produce 3D rendering, and only allows for the visualization of 2D resistivity profile. For 3D rendering, Voxler, a 3D graphics package by Golden Software, was used. The 3D graphics suite also allowed for the combination of the ERT and EM models in a single 3D rendering.

3.2.3.2. Electromagnetic surveys

A frequency-domain, ground electromagnetic survey was conducted over the field area on June 25th and 26th, 2020.

Electromagnetic geophysical techniques are based on the following principle: a primary electromagnetic field (H_p) induces an alternating current in conductive subsurface bodies (Figure 12), which in turn generates a secondary electromagnetic field (H_s) that is a contrary direction to the primary field. The primary current is induced by an alternating current in a transmitter coil on the instrument, and the resultant electromagnetic field is measured by a receiver coil is a combination of the primary and secondary fields ($H_r = H_p + H_s$). Data analysis considers the difference between the primary and secondary currents in terms of delay (time domain) or frequency (frequency domain). In frequency domain instruments, the ratio of the induced secondary magnetic field to the primary magnetic field is directly proportional to the ground's bulk or apparent conductivity. The shape of the transmitted signal can be varied, enabling heightened characterization of a body's size and conductivity.

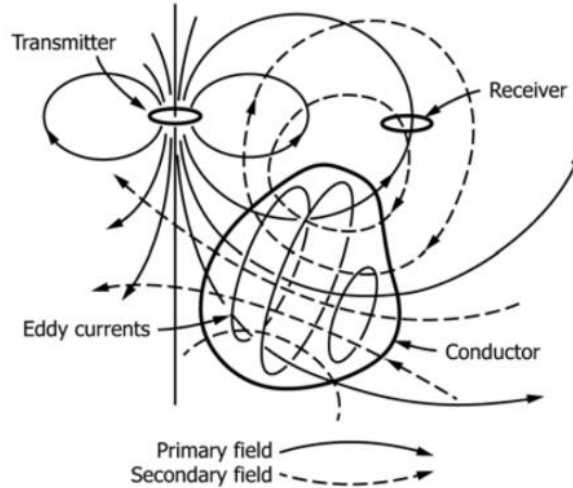


Figure 12. Principles of electromagnetic induction (Sheriff, 1989). Vertical dipole (horizontal loop) configuration is shown.

Common frequency-domain electromagnetic instruments typically operate under the “low induction number approximation,” which is a function of the separation between transmitter and receiver, the electrical permeability and conductivity of the ground, and the frequency of the transmitter signal. In the absence of metallic objects in the subsurface, the ratio of the magnitude of the secondary magnetic field to the primary magnetic field (H_s/H_p) is directly converted to an apparent conductivity (σ_a) measurement of earth material (Eq. 1). Outside of the approximation (e.g., where the apparent conductivity > 50 mS/m; Weymer, 2016), the direct correlation of signal response to σ_a breaks down and there is a departure of measured σ_a from “true conductivity,” σ . The depth of site characterization is related to the frequency of the alternating current, the distance between the transmitter and receiver coils (intercoil spacing) and coil orientation.

$$\sigma_a = \left(\frac{4}{\omega * \mu_0 * s^2} \right) * \left(\frac{H_s}{H_p} \right)$$

where

σ_a = apparent conductivity in Siemens/meter (S/m)

$\omega = 2\pi f$ in radians/sec; f = frequency in hertz (Hz)

μ_0 = the permeability of free space ($4\pi \times 10^{-7}$ Henry/m; H/m)

s = intercoil spacing in meters (m)

H_s = out-of-phase (quadrature) component of the secondary magnetic field, both measured by the receiver coil;

H_p = out-of-phase (quadrature) component of the primary magnetic field, both measured by the receiver coil;

Instruments usually measure two components of the secondary magnetic field: a component in-phase with the primary field and a component 90° out-of-phase with the primary field (the quadrature component). When ground conditions are such that the low induction number approximation is valid, the in-phase component is dwarfed by the quadrature phase component. If there is a large in-phase response, then the approximation is not valid and there is likely a very conductive body or layer in the subsurface. Specific earth materials can have a large variation in conductivity, which is related to temperature, particle size, porosity, pore fluid saturation, and pore fluid conductivity. Permafrost has low conductivity typically below 1 milliSiemens/meter (mS/m). Importantly, frequency-domain instruments are best used under relatively high electrical conductivity conditions (>1 mS/m). For values less than this, i.e., those most commonly recorded for permafrost samples, better results are obtained with DC resistivity methods (Figure 13).

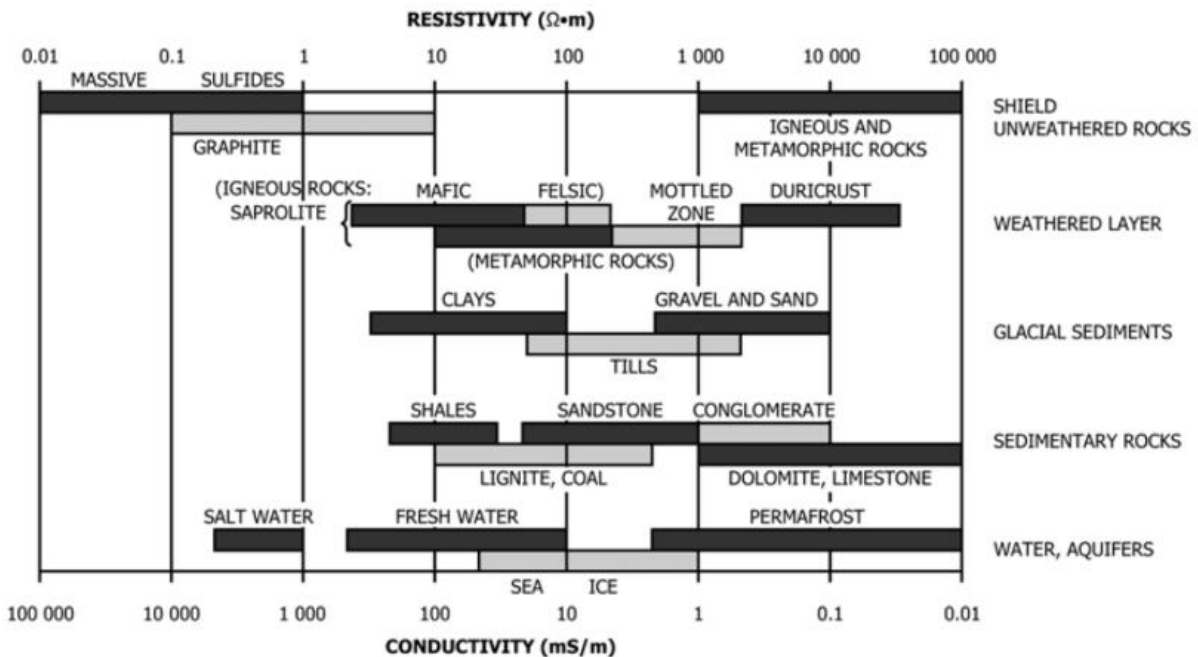


Figure 13. Conductivity ranges for common Earth materials (Sheriff, 1991)

This survey utilized a Profiler EMP-400 survey instrument manufactured by Geophysical Survey Systems, Inc. (GSSI). The EMP-400 is a single user instrument with an inline, 1.29 m (4 ft.) fixed coil spacing. Data was collected at 6 separate frequencies (1, 4, 7, 10, 13, 16 kHz); a low-carry handle was used to maintain a deployment height of ~6 inches (15 cm) above the ground surface.

The data were collected along the 40 x 40 m grid that was laid out over the study area, where each node was a measurement point. Data were collected on two successive days (frequencies 10, 13, and 16 kHz on Day 1; frequencies 1, 4, and kHz on Day 2). There was no precipitation between the two surveys at the study site and temperatures were stable; no significant changes in subsurface conditions (e.g., ground saturation) should have occurred between the two data collection sessions. The two sessions were necessitated by battery life on the instrument and handheld Trimble unit. A

stacking value of 8 was used at all nodes, i.e., eight individual readings were averaged at each collection point. A 60 Hz filter was applied during data collection.

Data are presented as six depth slices corresponding to the six frequencies. Gridding was performed using an inverse distance weighted gridding algorithm. Higher frequency data represent shallower depths, while lower frequencies have greater depth penetration. Absolute depth determination is difficult without additional intercoil spacings and/or a change to a horizontal dipole configuration, however, fixed coil systems typically have depth of investigation (DOI) limits of 6 m. Depth of investigation is strongly influenced by the geological materials underfoot.

3.3. Geospatial analyses

A variety of geospatial analyses were carried out to characterize the site location. These analyses include UAV data to quantify changes in slump morphology, and benchmark surveys to quantify small movements and discern error in geospatial data. Additionally, historical aerial and satellite imagery were analyzed to better understand the morphological history of the site.

3.3.1. UAV image collection and processing methodology

The thaw slump located at km 1456 on the Alaska Highway has been regularly surveyed with UAVs (drones) for aerial image collection since August 2019.

3.3.1.1. Data collection

The surveys have been completed using two models of drones, the DJI Phantom 4 Pro V2 and the DJI Matrice RTK 210. The Phantom 4 Pro V2 is equipped with a camera producing 20MP images. When using this model, targets were placed on the ground with their position geolocated using a DGPS. The target's locations were used as ground control points (GCP) to produce centimeter-scale positional accuracy for the image processing outcome products.

The Matrice 210 RTK carries a Zenmuse x7 (35mm) producing 24MP images. The RTK system of this drone offers a centimeter-scale positional accuracy not requiring the use of targets.

Mapping grids of various size (all covering the active slump area) were used with 2 different flight altitude, as indicated in Table 3.

Table 3. Flight mission specifications

Dates	Drones	Mapping grid size	Flight altitude	Image resolution
22-08-2019	Phantom 4 Pro V2	81x67m	60m	1.66cm
11-09-2019	Phantom 4 Pro V2	205x181m	100m	2.77cm
25-09-2019	Phantom 4 Pro V2	527x194m	100m	2.77cm
20-05-2020	Phantom 4 Pro V2	529x194m	100m	2.77cm

11-06-2020	Phantom 4 Pro V2	529x194m	100m	2.77cm
13-07-2020	Phantom 4 Pro V2	237x194m	100m	2.77cm
26-08-2020	Matrice 210 RTK, Zenmuse x7	347x193m	100m	1.11cm
29-09-2020	Matrice 210 RTK, Zenmuse x7	347x193m	100m	1.11cm

3.3.1.2. Image processing

Images were processed using Agisoft Metashape Professional photogrammetry software. For each survey, a point cloud, a 3D model including mesh mapping and texture, a digital surface model (DSM), and an orthomosaic were produced. All final products were projected using UTM zone 8.

Orthomosaics were used to digitize the headwall of the thaw slump with ArcGIS to measure the progression of the slump and its distance from the road at each acquisition date. Table 4 indicates the resolution for all DSMs and orthomosaics.

Table 4. Image resolution for DSM and orthomosaics

Dates	Drones	DSM resolution	Orthomosaic resolution
22-08-2019	Phantom 4 Pro V2	2.66cm	1.33cm
11-09-2019	Phantom 4 Pro V2	5.40cm	2.70cm
25-09-2019	Phantom 4 Pro V2	5.94cm	2.97cm
20-05-2020	Phantom 4 Pro V2	5.20cm	2.60cm
11-06-2020	Phantom 4 Pro V2		
13-07-2020	Phantom 4 Pro V2	5.20cm	2.60cm
26-08-2020	Matrice 210 RTK, Zenmuse x7	2.29cm	1.14cm
29-09-2020	Matrice 210 RTK, Zenmuse x7	2.36cm	1.18cm

3.3.2. Benchmark survey

To quantify small ground movements in the slump area, as well as quantify the error in the differential GPS measurements, a benchmark survey was conducted. This survey included creating 36 rebar benchmarks (Figure 14) that would be surveyed multiple times throughout the field season (beginning in May 2019) using a Trimble R8s differential GPS (DGPS) system. The orthogonal dispersion of the DGPS measurement points (the dispersion in x and y directions) was used to

calculate the standard deviation (SD) of measurements in the x and y directions (SDx and SDy). This analysis was performed using the calc_box function from the R package aspace.

Few points move significantly in the x direction, so the mean SD calculated for this direction (\overline{SDx}) is considered reliable. However, many points move significantly in the y direction, skewing the mean SD of the y direction (\overline{SDy}). Therefore, to resolve the high \overline{SDy} , a threshold value above which values of SDy are deemed to be noise was set as \overline{SDx} . Benchmarks with $SDy \leq \overline{SDx}$ were used to determine \overline{SDy} . Benchmarks with SDy slightly greater than this threshold were examined, and shown to have minimal movement, indicating that if a point begins to move, it will exceed the threshold and be excluded from the determination of \overline{SDy} . Then, to quantify the movement of each benchmark in meters, the distHaversine function from the geosphere R package was used, which calculates the shortest distance between two points using the haversine (half-versed-sined) method. This function allows for the distance between the most recent measured coordinate and the original measurement to be calculated, thereby tracking movement. This analysis will therefore allow for quantification of small ground movements in the study area, as well as an assessment of error in the DGPS system.

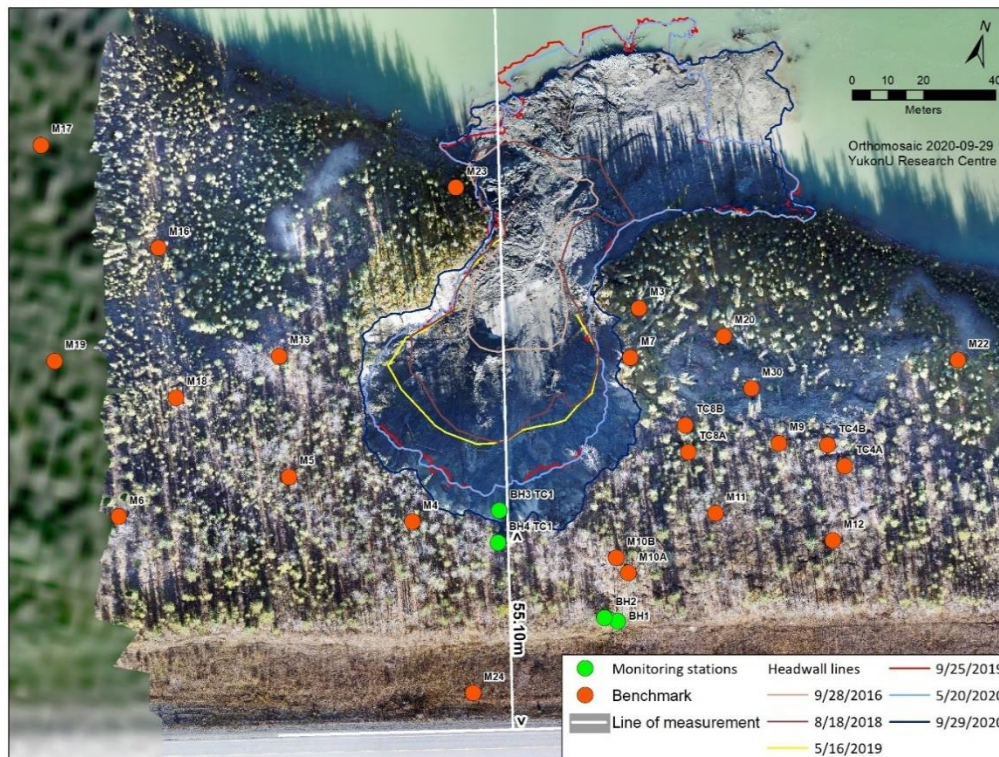


Figure 14. Benchmark survey monuments location and retrogressive thaw slump progression

4. Results

4.1. Geotechnical boreholes

4.1.1. Grain size, ice content and borehole log analysis

The borehole log (shown in Appendix A, No1) for WH_1456_BH1 shows a stratigraphy composed predominantly by clayey silt. The borehole ends at 10 meters in silty sediment (99.9 % silt). Lenticular, micro lenticular, reticulate and suspended cryo-structures (Figure 15) were identified along the profile and the volumetric excess ice content ranged from 13 to 41%. The horizon from 4.5 to 10 meters contained the highest excess ice content. Overall, the borehole has a mean volumetric excess ice content of 32.5% (Table 5).



Figure 15. Ice rich permafrost showing thick layered (left) and suspended (right) cryostructures in a core from WH_1456_BH1 at 657 centimeter depth.

Table 5. Geotechnical data. Grain-size and excess ice content results

Sample	Excess Ice %	Cobble %	Gravel %	Sand %	Silt %	Clay %
WH_1456_BH1_0	0.00	0.00	0.04	4.08	72.51	23.38
WH_1456_BH1_152	0.00	0.00	0.09	91.79	7.54	0.58
WH_1456_BH1_304	0.00	0.00	0.00	5.48	79.81	14.71
WH_1456_BH1_335	14.09	0.12	0.00	2.67	78.65	18.56
WH_1456_BH1_457	30.66	0.00	0.00	2.94	83.57	13.49
WH_1456_BH1_480	34.64	0.00	0.00	8.03	81.66	10.31
WH_1456_BH1_563	35.78	0.00	0.00	0.21	90.28	9.51
WH_1456_BH1_596	36.24	0.00	0.01	0.58	76.73	22.67
WH_1456_BH1_657	39.22	0.00	0.00	0.38	85.70	13.92
WH_1456_BH1_703	36.39	0.00	0.00	0.08	64.31	35.61
WH_1456_BH1_745	34.62	0.00	0.00	0.16	92.19	7.65
WH_1456_BH1_785	13.36	0.00	0.00	1.20	87.05	11.75
WH_1456_BH1_822	39.50	0.00	0.00	0.01	67.70	32.29
WH_1456_BH1_850	36.59	0.00	0.00	1.70	87.41	10.89
WH_1456_BH1_878	41.63	0.00	0.00	0.06	68.13	31.81
WH_1456_BH1_915	26.34	0.00	0.00	0.12	70.13	29.75
WH_1456_BH1_940	33.88	0.00	0.00	0.15	99.85	0.00

The borehole log for borehole WH_1456_BH3 (BH3) (Appendix A, No2) shows layers of ice rich gray clayey silt alternating with some very ice rich layers. While drilling was initiated in frozen ground, at approximately 2 m depth a thin unfrozen section of soil with the presence of ground water depth was encountered. The borehole extends to six meters with clayey-silt sediment. Lenticular and micro lenticular cryo-structures were identified along the profile (Figure 16).



Figure 16. Ice rich permafrost core showing suspended cryostructure collected from borehole WH_1456_BH03

The grain size distribution of sediments determines the porosity and hydraulic conductivity of the ground. Coarse material (medium sand and coarser) has a high hydraulic conductivity and readily drains water as ice melts, whereas fine-grained material drains poorly once it thaws due to its low hydraulic conductivity. Furthermore, fine-grained sediments often contain excess ice (i.e., the volume of ice in exceedance of the total pore volume of the ground when unfrozen) and may form ice lenses or layers by ice segregation. On flat terrain, ground with excess ice will undergo severe thaw settlement; likewise, on slopes, silt and clay deposits may experience mass movement when the pore water pressure created by melting ice is high. For slope deposits, the plastic and liquid limits of the material are used to evaluate the potential for ground failure.

The nature of the ground ice is segregated with the dominant cryostructures being suspended and thick layered ice. These types of cryostructures form in ground where the freezing front progresses slowly (low thermal gradient) with a ground water supply sufficient to accommodate the growth of thick ice layers and lenses. Usually, the thickness of the ice layer increases with depth as the freezing plane slows down. This type of cryostratigraphical record is consistent with an epigenetic discontinuous permafrost such as encountered in wet, frost-heave mounds and permafrost plateau environments.

4.1.2. Ground temperature and environmental conditions

Air temperature and precipitation data from the Whitehorse Airport weather station for April 17 to December 31st can be seen in Figure 17 below (A and B). Figure 17 C and D shows the ground temperature for boreholes 2 and 3 from the thermistors. Trumpet curves for boreholes 2 and 3 can be seen in Figure 18 below. The trumpet curves in Figure 18 suggest that the top of permafrost is between 3 meters (BH3) and 4 (BH2) meters, and reaches a depth of 8m, suggesting that the permafrost is 4-5m deep (see limitation below). In BH3, the ground is frozen below 3m to the bottom of the borehole (6m) for the duration of the recording period (June 5th until the borehole failure on August 12th).

Overall, the ground temperature data suggest that temperatures below 0 °C do not persist below 8m of depth. It is possible that this is due to the disturbance caused by the drilling process, which may upset the thermal regime by thawing the permafrost around the borehole. While it is possible that the temperatures will stabilize over time, the disturbance could be permanent. Interpretations of the permafrost boundaries based on ground temperatures in the boreholes should be considered with caution.

An important amount of ground water was observed during the drilling process, which could be causing the ground temperatures above the freezing point. We believe that even if the mean ground temperature is slightly above 0°C, the significant amount of ice present in the ground is preventing permafrost from thawing because of the latent heat (the amount of heat required to melt all the ice in a unit of soil or rock) absorption required to change ice to liquid water, therefore reducing the warming effect.

Temperature data from BH 3 (Figure 18B) show that as the headwall retreats towards the borehole, temperatures at 0.5 and 1m of depth steadily increase beginning on the 6th of August. A less prominent increase is also seen beginning on August 6th at 3-6 m of depth.

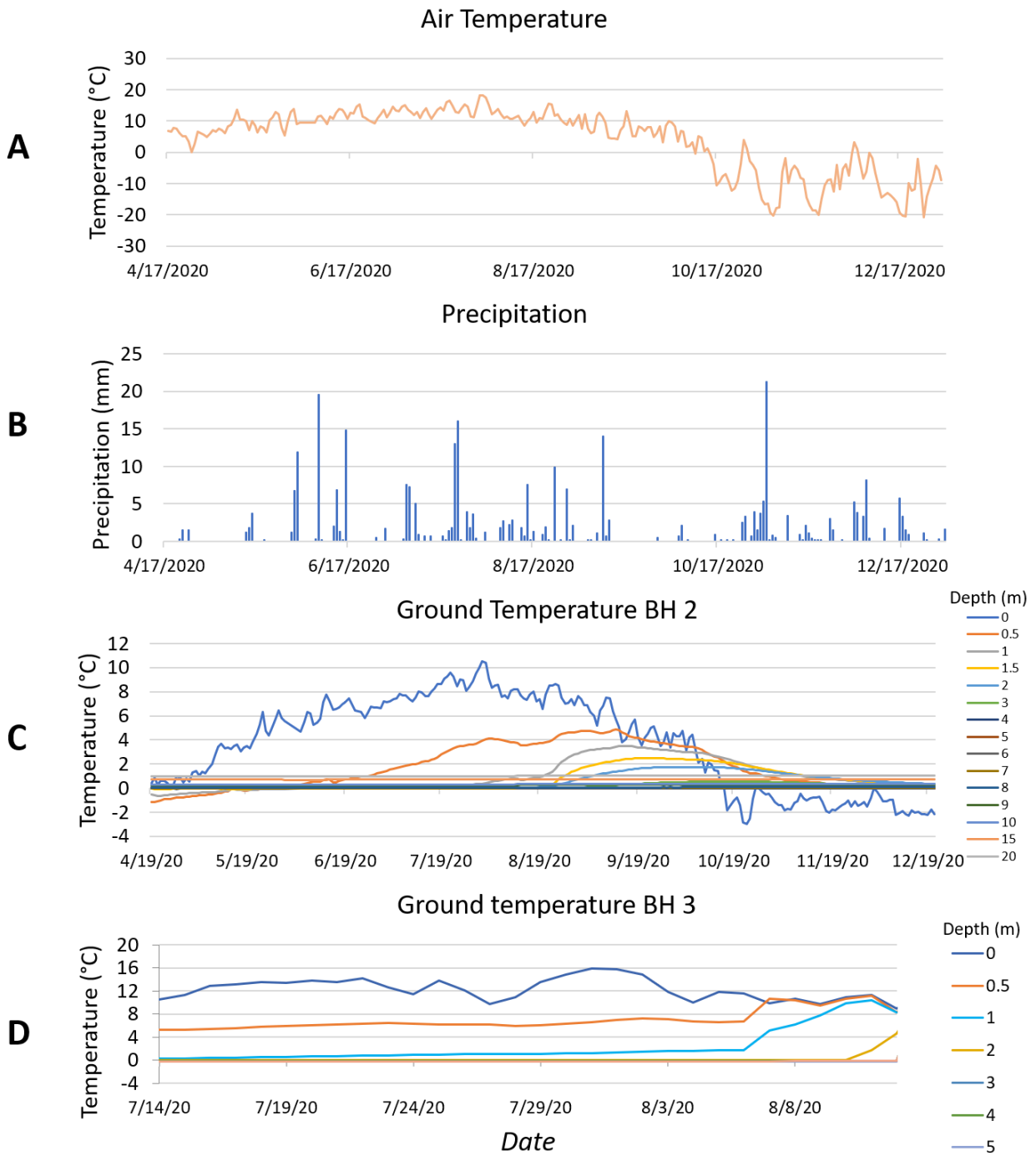
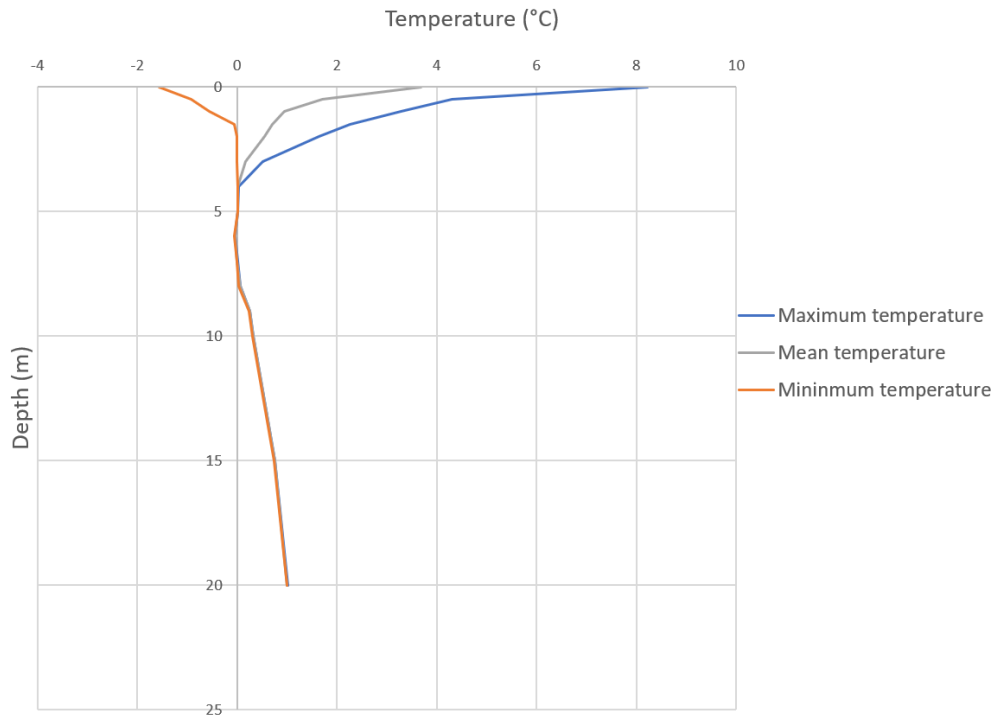


Figure 17. Environmental factors for study site including: A) Air temperature; B) Precipitation; C) Ground temperature for BH2; and D) Ground temperature for BH3 (notice change in x-axis)

A



B

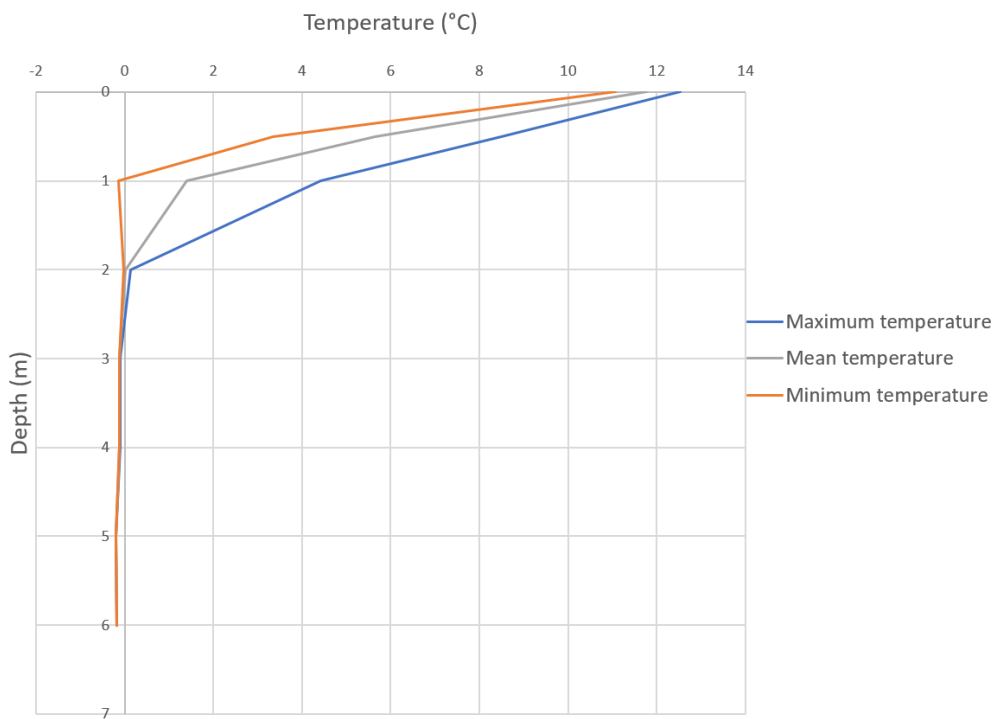


Figure 18. Trumpet curves for A) BH2 using temperature data from April to December 2020; B) for BH3 using temperature data from June to August

4.1.3. Soil moisture

Despite the limitations of the soil moisture data from the METER-EC 5 soil moisture sensors in Borehole 3, the normalization of the data allows for an adimensional analysis of trends in soil moisture leading up to the failure of the slump. Figure 19 below shows the variations in the normalized soil moisture from June 2nd until the slump failure on August 12th. There was little variation in soil moisture for all depths until the beginning of August, showing trends similar to those seen in the temperature data. The greatest increase is seen at depths of 1 m and 5 m on August 6th, though increases are seen at all depths on the same date except for at 2 m, where an increase in soil moisture is seen on August 10th.

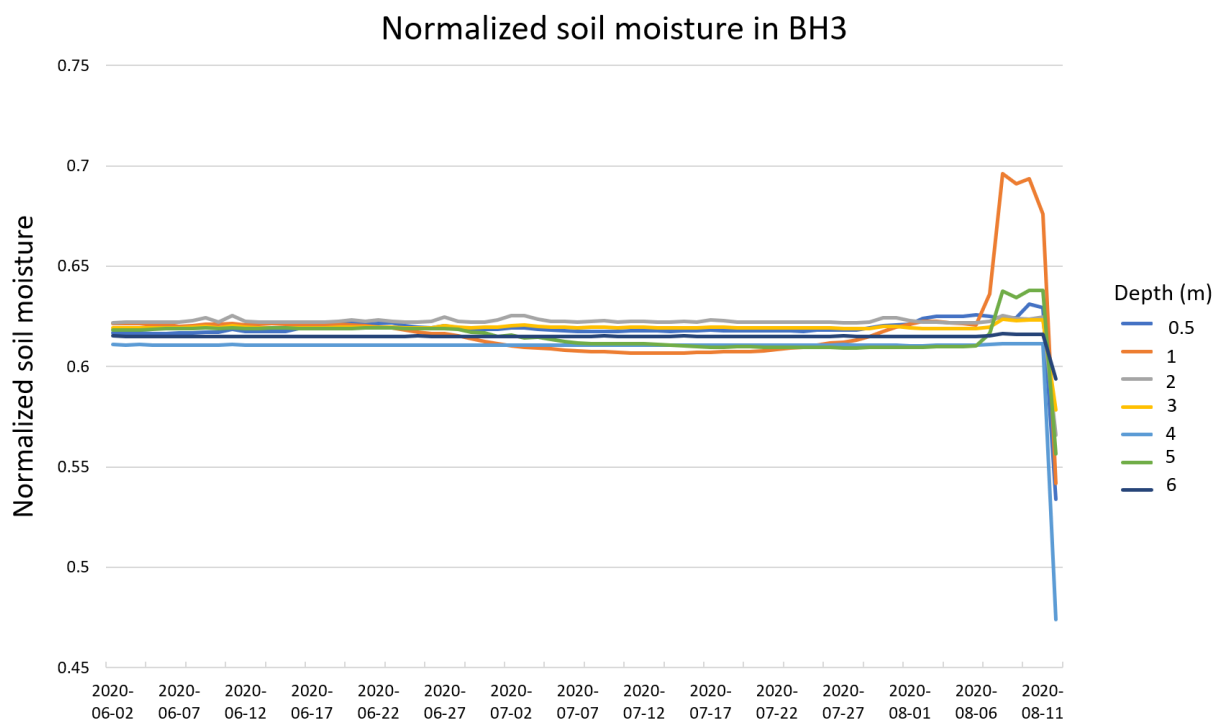


Figure 19 Daily normalized soil moisture in BH3 from June 2nd to August 12th 2020

4.1.4. Inclinator

The inclinometer data from Measureand's ShapeArrays in Boreholes 2 and 3 provide information on soil deformation and movement in the slump area. Figure 20 and Figure 21 below show the movement of the sensor at multiple depths for Boreholes 2 and 3, respectively. The movement in Borehole 2 is relatively constant with some minor gaps due to missing data or suspected interference during field visits. There is a noticeable movement at the surface that decreases in importance with depth on August 12th at the time of the major headwall retreat event. The August 12th movement is predominantly a downslope one (in the y-direction), of approximately 10 mm (Figure 20). The sensor

movements within the borehole are oscillating (backwards and forwards) throughout the recording period. Therefore, the absolute displacement only amounts to 5 mm in the x-direction and 22 mm in the y-direction at the surface (less than the sum of all relative movements) over the entire recording period (April-December).

In BH3, the movements are much more significant. The array is stable in BH3 until a movement is initiated on August 6th by 200 mm in the x and y directions, followed by another 200 mm movement (predominantly in the y-direction) (Figure 21). A final 600 mm movement in the y direction (downslope) on August 12th represents the borehole failing due to the retreat of the slump headwall (Figure 21). The absolute displacement amounts to 237 mm in the x-direction and 1160 mm in the y-direction at the surface (less than the sum of all relative movements).

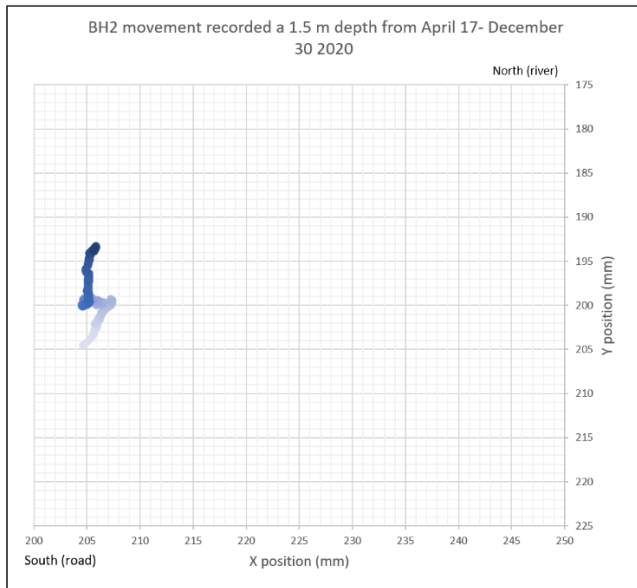
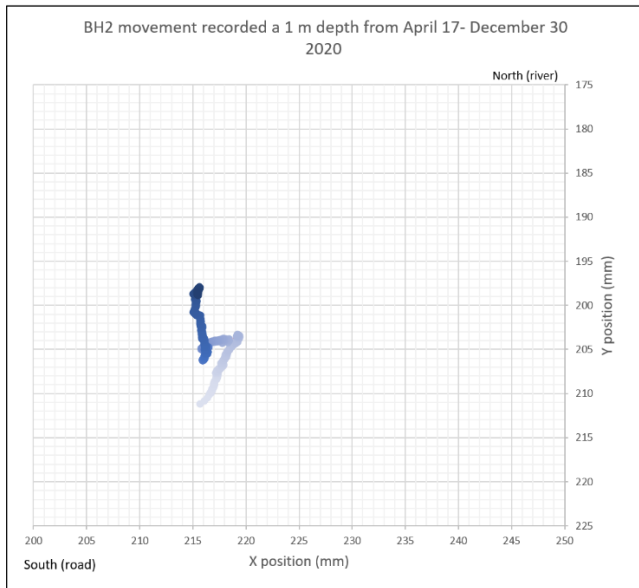
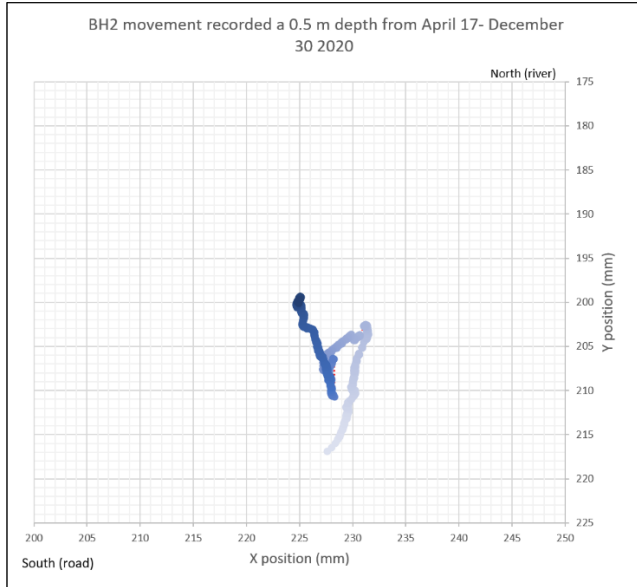
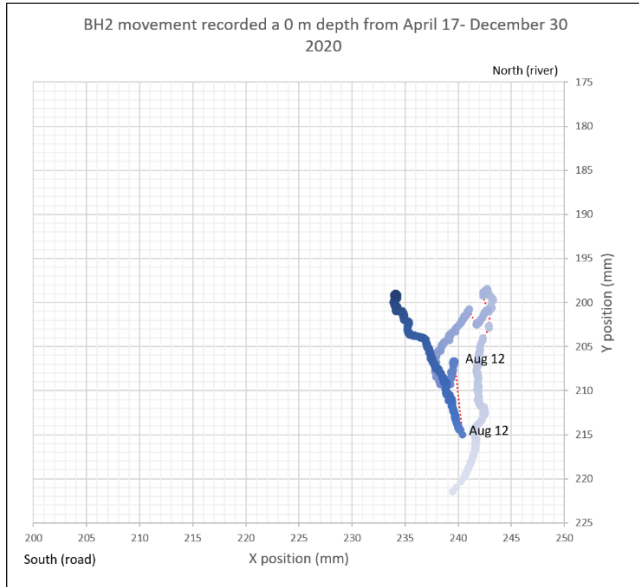


Figure 20. Cumulative deviation from initial position on April 17th to final recording on December 30th 2020 in BH2 for 0, 0.5, 1 and 1.5 m depth

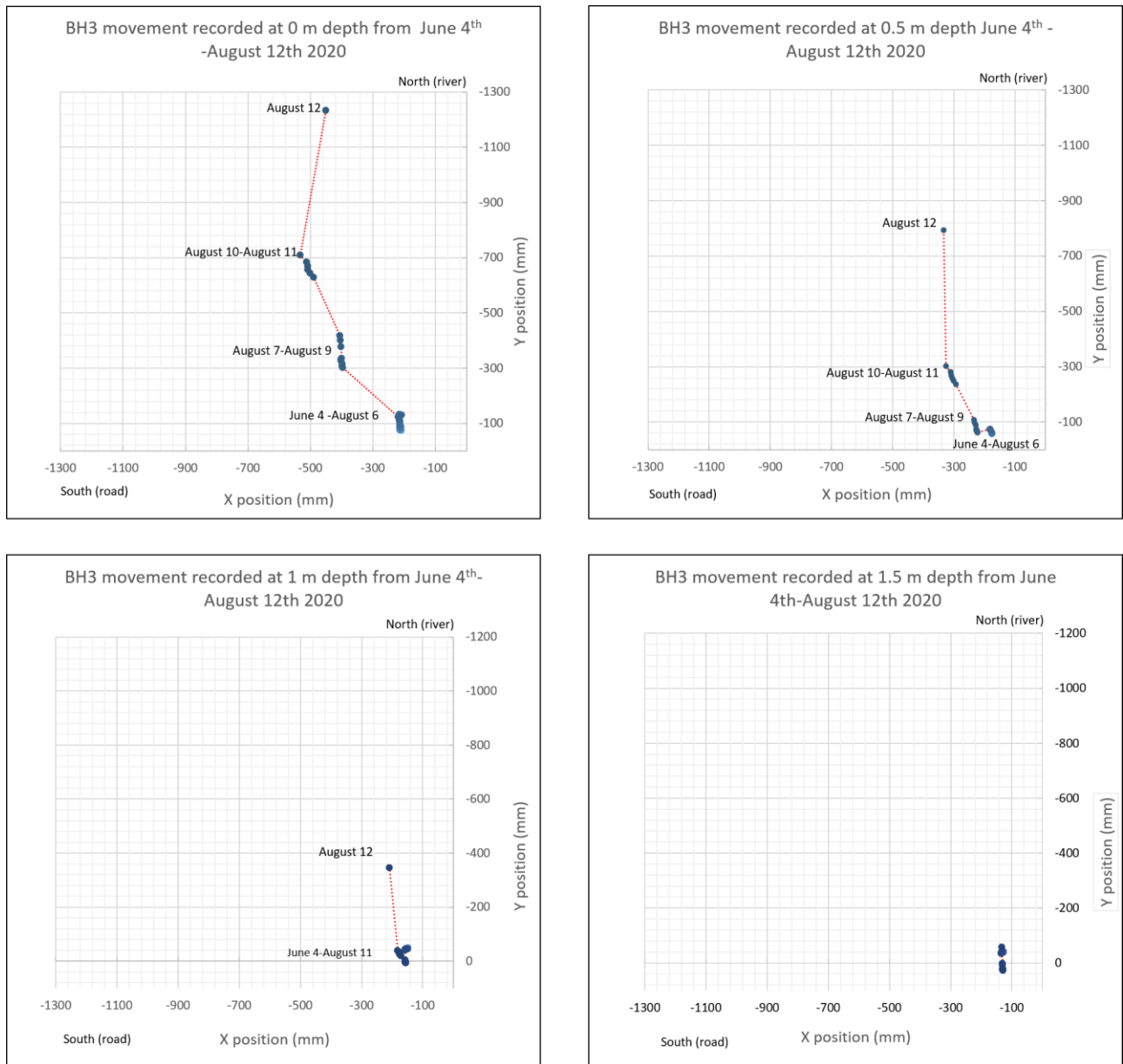


Figure 21. Cumulative deviation from initial position on June 4th to final recording on August 12th 2020 in BH3 for 0, 0.5, 1 and 1.5 m depth

The inclinometer data provides a clear picture of ground movement close to the slump in BH3. The data recorded in BH3 from June until the borehole failure on August 12 provides a unique window into the failure processes occurring in the slump. The trends of the movements at multiple depths are extracted from this record and give an understanding of the mechanics leading to the failure. The daily change between positions was computed and is shown in Figure 22 for depths up to 1.5m where the most important movement occurred. This change in daily slopes shows trends similar to those of the ground temperature data (Section 3.1.3), with little movement up until the 6th of August, at which point there is increased movement leading up to the slumping event. This trend is also seen if the change in position is downscaled to three-day movements (Figure 23).

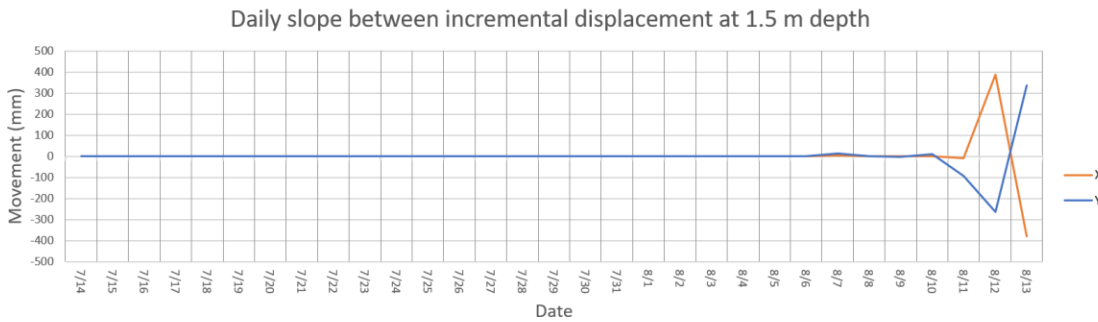
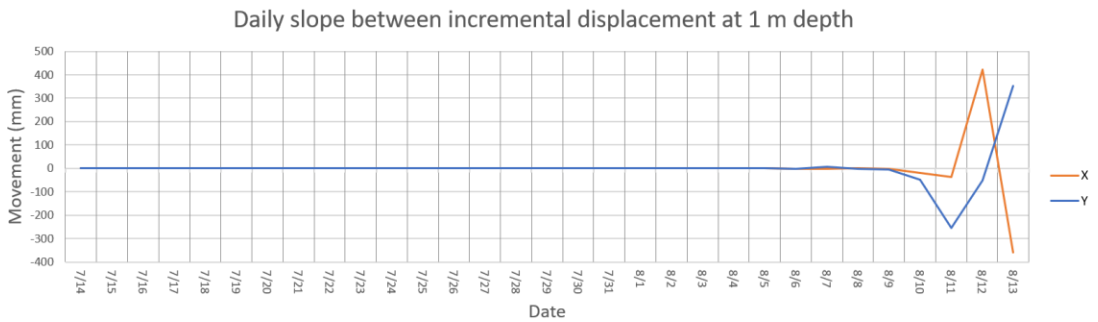
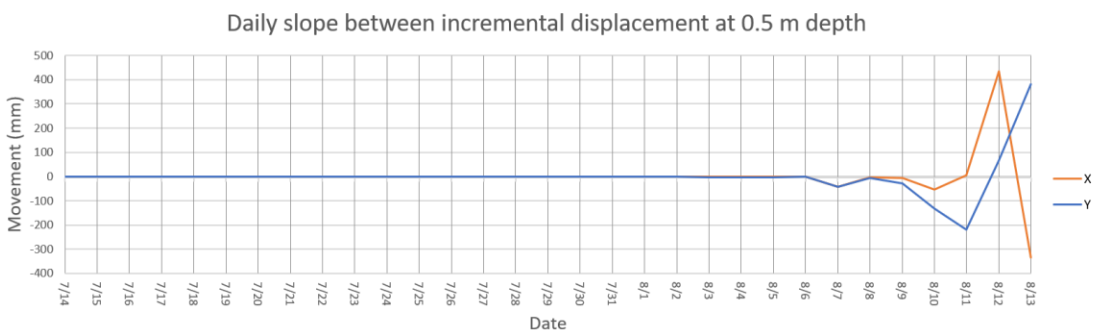
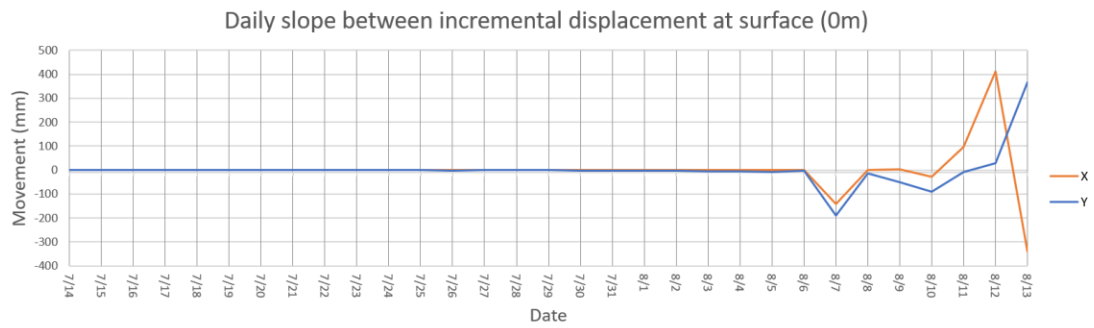


Figure 22. Daily change in position (slope) for surface; 0.5 m depth; 1 m depth; and 1.5 m depth between July 14th and August 12th in BH3

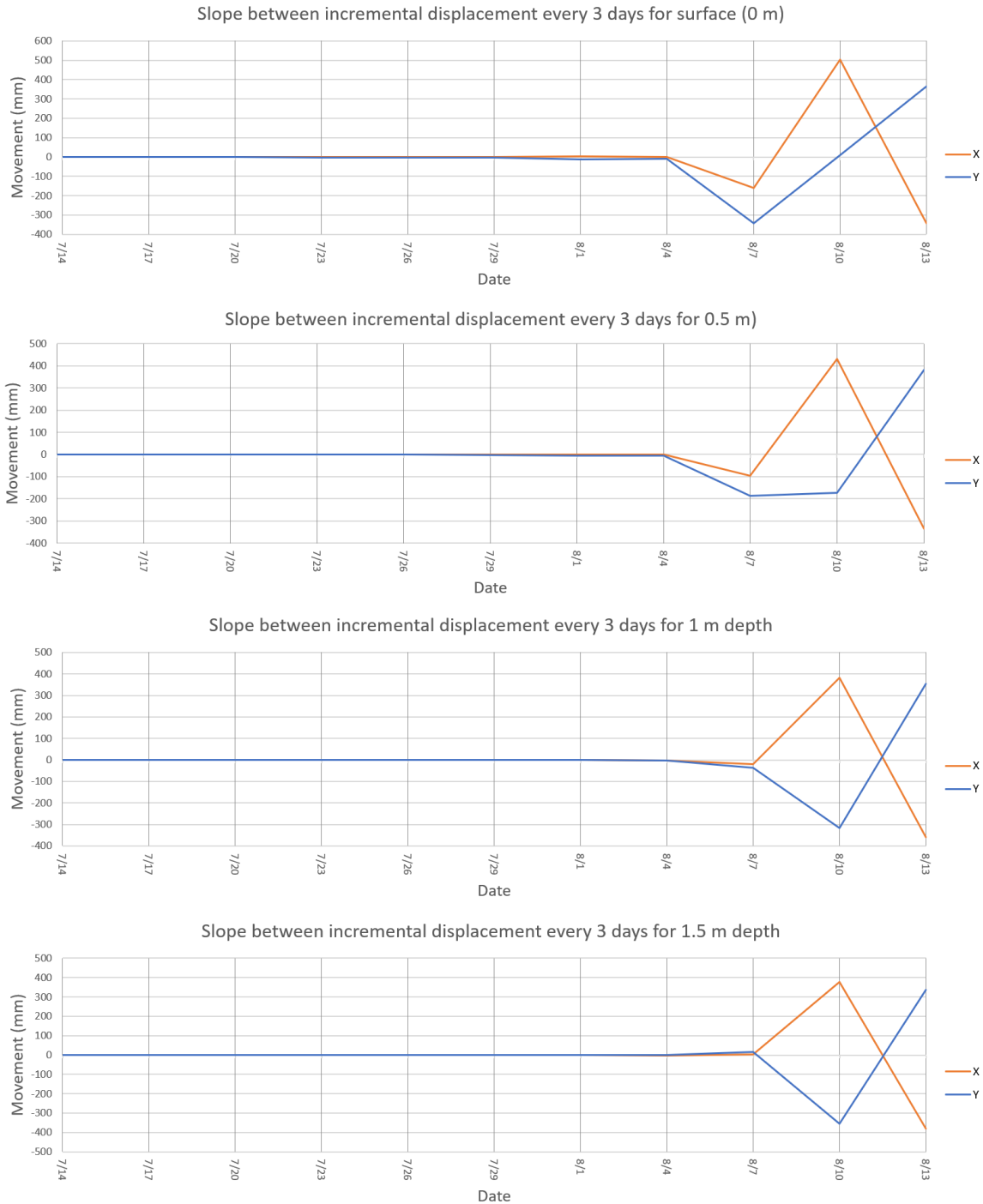


Figure 23. Change in position (slope) every 3 days for surface; 0.5 m depth; 1 m depth (upper right); and 1.5 m depth between June 5th and August 12th in BH2

These trends can also be visualized in the velocity of the movements, as shown in Figure 24. This figure shows relatively stable velocities of less than 1mm/6 hour period at various depths until the end of July (surface) or beginning of August (0.5, 1m and 1.5 m depths). Towards the end of July and beginning of August, there is a steady increase in movements until the slumping event on August 12th.

Velocity per recording period

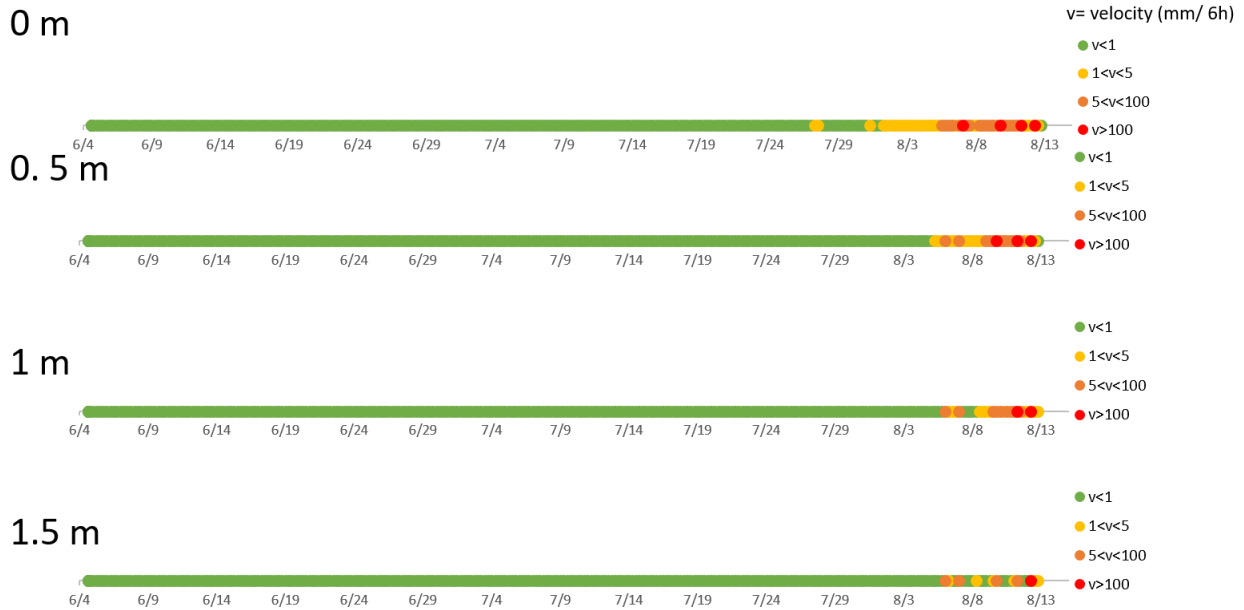


Figure 24. Velocities of combine x and y movement per recording period (mm/6h), where v is the velocity for A) the surface (0m); B) 0.5 m depth; C) 1 m depth; D) 1.5 m depth.

4.2. ERT and EM

4.2.1. ERT

Four ERT surveys were conducted on this site (Table 2). For two of these surveys (WH_1456_ERT1 and WH_1456_ERT2) both the Wenner and dipole-dipole array configuration were measured. For WH_1456_ERT3 and WH_1456_ERT4 only the Dipole-dipole array was measured. The results obtained with the Wenner and dipole-dipole arrays mostly show similar resistivity distributions in the ground, however the dipole-dipole array shows more detail relative to the low resistivity areas.

The WH_1456_ERT1 survey was completed on June 14th, 2019. It ran from east to west, through a dense undisturbed deciduous mixed forest (Figure 25) 12 meters away from the headwall. Data suggests that permafrost could be as deep as 30 meters towards the eastern part of the survey. High resistivity pockets (dark blue shades) seem to be concentrated between 25 to 50 meters along the survey. Some tension cracks manifested at the ground surface.

The permafrost table could be at its shallowest towards the western end of the profile, where the resistivity values remain relatively high (2500 ohm.m). A lower resistivity core (red shades) can also be observed at 40 meters; this could potentially be the result of a ghosting effect from the high resistivity material above or associated with water movement. Another lower resistivity core can be

observed at 180 meters from 8 to 12 meters depth. This could be the result of underground water flow within the permafrost, due to the discontinuous distribution of permafrost in the Takhini Valley.

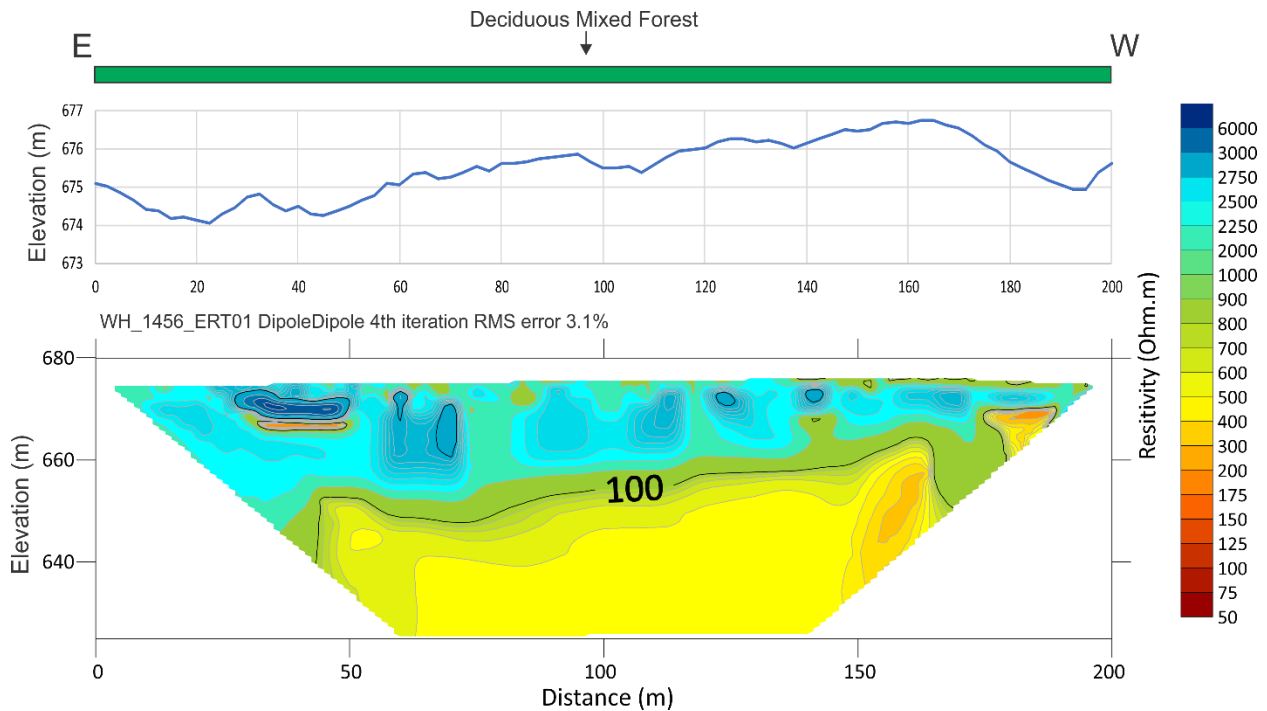


Figure 25. WH_1456_ERT1 DipoleDipole 200 meters transect (east to west)

WH_1456_ERT2 was conducted on July 16th, 2019. This transect ran east to west (Figure 26) in a deciduous mixed forest, along the cleared portion of the right of way of the Alaska highway and 30 meters away from the headwall. The survey intercepted the borehole location of WH_1456_BH2 at electrode 31 and WH_1456_BH1 at electrode 32. The vegetation cover was colonized predominantly by trembling aspen, and white spruce. The underbrush, composed mainly of small aspen, willow and soapberry, was dense in the first and last quarter of the profile. It then became more open between 60 and 80 meters. The survey intercepted meter deep tension cracks at 5 and 135 meters along the profile (Figure 26).

The resistivity data suggests that the permafrost is more discontinuous closer to the highway. High resistivity pockets (blue shades) are concentrated between 50 and 80 meters. This cluster of high resistivity, which likely represents ice rich permafrost, could also be observed on WH_1456_ERT1. Permafrost distribution seems more localized and does not tend to go deeper than 20 meters at its deepest (77.5 meters along the profile). Some small high resistive pockets (light blue) can be observed at 30, 115 and 180 meters. Low resistivity areas (red/orange shades), at 35 and from 115 to 200 meters may indicate ice poor and/or unfrozen material, or the presence of liquid ground water circulating within permafrost. It is not impossible to have permafrost in areas with resistivity as low as 100 ohm.m, because in fine-grained materials, near-0°C temperatures can result in higher liquid water content resulting in low resistivity values.

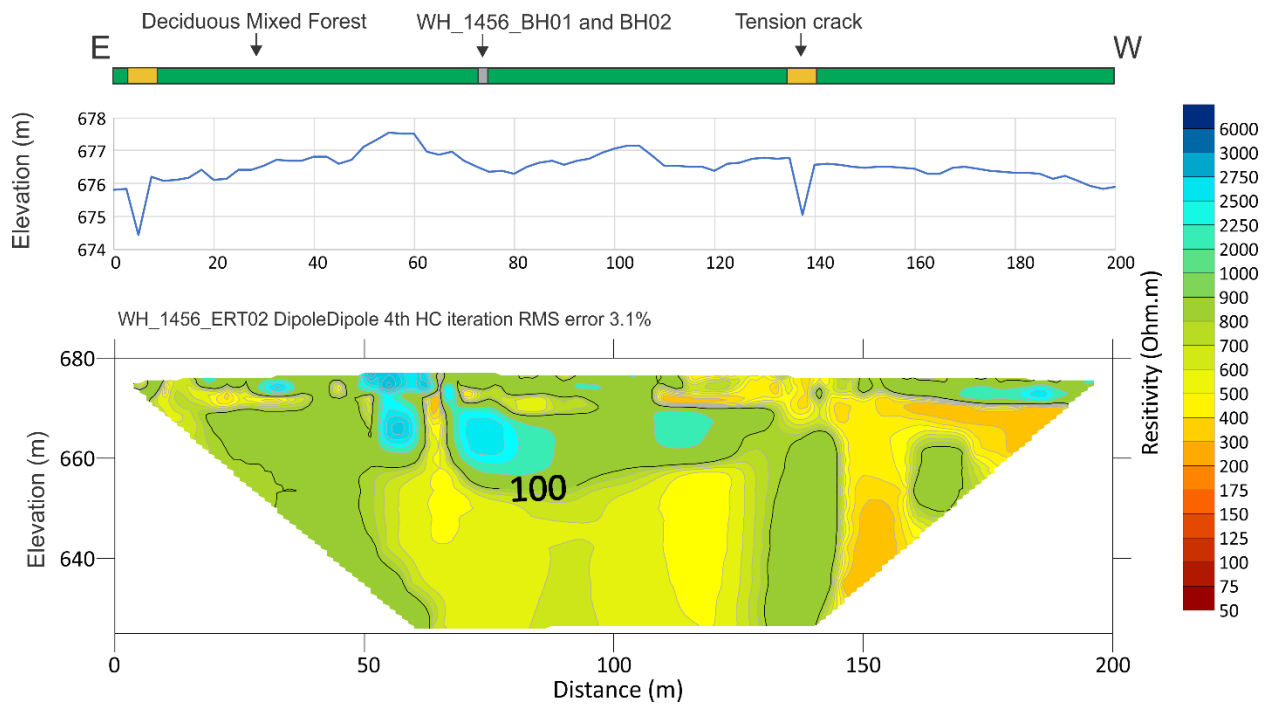


Figure 26. WH_1456_ERT2 DipoleDipole 200 meters transect (east to west)

WH_1456_ERT3 was completed on August 23rd, 2019. The 500-meter survey ran west-east (Figure 27) along the right-hand side of the Alaska Highway embankment, going down a gentle slope. The vegetation cover was open and colonized predominantly by small trembling aspens, willows, and some spruce saplings. The data suggests localized high resistivity areas (dark blue) up to 7 meters deep from 20 to 110 meters along the profile. Material from 200 to 280 meters along the survey is likely to be unfrozen. Some deep low resistivity pockets (red shades) visible at 265 and 365 meters could be associated with groundwater flow.

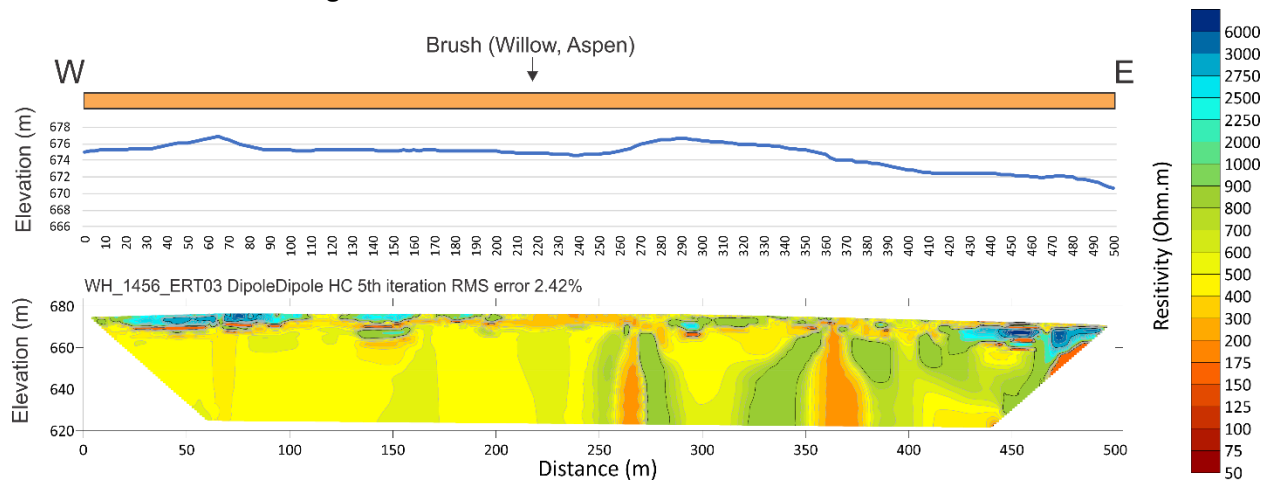


Figure 27. WH_1456_ERT3 DipoleDipole 500 meters transect (west to east)

WH_1456_ERT4 was completed on September 12th, 2019. The 500-meter survey ran west-east (Figure 28) along the left-hand side of the Alaska Highway embankment, going down a gentle slope. The vegetation cover was very similar to the one encountered at WH_1456_ERT3, which included small trembling aspens, willows, and some spruce saplings. The data shows high resistivity areas (blue shades) down to 7 meters deep, along most of the profile. Only the first 70 meters of the survey seem unfrozen. One larger highly resistive cluster, towards the end of the profile (450 to 500 meters) show potential ice-rich material from 17 to 35 meters of depth. Some shallow low resistivity pockets, between 5 and 10 meters of depth along the profile could be associated with groundwater flow within permafrost.

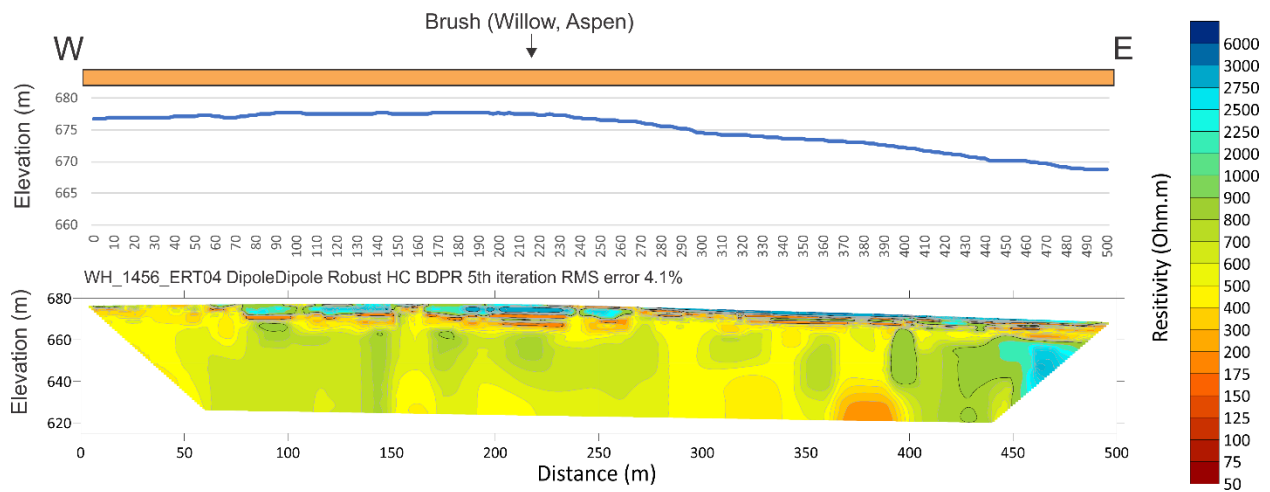


Figure 28. WH_1456_ERT4 DipoleDipole 500 meters transect (west to east)

Overall, the very high-resistivity areas (dark blue) are attributable to ice-rich fine-grained sediment (clayey-silts); they increase as you get closer to the headwall and become more sporadic closer to the highway. The low resistivity values could be attributable to ice poor and/or unfrozen material, the lowest values may indicate the presence of liquid ground water.

4.2.2. 3D ERT & EM

The EM and 3D ERT surveys are an experimental attempt to obtain a three-dimensional representation of some of the ground properties, primarily ground ice content and groundwater occurrence. While the processing of the 3D ERT survey did not provide any specific difficulties, that of the EM data did.

The EM data products consist of horizontal slices representing ground conductivity for each investigated frequency (1, 3, 7, 10, 13, and 16 kHz). The preliminary results presented in this section remain tentative as EM data require additional post-treatment, specifically regarding the calculation

of the skin depths, i.e. the depths of investigation for each surveyed frequency. The skin depth δ is given by the following equation.

$$\delta = \sqrt{\frac{2}{\omega\mu\sigma}}$$

Where $\omega = 2\pi f$ and f is the frequency in Hz

$\mu = 4\pi \cdot 10^{-7}$ (magnetic permeability)

σ = electrical conductivity in of the geologic materials of interest in S/m

In the case of the present survey, the equation is especially difficult to solve because the result is influenced by the nature of the investigated soil, which in this case is a non-homogenous/isotropic geologic medium consisting of a sedimentary soil that can be either dry and/or wet with a variable content of ground ice along the profile. To circumvent this difficulty and proceed with a tentative 3D model, a depth of investigation was attributed to each EM slice based on an empirical approach. The approach relies on two hypotheses: 1- the equation suggests that a linear relationship should exist between depth and frequency and could be used to locate the slices; 2- the manufacturer of GSSI Profiler EMP-400 system suggest that the depth of investigation of its system is limited to about 7.5 m.

Consequently, boundary depths of 0 m and 7.5 m have been attributed to 16kHz and 1kHz frequencies, respectively, while the other frequencies were linearly spread along the 10 m depth interval.

The EM and ERT survey slices are presented in Figure 29. The EM survey shows constant pattern across each frequency: conductive material (red hues) located in the south border of the slices; a large low conductivity area (blue hues) at the east and a smaller low conductivity area at the west. The ERT slices show the same type of pattern where resistive material (blues) are present at the east and at the west, and low resistive material (reds) are present at the south. In addition, the resistivity of the ground increase progressively with depth. Those observations are consistent with drillings and 2D ERT observations. The reddish areas are located near the road where vegetation was cleared, the soil is wet and less likely to be frozen. The blue areas likely represent areas of ice-rich ground.

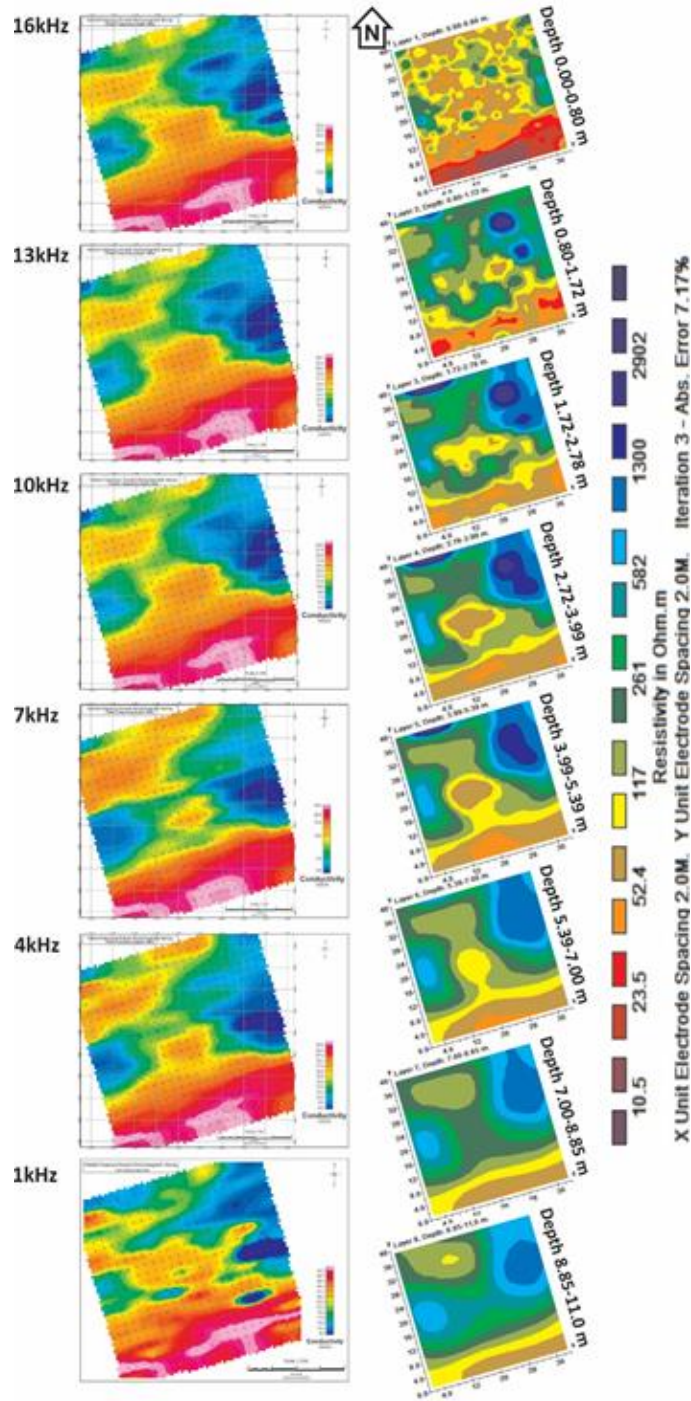


Figure 29. EM (left) and ERT (right) surveys horizontal slices, from shallower slices of the top to deeper slices at the bottom. The slump is located northward, and the road southward

Figure 30 shows a 3D representation of the EM survey. This representation shows the warmer area along the southern edge of the survey, which is cleared and runs along the road. It also shows the two ice-rich bodies closer to the slump. Figure 29 shows a comparison between EM and ERT data; for this representation, only the high-resistivity bodies are shown as discreet blue volumes (delimited by

the dotted line in Figure 31). Overall, there is a strong relationship between the two types of geophysical data.

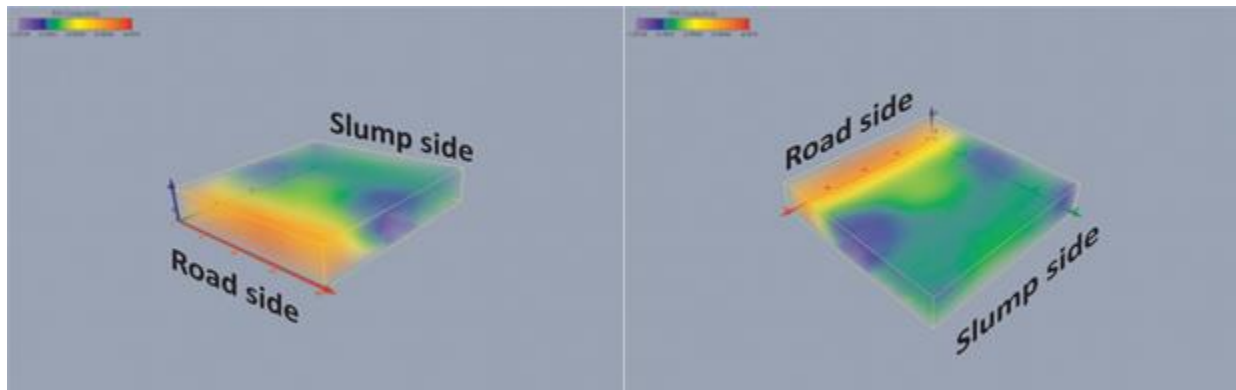


Figure 30. EM survey at km 1456 of the Alaska Highway. The blue areas show ice-rich permafrost zones while the redish areas show warm or thaw permafrost zones

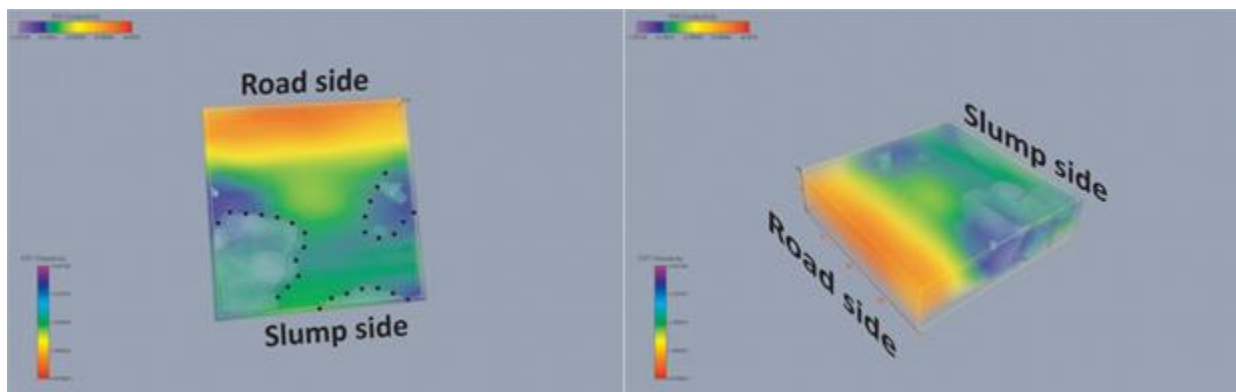


Figure 31. Comparison between EM and ERT surveys at km 1456 of the Alaska Highway. Comparison shows a good correlation between the two types of surveys. Dotted lines indicate ice-rich areas identified by the ERT survey

Observing the 3D ERT model alone, some specific features can be observed when specific iso-curves, which correspond to specific resistivity values, are shown separately. By focusing on high-resistivity values, ice-rich zones can be visualized in the model (blue iso-curve in Figure 32). When looking at intermediate resistivity values, a boundary between firmly frozen ground and wet or unfrozen ground can be implied (green iso-curve in Figure 32). These observations suggest that the ground ice distribution is not homogenous across the area, but rather that ice-rich ground is present in clusters. The data also suggest the presence of a groundwater channel crossing the site in at south-north direction. This is not surprising as springs have been observed on the headwall as well as in some of the boreholes during drilling.

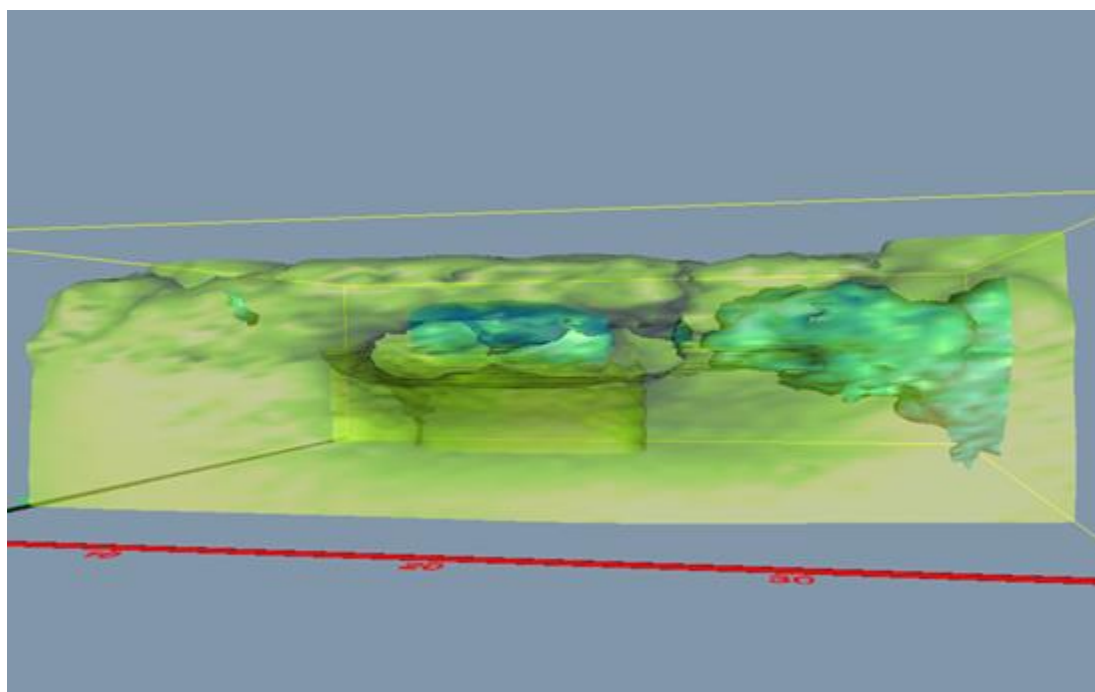
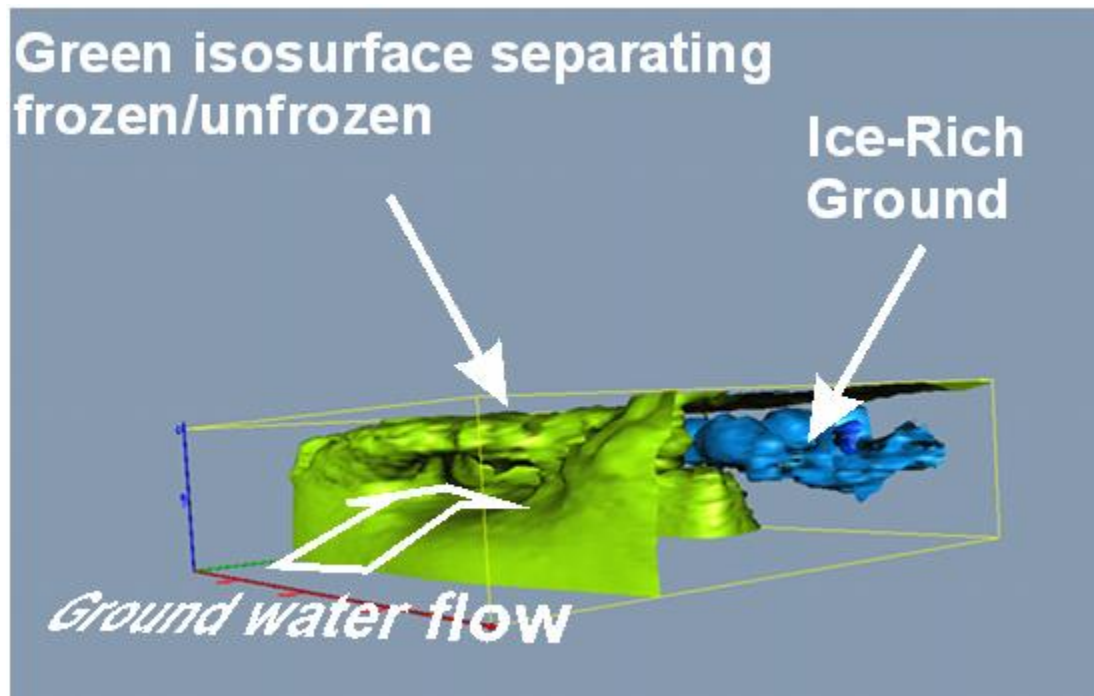


Figure 32. 3-D ERT survey at km 1456 of the Alaska Highway. The blue bodies are ice-rich permafrost zones while the greenish iso-curve separate warm and/or wet and/or unfrozen areas from frozen ground

4.3. Geospatial analyses

4.3.1. Field, aerial and satellite imagery, and UAV observations

To better understand the morphological characteristics of the site, historical aerial and satellite imagery were analyzed, along with current UAV-derived orthoimages and models.

Aerial and satellite imagery analyses suggest that the thaw slump was instigated in 2014 by the erosion of the Takhini river. Using this imagery in combination with UAV-derived orthoimages has allowed for the progression of the slump to be monitored. According to this analysis, the ongoing thaw of exposed ice has caused the headwall to retreat towards the Alaska highway at rates of up to 8 m/year since 2014 to its current position 55 m downslope from the highway (Table 6, Figure 33). At present, the thaw slump has a 70-m wide crescent-shaped source zone, with a steep headwall up to 7 m high which exposes ice-rich permafrost within glaciolacustrine silt and clay sediments. Groundwater springs can be observed seeping from the headwall at several locations between 2-3 meter depth. As thaw debris accumulate at the base of headwall, they are mobilized by mudflows that have travelled upwards of 100 m. On September 2nd 2019, a large mudflow event deposited a low-angle tongue of debris more than halfway across Takhini River (Figure 33).

Table 6. Measured rate of expansion of the retrogressive thaw slump since 2016.

Date	Distance to road (m)	Full size area (m ²)	Area to straight river bank (m ²)
7/27/2016	105.8	1321.9	1257.8
8/18/2018	80.9	2816.3	2705.8
5/16/2019	80.9	N/A	N/A
8/22/2019	71.8	4777.8	4018.5
9/11/2019	69.7	6652.4	4355.5
9/25/2019	68	6942.5	4524.8
10/30/2019	68.8	6816.1	4324.6
5/20/2020	68	6982.9	4590.7
8/26/2020	57.5	7453.2	5466.7
9/29/2020	55.1	7462.02	5499.65

Older aerial imagery shows that two retrogressive thaw slumps of similar size have occurred on the slope adjacent to the current slump. One slump was located 100 m to the west and was active in the 1940s. Another slump was located 200 m to the east and was active from 1979 to 1989. This slump caused tension cracks in the highway embankment. These older slumps have since stabilized, most likely due to depletion of ground ice and/or covering and insulation of their headwalls.

Surface tension cracks up to 1.4 meters deep and 1.8 meters wide have developed adjacent to and upslope from the slump (Figure 33), indicating widespread slope instability that extends beyond the footprint of the slump, likely due to creep or solifluction processes. Tree roots and split trunks extend across the tension cracks in several locations (Figure 33). The crack widths of twelve split trees shown in Figure 34 were remeasured at regular intervals throughout the summer and fall of 2019, with cracks expanding at rates of up to 1-2 cm/month.

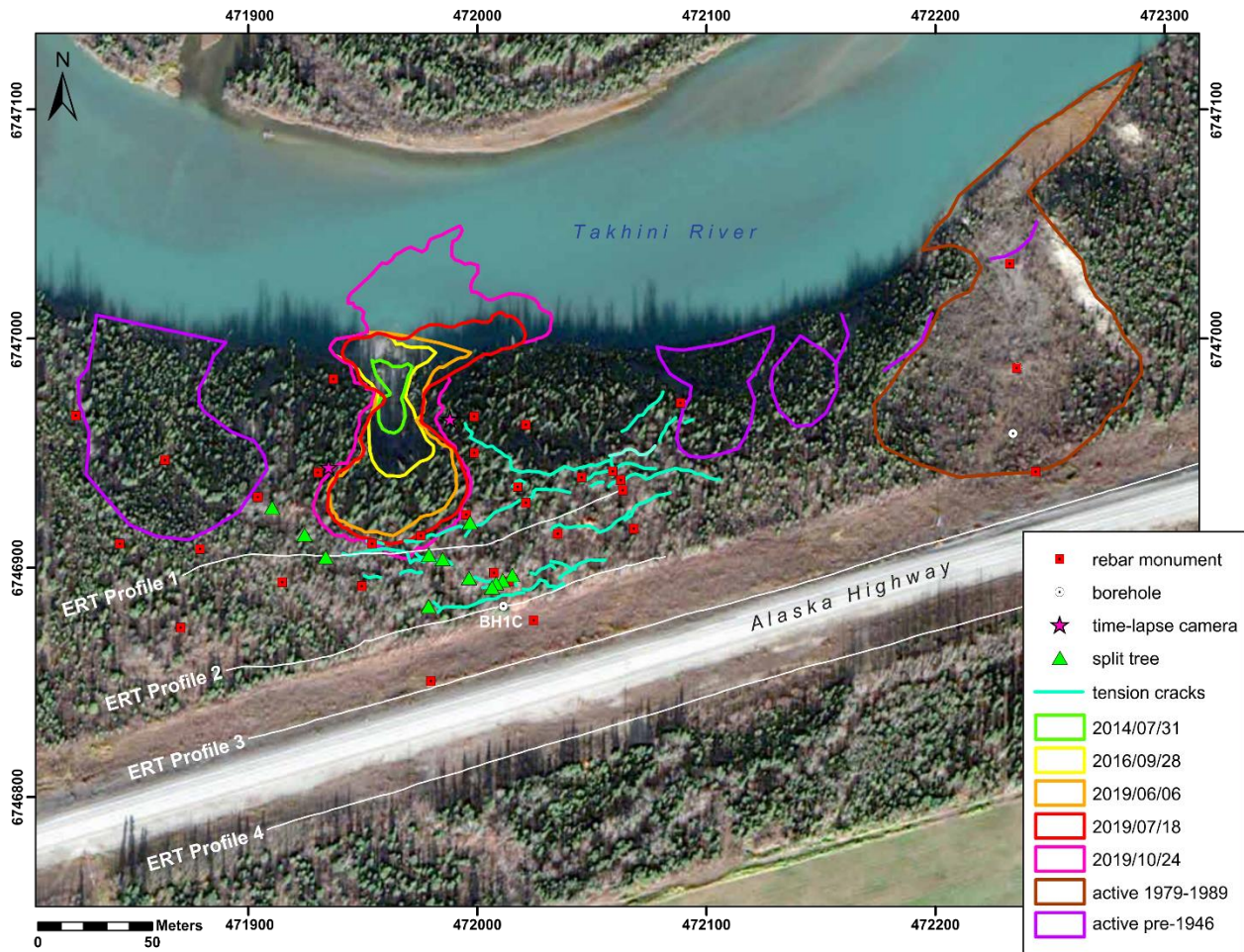


Figure 33. Map of past retrogressive thaw slumps, also showing tension cracks and split trees locations



Figure 34. Split trees due to tension cracking

degradation under the right of way of the Alaska highway since its construction in 1942. However, the ERT data suggest that permafrost could still be present on the southern side of the highway.

Current warm ground temperatures (just below 0 °C) and the distribution of ice rich permafrost in clusters (observed in the ERT surveys) seem to indicate that the permafrost may have formed in a colder and more humid environment than the one prevailing today. The lack of thick organic cover and the abundance of deciduous trees on site is atypical when considering other similar ice-rich epigenetic permafrost in discontinuous areas. This atypical environment suggests that the permafrost may have originally formed under different environmental conditions, associated to a different climate and different vegetation. Therefore, the site might be underlain by relic permafrost that is precariously in balance with the current climate.

The cryostratigraphical observations from the core samples and the headwall are consistent with syngenetic permafrost. The formation of this type of ground ice, with suspended and thick layered cryostructure in fine grained material, requires ample water supply, a slow thermal gradient, and usually an organic cover. This type of permafrost is generally associated with permafrost plateaus and frost heave mound environments (Calmels et al, 2008). Such conditions may have existed in the Takhini Valley when the permafrost developed. Although the vegetation and the topography have changed, the original cryostratigraphical imprint, shown by the ERT survey in the shape of ice-rich ground clusters, has remained unchanged. The shading provided by the newer deciduous forest may have contributed to the preservation of this relic permafrost.

The headwall of the retrogressive thaw slump provides an exceptional view of the ground profile. It shows lacustrine deposits (clayey silts) reworked by ground movements (Figure 36), with ice lenses being in unconformity with the stratigraphy yet parallel to the topography. This indicates that the permafrost was formed after this ground disturbance.



Figure 36. Retrogressive thaw slump headwall

Figure 37 shows the approximate ground ice distribution based on the ERT profiles. The location of the ice suggests that the study site is vulnerable to further degradation even near the road. It is of note that the location of the inactive slump shows no ground ice, which could explain why this slump stabilized, or alternatively, that any ice present at that location has already melted out with the slump.

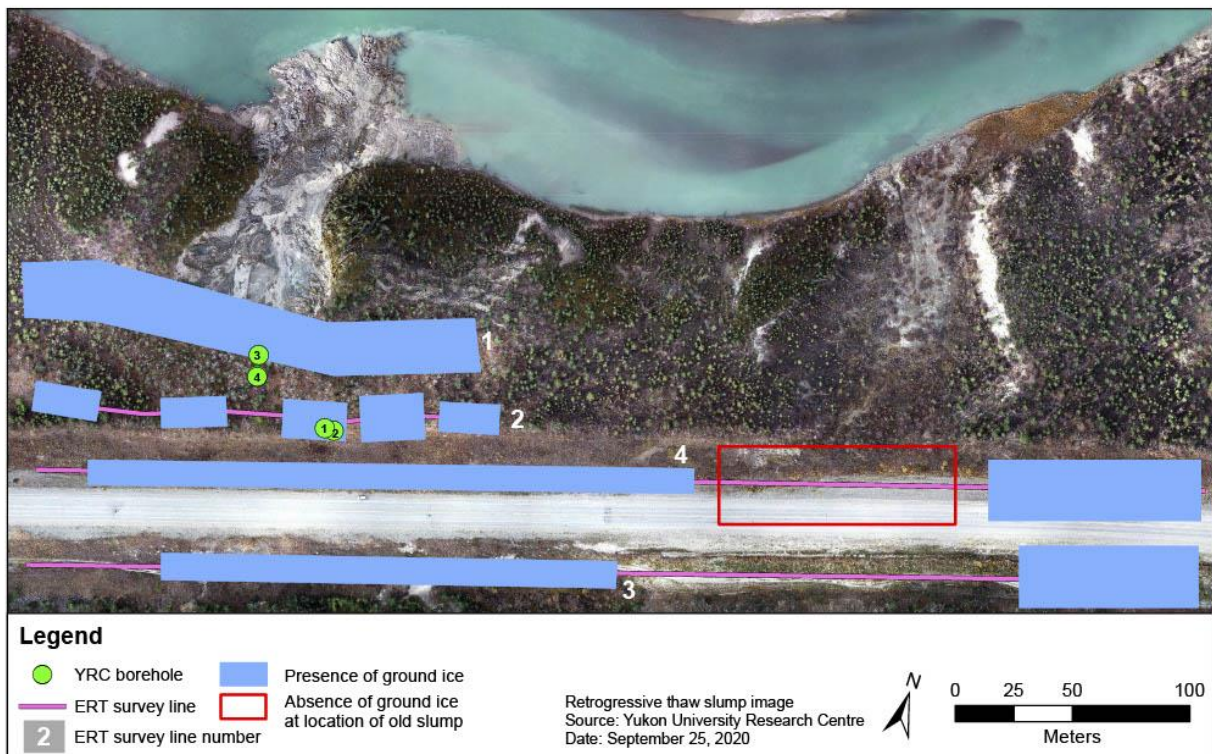


Figure 37. Approximate position of ground ice based on ERT profiles

5.2. Retrogressive thaw slump processes

Geophysical and borehole data emphasize the ice-rich nature of the ground at this site, as well as the presence of ground water flows. While the thaw processes may have been initiated by bank erosion on the Takhini River, they have been exacerbated by the high ground ice content and the thermal effect of ground water springs circulating within the ice-rich clusters as depicted in the 3D ERT models (section 4.2.2). Irrigation of the farmland located on the other side of the highway in the summertime may contribute to the degradation processes.

The ground temperature and inclinometer data show precursory indicators of the RTS failure processes. Temperatures recorded in BH3 show an increase 6 days before the headwall reached the borehole and the pipe collapsed (Figure 38A). Incremental displacement is minimal at the surface (0m) and 0.5 m depths in BH3 until August 6th. After this, it increases until the failure of the borehole, also 6 days later (Figure 38B and C).

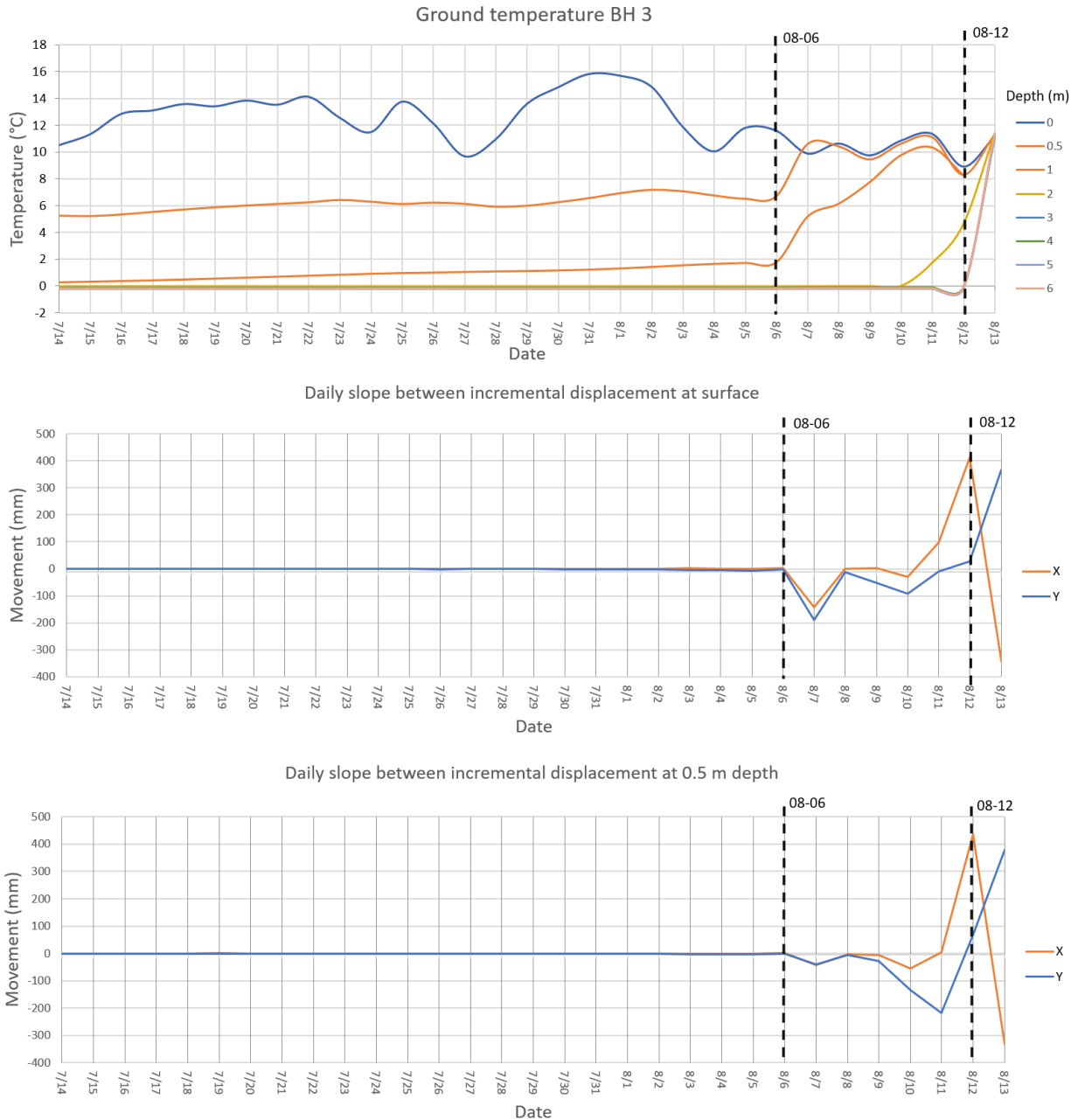


Figure 38. Comparison between ground temperature and displacement recorded by the inclinometer in BH3 at 0m and 0.5 m

Farther away from the slump at BH2, inclinometer data also show a sudden displacement when the slump gained on BH3. This suggests that the slump eroded in one quick event rather than through slow incremental erosive processes.

All together, these records suggest that ground temperature and inclinometer data could be used as an anticipatory warning of failure for a specific point many days before a catastrophic event. Remote daily monitoring of this data could be used in an alarm system to trigger an alert for an upcoming

collapse. Such a system could be used to monitor the thaw slump as it progresses towards the highway and help the highway operator to ensure public safety.

6. References

- ASTM Standard C29 – 09, 2000. Standard Test Method Bulk Density (“Unit Weight”) and Voids in Aggregate. West Conshohocken, PA, ASTM International.
- ASTM Standard D422 – 63, 2000. Standard Test Method for Particle-Size Analysis of Soils. West Conshohocken, PA, ASTM International.
- Bond, J.D., 2004. Late Wisconsinan McConnell glaciation of the Whitehorse map area (105D), Yukon. In: Yukon Exploration and Geology 2003, Emond, D.S. and Lewis, L.L. (eds.), Yukon Geological Survey, p. 73-88.
- Burn, C.R. 1987. Thermokarst ponds and ground temperatures in Takhini Valley. In XIIth INQUA Congress field excursions A20 and A20b Research in Yukon. Edited by S.R. Morison and C.A.S. Smith. National Research Council of Canada, Ottawa, Ont., p. 34.
- Burn, C.R. 1998. The response (1958-1997) of permafrost and near-surface ground temperatures to forest fire, Takhini River valley, southern Yukon Territory. *Canadian Journal of Earth Sciences*. 35: 184-199.
- Calmels, F., Allard, M., 2007. Segregated Ice Structures in Various Heaved Permafrost Landforms Through CT Scan. *Earth Surface Processes and Landforms*, 33, p 209-225, DOI: 10.1002/esp.1538.
- Egginton, P., French, H., 1976. Thermokarst and related geomorphic processes eastern Banks Island, N.W.T. University of Ottawa, PhD Thesis. UMI: EC55744.
- French, H., 2007. *The Periglacial Environment*. Third Edition.
- Hauck, C., Isaksen, K., Vonder Mühll, D. and Sollid, J.L., 2004. Geophysical surveys designed to delineate the altitudinal limit of mountain permafrost: An example from Jotunheimen, Norway. *Permafrost and Periglacial Processes*, vol. 15, p. 191-205, doi:10.1002/ppp.493.
- Hilbich, C., Hauck, C., Hoelzle, M., Scherler, M., Schudel, L., Voelksch, I., Vonder Muehll, D. and Mausbacher, R., 2008. Monitoring mountain permafrost evolution using electrical resistivity tomography: A 7-year study of seasonal, annual, and long-term variations at Schilthorn, Swiss Alps. *Journal of Geophysical Research-Earth Surface*, vol. 113, doi:10.1029/2007JF000799.
- Hilbich, C., Marescot, L., Hauck, C., Loke, M.H. and Mausbacher, R., 2009. Applicability of electrical resistivity tomography monitoring to coarse blocky and ice-rich permafrost landforms. *Permafrost and Periglacial Processes*, vol. 20, p. 269-284, doi:10.1002/ppp.652.
- Hughes, O.L., Pilon, J., Veillette, J.J., Zoltai, S.C., and Pettapiece, W.W., 1973. Three surficial geology and geomorphology maps of Trial river, Bell river, Old Crow map-areas, Mackenzie Valley and northern Yukon Territory. Geological Survey of Canada, Open File 167, 1 sheet. doi:10.4095/129201
- Klassen, R.W. 1979. Thermokarst terrain near Whitehorse, Yukon Territory. In *Current research*, part A. Geological Survey of Canada, Paper 79-1A, pp. 385–388.
- Kneisel, C., Hauck, C. and Vonder Mühll, D., 2000. Permafrost below the timberline confirmed and characterized by geoelectrical resistivity measurements, Bever Valley, eastern Swiss Alps. *Permafrost and Periglacial Processes*, vol. 11, p. 295-304, doi:10.1002/1099-1530(200012)11:4<295::AID-PPP353>3.0.CO;2-L.

Kneisel, C., Hauck, C., Fortier, R. and Moorman, B., 2008. Advances in geophysical methods for permafrost investigations. *Permafrost and Periglacial Processes*, vol. 19, p. 157-178.

Lewkowicz, A. G., Bonnaventure, P. P., Smith, S. L. and Kuntz, Z., 2012. Spatial and thermal characteristics of mountain permafrost, Northwest Canada, *Geografiska Annaler*, vol. 94, p. 195–213, doi:10.1111/j.1468-0459.2012.00462.x.

Lewkowicz, A. G., Etzelmüller, B.E. and Smith, S.L., 2011. Characteristics of discontinuous permafrost from ground temperature measurements and electrical resistivity tomography, southern Yukon, Canada. *Permafrost and Periglacial Processes*, vol. 22, p. 320-342.

Lipovsky, P.S. and Yoshikawa, K., 2009. Initial results from the first year of the Permafrost Outreach Program, Yukon, Canada. In: *Yukon Exploration and Geology 2008*, L.H. Weston, L.R. Blackburn and L.L. Lewis (eds.), Yukon Geological Survey, p. 161-172.

Lipovsky, P.S., 2015. Summary of Yukon Geological Survey permafrost monitoring network results, 2008-2013. In: *Yukon Exploration and Geology 2014*, K.E. MacFarlane, M.G. Nordling and P.J. Sack (eds.), Yukon Geological Survey, p. 113-122.

Loke, M.H. and Barker, R.D., 1996. Rapid leastsquares inversion of apparent resistivity pseudosections using a quasi-Newton method. *Geophysical Prospecting*, vol. 44. p. 131-152, doi:10.1111/j.1365-2478.1996.tb00142.x

Loke, M.H., Acworth, I. and Dahlin, T., 2003. A comparison of smooth and blocky inversion methods in 2D electrical imaging surveys. *Exploration Geophysics*, vol. 34, p. 182-187.

Miceli, C., 2012. Seasonal cycling in electrical resistivities at ten thin permafrost sites, southern Yukon and northern British Columbia. Unpublished MSc thesis, Department of Geography, University of Ottawa, ON, 201 p.

Murton, J.B. and French, H.M., 1994. Cryostructures in permafrost, Tuktoyaktuk coastlands, western arctic Canada. *Canadian Journal of Earth Sciences*, vol. 31, no. 4, p. 737-747.

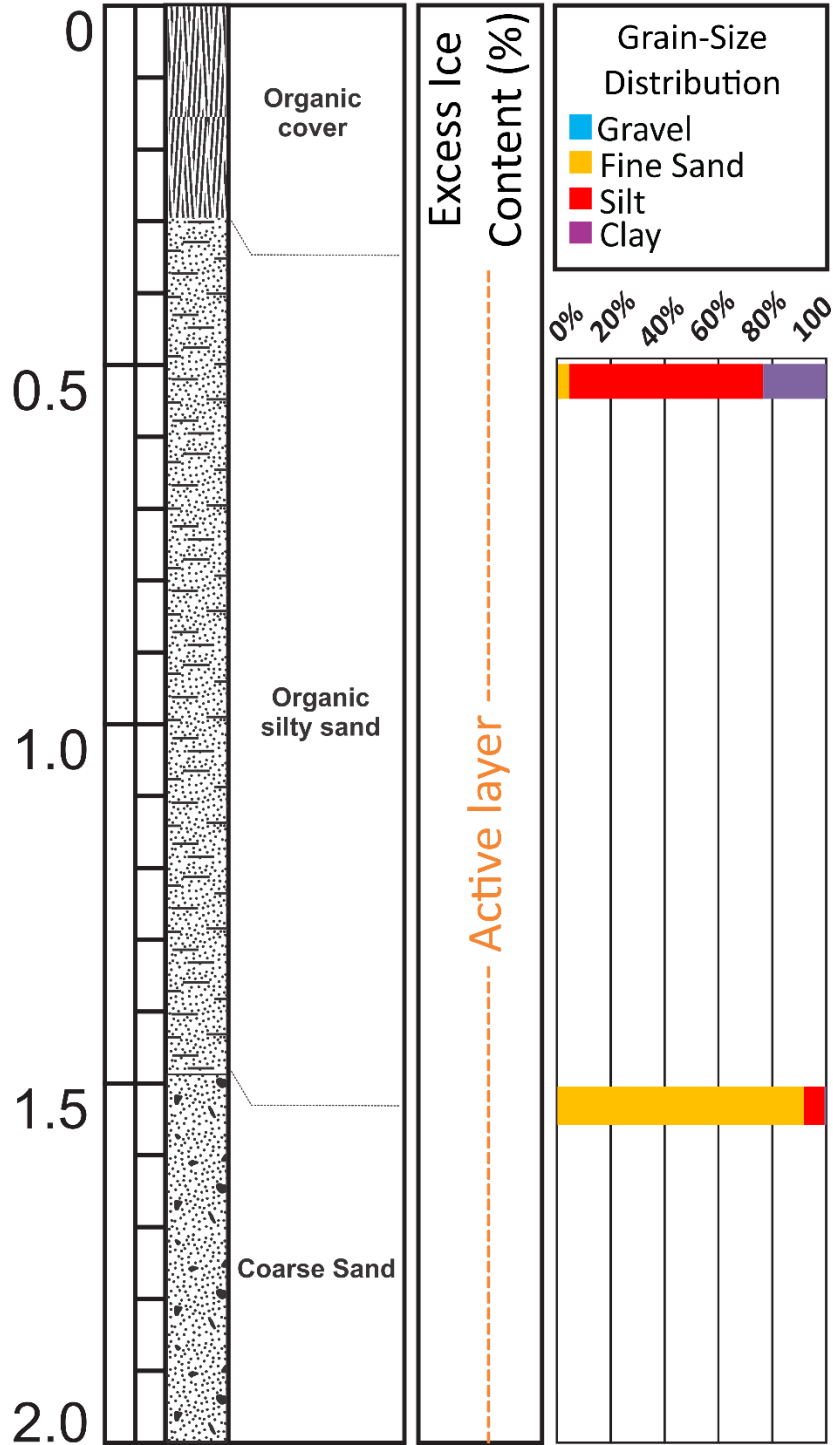
Smith, M.W. and Riseborough, D.W., 2002. Climate and the limits of permafrost: a zonal analysis. *Permafrost and Periglacial Processes*, vol. 13, p. 1-15.

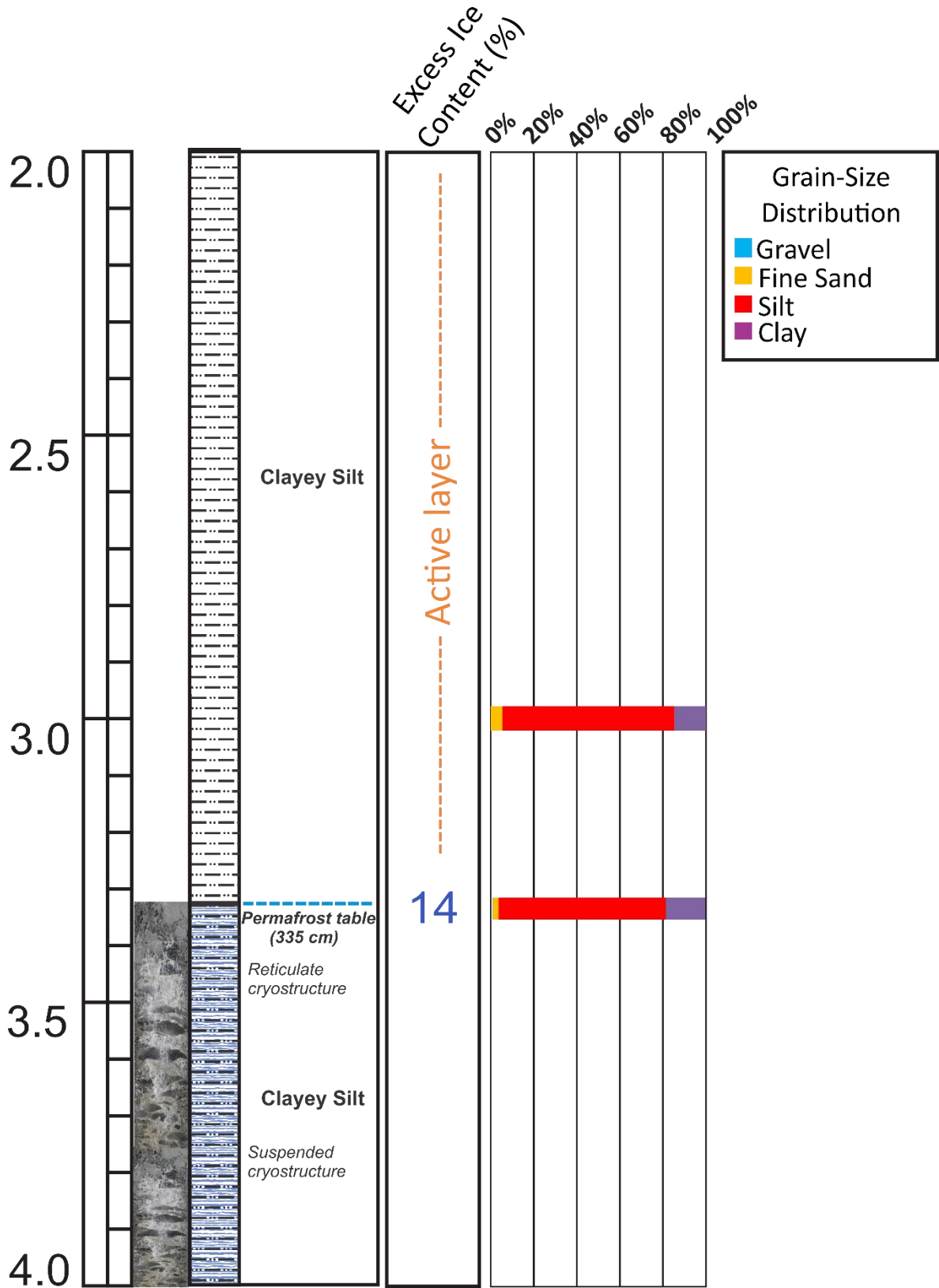
Stephani, E., Fortier, D. and Shur, Y., 2010. Applications of cryofacies approach to frozen ground engineering – Case study of a road test site along the Alaska Highway (Beaver Creek, Yukon, Canada). GEO2010: 63rd Canadian Geotechnical Conference and 6th Canadian Permafrost Conference, Calgary, Canada.

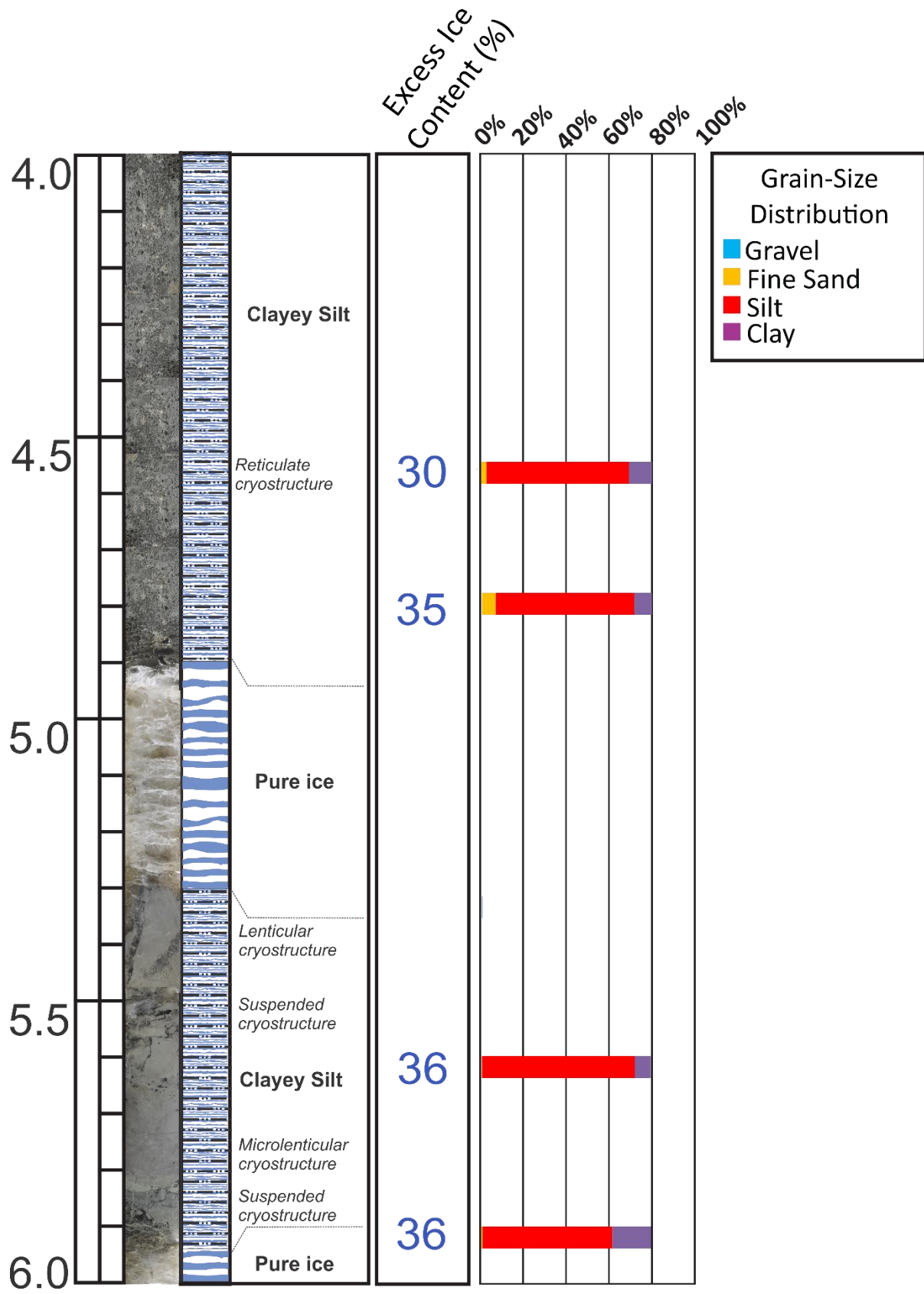
Yukon Geological Survey, 2019. Yukon Digital Bedrock Geology. http://www.geology.gov.yk.ca/update_yukon_bedrock_geology_map.html, accessed: 28 January 2019.

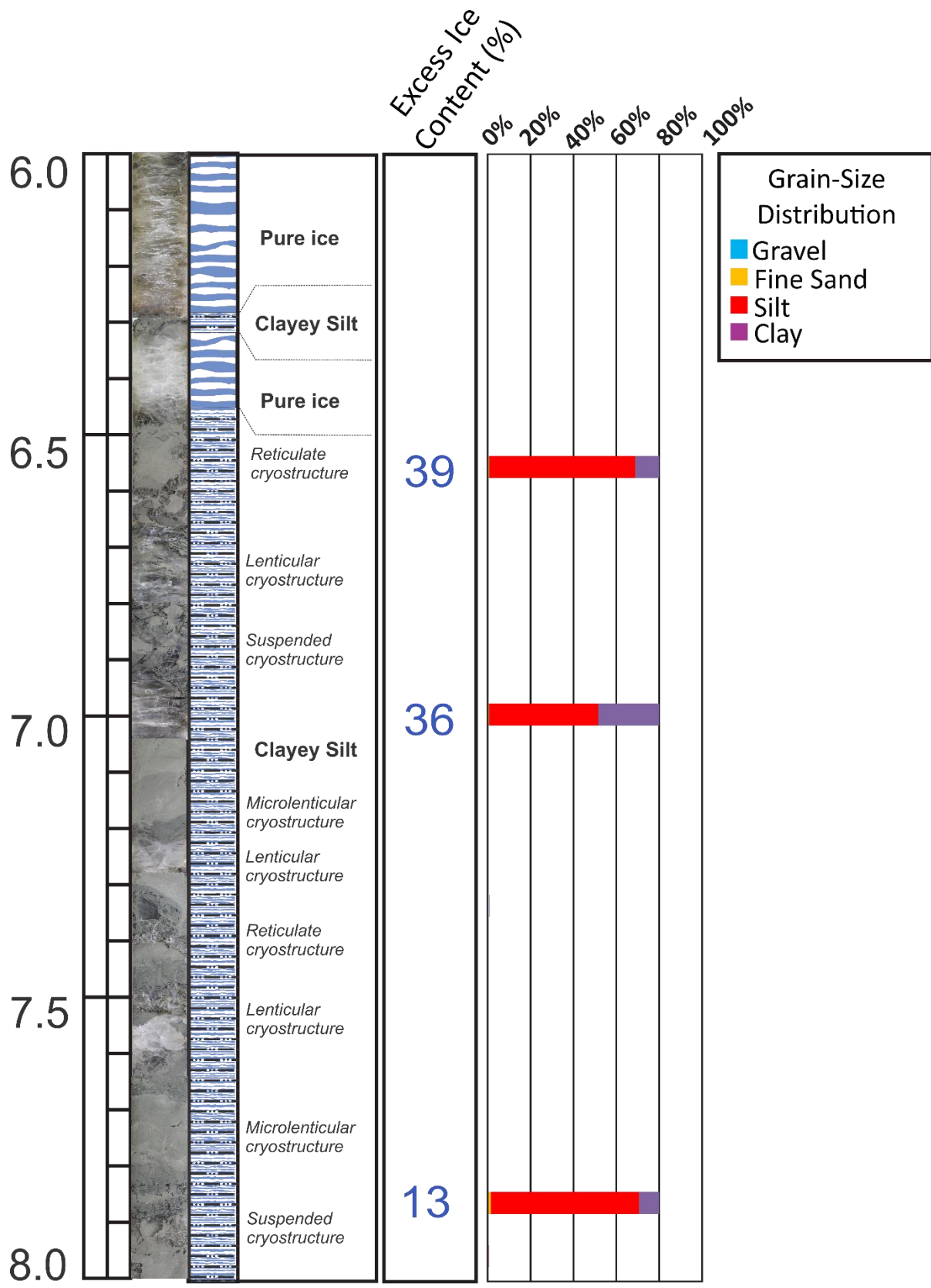
7. Appendix A

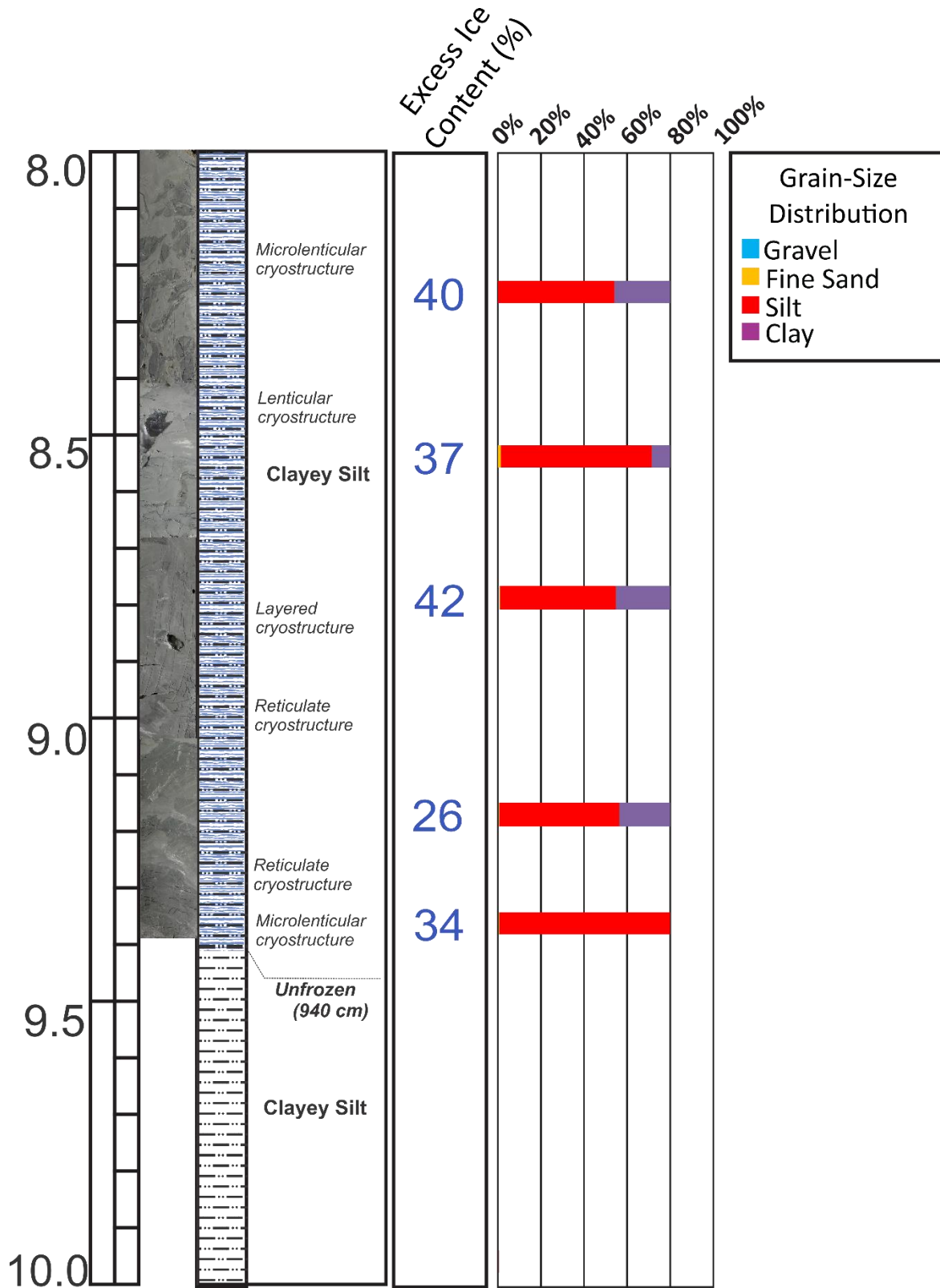
No 1: Borehole log WH_1456_BH1, with volumetric excess ice content and grain size distribution





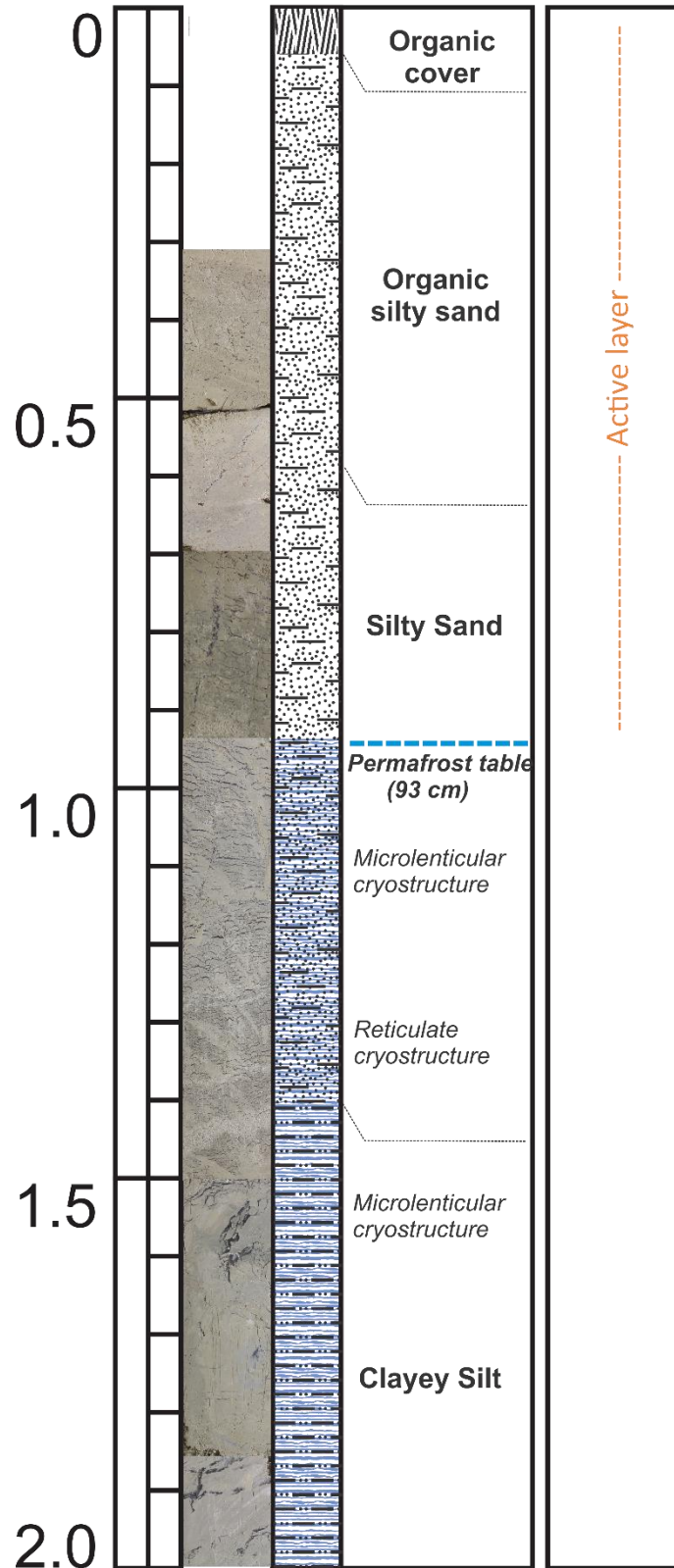


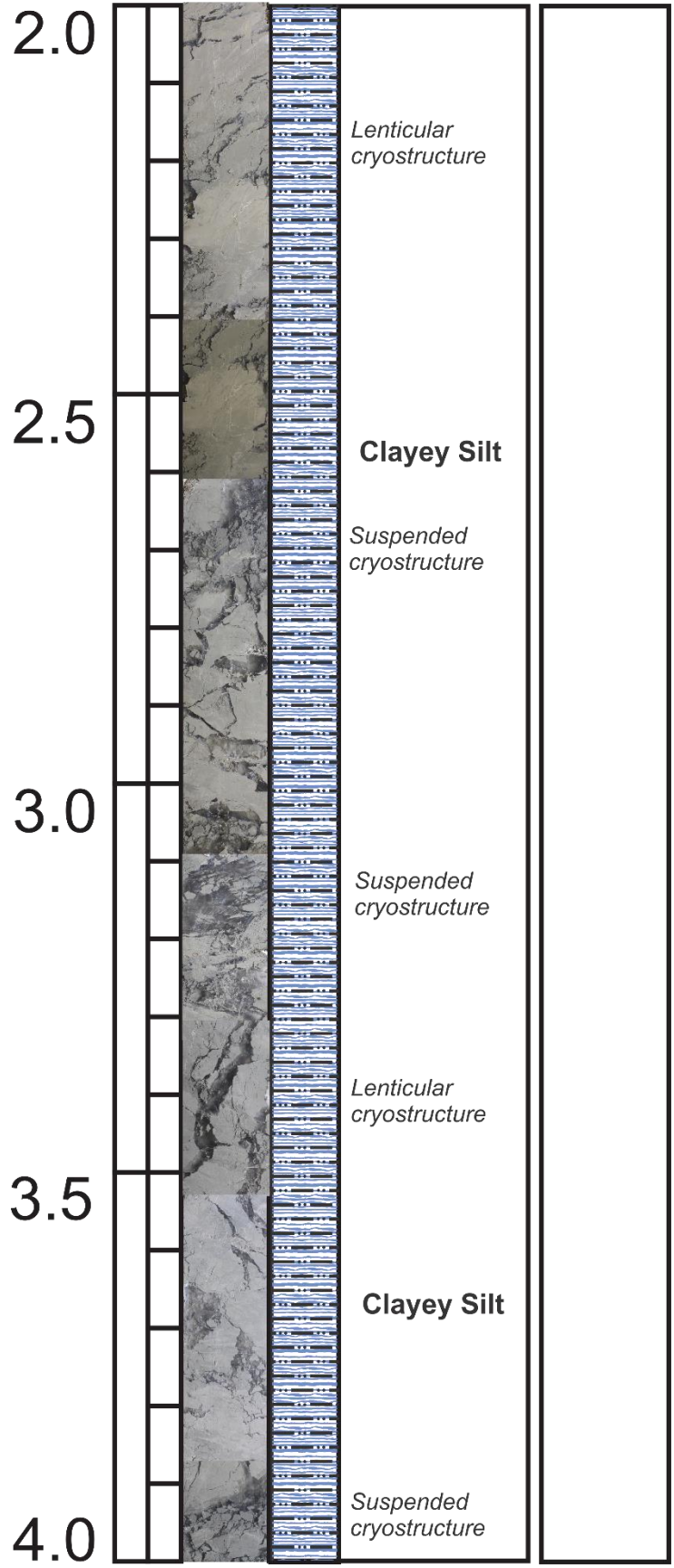


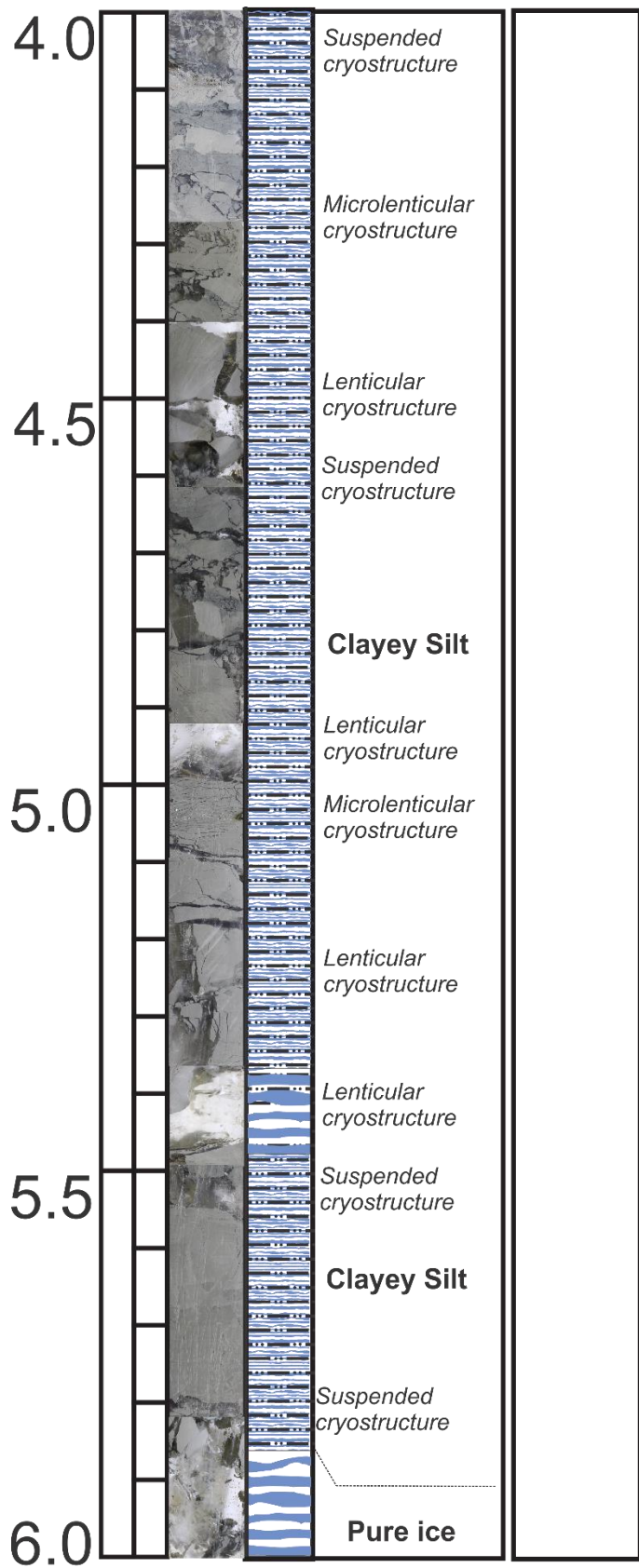


End of Borehole: 10 meters

No2: Borehole log WH_1456_BH3







End of Borehole: 6 meters

